UNIVERSITY OF OSLO
Department of Informatics

On the use of super-resolution algorithms in seismics: *applications within diffraction separation and imaging*

Endrias G. Asgedom

November 19, 2012

Series of dissertations submitted to the
Faculty of Mathematics and Natural Sciences, University of Oslo
No. 1270

ISSN 1501-7710

Cover: Inger Sandved Anfinsen.
Printed in Norway: AIT Oslo AS.

Produced in co-operation with Akademika publishing.
The thesis is produced by Akademika publishing merely in connection with the thesis defence. Kindly direct all inquiries regarding the thesis to the copyright holder or the unit which grants the doctorate.

Preface

This thesis has been submitted to the Faculty of Mathematics and Natural Sciences at the University of Oslo in partial fulfillment of the requirements for the degree *Philosophiae Doctor (Ph.D.)*. The work was carried out in collaboration between the Department of Informatics (Digital Signal Processing and Image Analysis group) and the Department of Geosciences, University of Oslo. The thesis was supervised by Professor Leiv -J. Gelius, Associate Professor Andreas Austeng and Professor Sverre Holm. As part of the Ph.D. program I visited Professor Martin Tygel at the State University of Campinas, Brazil, during the time Aug. 2010 - Feb. 2011. The work has been financed by the Department of Informatics, University of Oslo.

Acknowledgements

First and foremost, I would like to extend my sincere thanks to my main advisor professor Leiv -J. Gelius for his guidance, encouragement and support throughout my Ph.D. studies. I am sure that this dissertation would not have been possible without his unlimited patience, understanding and encouragement. I owe sincere and earnest thankfulness to my co-advisors Associate professor Andreas Austeng and Professor Sverre Holm for there fruitful conversations, discussions and comments.

I would like to thank Professor Martin Tygel, who introduced me to the world of CRS, for being a great advisor when I visited the state University of Campinas during the time Aug. 2010 - Feb. 2011.

I am grateful to my colleagues at the DSB-group and the department of Geosciences for providing such a nice working environment. Special thanks to my best friends Shewa, Abraham, Chuks and Mesay for being there for me when I needed them the most. I also thank the Department of Informatics, University of Oslo for funding this Ph.D. work.

At last but not least, I wish to thank my mother Almaz Negash for her endless support and love.

Abstract

It is both an experimental and theoretical fact that imaging of scatterers using bandlimited signals results in what is known as a *diffraction-limited image*. As a consequence, the best possible resolution obtained from a diffraction-limited system is about half a wavelength of the illuminating wavefield. In the near-field imaging systems used in optics this problem has been overcome by measuring the contribution of evanescent wavefields. However, in case of seismics, the sources and receivers are placed more than three times the wavelength away from the target and the evanescent wavefields are highly attenuated and thus fall below the noise level. Nevertheless, super-resolution imaging (i.e. imaging beyond the diffraction-limit) is possible by utilizing the time-reversal MUltiple SIgnal Classification (MUSIC) algorithm. The main idea is then to perform a Singular Value Decomposition (SVD) of the Multistatic Response (MSR) matrix to obtain the source and receiver side singular vectors which transforms the active experiment into a purely passive one. These singular vectors contain interaction information about the different scatterers, which is the key to obtain super-resolution. Though this algorithm can provide a super-resolved localization of point targets, it is also highly noise sensitive. In this thesis, we propose a phase-coherent time-reversal MUSIC (PC-MUSIC) algorithm, which utilizes the band of frequencies present in the measured data and exhibits a phase-coherent nature of the time-reversal operator. The noise present in the resulting monochromatic time-reversal MUSIC image can now be minimized by averaging over a smaller band of frequencies. The robustness and super-resolution ability of PC-MUSIC has been demonstrated employing both experimental ultrasonic data and numerical simulations based on the Foldy-Lax interaction model.

Both time-reversal MUSIC and its phase-coherent version, PC-MUSIC, are originally designed to localize point like targets. In seismic or Ground Penetrating Radar (GPR) signals, the contributions from point like targets are carried by the diffracted wavefield. However, diffracted signals both in seismic and GPR are often much weaker than the specular reflections making it difficult to utilize them for super-resolution imaging. In this thesis, we propose to separate the diffracted signals from the reflected ones using two parameterized diffraction traveltime approximations. The first technique is based on a modified version of the Common Reflection Surface (CRS) technique. The second diffraction traveltime approximation is based on the REplacement Medium (REM) approach derived in this thesis for applications in a laterally smooth velocity field. The actual diffraction enhancement (or separation) is then carried out by stacking the data along the two approximate diffraction traveltime surfaces with optimal parameters determined using a coherency measure. As possible coherency measure candidates we tested both conventional Semblance and higher-resolution coherency measures like MUSIC, Eigen Vector (EV) and Minimum Variance (MV). The higher-resolution coherency measures, originally developed for narrowband Direction Of Arrival (DOA) estimation, were extended to handle the highly correlated and wideband seismic and GPR signals. From this extensive testing, employing both controlled data (Marmousi) as well as field data (both GPR and seismic), we concluded that the MUSIC coherency measure provides the

most optimal diffraction traveltime parameters. After separating the diffractions from the reflections by stacking along the optimized diffraction traveltime surfaces, we performed diffraction imaging using both conventional Kirchhoff migration and a new high-resolution MUSIC like imaging algorithm known as Semblance balanced MUSIC (SB-MUSIC). This new algorithm outperformed classical migration when applied to various controlled and field data.

List of Publications

This thesis is based on the following five papers, referred in the text by their corresponding Roman numerals (I-V).

I Leiv -J. Gelius and Endrias G. Asgedom, "Diffraction-limited imaging and beyond - the concept of super resolution," *Geophysical Prospecting*, vol. 59 no. 3, pp. 400-421, 2011 (Lorand Eötvös Award 2012 from EAGE for best paper in Geophysical Prospecting).

II Endrias G. Asgedom, Leiv -J. Gelius and Martin Tygel, "Higher-Resolution Determination of Zero-Offset Common-Reflection-Surface Stack Parameters," *International Journal of Geophysics*, vol. 2011, 10 pages, 2011, Article ID 819831 doi:10.1155/2011/819831.

III Endrias G. Asgedom, Leiv -J. Gelius, Andreas Austeng, Sverre Holm and Martin Tygel, "Time-reversal multiple signal classification in case of noise: A phase-coherent approach," *J. Acoust. Soc. Am.*, vol. 130, no.4, pp. 2024-2034, 2011.

IV Endrias G. Asgedom, Leiv -J. Gelius and Martin Tygel, "Seismic Coherency Measures in Case of Interfering Events: A Focus on the Most Promising Candidates of Higher-Resolution Algorithms," *IEEE Signal Processing Magazine*, vol. 29, no. 3, pp. 47-56, 2012.

V Endrias G. Asgedom, Leiv -J. Gelius, and Martin Tygel, "2D Common-Offset Traveltime Based Diffraction Enhancement and Imaging," *Geophysical Prospecting*, Submitted for publication, Oct. 2012.

Related publications

i Endrias G. Asgedom and Leiv -J. Gelius, "Multi-frequency Phase Coherent Super-resolution Imaging," *Extended Abstract 72nd EAGE Conference and Exhibition*, Barcelona, Spain, June 2010.

ii Endrias G. Asgedom, Leiv J. Gelius and Martin Tygel, "On Separation of Reflections and Diffractions Using a CRS/MUSIC Approach," *Extended Abstract 73nd EAGE Conference and Exhibition*, vienna, Austria, May 2011.

iii Endrias G. Asgedom, Leiv -J. Gelius and Martin Tygel, "Diffraction Separation Using the CRS Technique: A Field Data Application," *Extended Abstract 12th International Congress of the Brazilian Geophysical Society*, Rio de Janeiro, Brazil, August 2011.

iv Endrias G. Asgedom, Leiv -J. Gelius, Andreas Austeng and Martin Tygel, "A new approach to post-stack diffraction separation," *Extended Abstract 81st SEG Conference and Exhibition*, San Antonio, USA, Sep. 2011.

v Endrias G. Asgedom, Leiv -J. Gelius and Martin Tygel, "Common-offset Diffraction Separation and Imaging with Interpretation," *Extended Abstract 74nd EAGE Conference and Exhibition*, Copenhagen, Denmark, June. 2012 (invited paper).

vi Endrias G. Asgedom, Leiv -J. Gelius, H. Faccipieri and Martin Tygel, "2-D Pre- and Post-stack diffraction separation and imaging," *Extended Abstract 82nd SEG Conference and Exhibition*, Las Vegas, USA, Nov. 2012.

Contents

1 Introduction **1**

1.1 Motivations 1

1.2 Objectives of the thesis 2

1.3 Thesis outline 2

2 Scientific Background **3**

2.1 Diffraction-limit and the concept of super-resolution 3

2.1.1 Diffraction-limited imaging 6

2.1.2 Time-reversal imaging and super-resolution 7

2.2 Coherency measures and SB-MUSIC imaging 16

2.2.1 Semblance 18

2.2.2 MUSIC 19

2.2.3 SB-MUSIC diffraction imaging 19

2.3 Diffraction separation 21

2.3.1 Diffraction separation based on modified CRS 26

2.3.2 REM based diffraction separation 27

3 Summary of publications **31**

3.1 Paper I 31

3.2 Paper II 31

3.3 Paper III 32

3.4 Paper IV 32

3.5 Paper V 33

4 Contributions and future work **35**

5 "Diffraction-limited imaging and beyond-the concept of super resolution," Leiv -J. Gelius and Endrias G. Asgedom, *Geophysical Prospecting*, vol. 59 no. 3, pp. 400-421, 2011. **41**

6 "Higher-Resolution Determination of Zero-Offset Common-Reflection-Surface Stack Parameters," Endrias G. Asgedom, Leiv -J. Gelius and Martin Tygel, *International Journal of Geophysics*, vol. 2011, 10 pages, 2011, Article ID 819831 doi:10.1155/2011/819831. **65**

7 **"Time-reversal multiple signal classification in case of noise: A phase-coherent approach,"** Endrias G. Asgedom, Leiv -J. Gelius, Andreas Austeng, Sverre Holm and Martin Tygel, *J. Acoust. Soc. Am.*, vol. 130, no.4, pp. 2024-2034, 2011. **77**

8 **"Seismic Coherency Measures in Case of Interfering Events: A Focus on the Most Promising Candidates of Higher-Resolution Algorithms,"** Endrias G. Asgedom, Leiv -J. Gelius and Martin Tygel, *IEEE Signal Processing Magazine*, vol. 29, no. 3, pp. 47-56, 2012. **91**

9 **"2D Common-Offset Traveltime Based Diffraction Enhancement and Imaging,"** Endrias G. Asgedom, Leiv -J. Gelius, and Martin Tygel, *Geophysical Prospecting*, Submitted for publication, Oct. 2012. **103**

Chapter 1

Introduction

Active sensing of the subsurface using both seismic and Ground Penetrating Radar (GPR) has the potential to give well-resolved and reliable images of underground structures. For example GPR has been used to identify buried archaeological remainences, pipes, cavities and tunnels. Seismic imaging, on the other hand, represents the major source of information about the subsurface geological structures for applications in oil exploration. In a seismic (or GPR) experiment the sources at the surface generate elastic (or electromagnetic) waves which propagate into the subsurface until they encounter a change in the elastic (or electric) properties of the earth. Such changes result in reflection, transmission, refraction and diffraction contributions that propagate back to the surface and are recorded by a receiver array. After collection of the data, various signal processing techniques are applied to increase the signal-to-noise ratio (SNR) and to remove the unwanted parts of the recorded data. Finally, imaging is performed in order to reconstruct the subsurface changes in elastic (or electric) properties. In this thesis, we cover signal processing problems like diffraction separation and coherency measures as well as super-resolution imaging. In this chapter, we introduce the main motivation behind this research and identify the main objectives. Finally, the outline of the thesis is given.

1.1 Motivations

The quest for having an imaging system with unlimited resolving power started after the observation of the moon's of Jupiter made by Galileo in 1609 using his simple refractive telescope. Since that time a wide range of imaging techniques have been developed to collect information both from the infinite universe to the interior of the earth. In case of the latter, the seismic technique has proved well when limited to the upper crust. However, just like any other wave-based technique, seismic imaging suffers from the fundamental limit of resolution. This resolution limit is known as the *diffraction-limit* characteristing any imaging system with finite aperture and bandlimited sources. To understand this fundamental limit both from a physical and mathematical point of view was the starting point of this Ph.D. thesis. The next step was to identify alternative techniques able to apparently break this diffraction-limit. This lead to the study of the time-reversal MUltiple SIgnal Classification (MUSIC) algorithm. This technique was modified further in this thesis work to handle noise and also highly correlated signals. Since this method has the potential of giving super-resolved images of scattering features, a method to separate diffractions from reflections in sesmic

data was further addressed. This is because in seismic (or GPR) diffracted signals are often much weaker than specular reflections. Therefore, a method to separate the diffracted signals from the reflected ones was needed. In this thesis, the main idea was to recognize the differences in traveltime between diffractions and reflections. We proposed to approximate the diffraction traveltimes using a parameterized analytical formulation and determined the optimal parameters using a coherency measure. In case of the parameter estimation we tested different coherency measures including MUSIC, Minimum Variance (MV), Eigen Vector (EV) and Semblance. The three first coherency measures are not well known in exploration seismology and thus required some adjustments to the wideband and highly correlated seismic (or GPR) signals.

1.2 Objectives of the thesis

The main objective of the thesis was to develop a formalism for super-resolution imaging of subsurface scattering features based on seismic and GPR data. The proposed algorithm should be highly robust to noise. To satisfy this objective we addressed the following:

(i) Identifed the main causes of diffraction-limited imaging.

(ii) Developed an imaging algorithm with super-resolution capability for resolving scattering features.

(iii) Verified the robustness of the algorithm with respect to noise and model perturbations.

(iii) Developed a technique to separate diffractions from reflections based on their kinematic differences.

(iii) Identified the most promising candidate among higher-resolution coherency measures to be used in seismic (or GPR) signal processing.

1.3 Thesis outline

The thesis is organized as follows. In Chapter 2, the basics of diffraction-limited imaging, coherency measures in seismic (or GPR) signal processing as well as the concept of seismic (or GPR) diffraction separation are introduced. In Subsections 2.1.1 and 2.1.2 we shade light on the fundamental nature of wave propagation resulting in diffraction-limited imaging and improve the concepts of time-reversal imaging and its ability to provide super-resolution. Section 2.2 is devoted to seismic coherency measures and higher-resolution diffraction imaging. In Subsections 2.2.1 and 2.2.2 we briefly revise classical Semblance and replace it with the higher-resolution coherency measure MUSIC. Combining Semblance and MUSIC in Subsection 2.2.3 we introduce a higher-resolution diffraction imaging algorithm known as Semblance balanced MUSIC (SB-MUSIC). The final section in Chapter 2 deals with diffraction traveltime approximations and diffraction separation. Two different traveltime approximations (modified CRS and REM) are introduced and the concept of how to separate diffractions from reflections is briefly addressed. Chapter 3 summarizes the five papers included in this thesis and finally Chapter 4 discusses the main contributions made followed by suggestions to possible future work.

Chapter 2

Scientific Background

This chapter provides the reader with basic scientific ideas necessary to understand the core work of this thesis. Most of the discussions are accompanied with simple numerical simulations to aid in visualizing the different mathematical formulations. The chapter is divided into three parts; the first part reviews the origin of diffraction-limited imaging and introduces super-resolution time-reversal imaging. The second part discusses different coherency measures that can be used within seismic (or GPR). The final part considers the problem of diffraction separation.

2.1 Diffraction-limit and the concept of super-resolution

In every branch of imaging (e.g. optical, acoustic, elastic or electromagnetic) the quest for understanding the fundamental limit of resolution has always been, and still is, an important issue [1]. This is partially due to the fact that numerous ways of defining the resolving power (RP) of an imaging system exist. However, the RP of a *theoretical imaging system* (i.e. one not affected by noise, source and receiver responses, attenuation, dispersion or any instrument irregularities) is ultimately characterized by diffractions [2]. This fact has resulted in the so-called classical resolution limit, as described by Rayleigh and Abbe [3, 1, 4].

The fundamental behavior of a theoretical imaging system is characterized by a RP only dependent on the shape of its diffraction pattern or what is known as the *point spread function (PSF)*. This means that the only factors affecting the RP are the physical aperture of the imaging system and the source frequency. To understand how the diffraction pattern determines the RP of an imaging system one needs to investigate the behavior of the scattered and backpropagated wavefields. Consider a scattering experiment (or system) with acoustic sources generating waves propagating in a homogeneous (possibly inhomogeneous), lossless and non-dispersive background medium embedded one or several velocity perturbations. The wavefield satisfies the Helmholtz wave equation given by (after temporal Fourier transform)

$$\nabla p^2(\mathbf{r},\omega) + k_0^2(\mathbf{r},\omega)p(\mathbf{r},\omega) = -k_0^2(\mathbf{r},\omega)\gamma(\mathbf{r})p(\mathbf{r},\omega)\ , \tag{2.1}$$

where, $p(\mathbf{r},\omega)$ is the total wavefield (incident plus scattered contributions) at the location $\mathbf{r}$, ω is the angular frequency and k_0 and γ are the background medium wavenumber and scattering potential, respectively. Solving Eq. (2.1) using Green's theorem provide us the scattered wavefield $p_s(\mathbf{r},\omega)$ associated with a given scattering potential. Mathematically, this solution is expressed using the

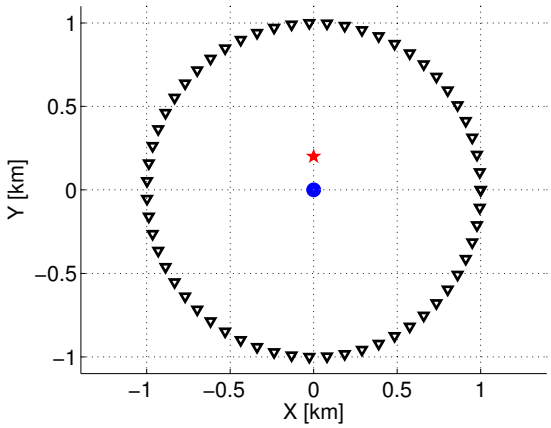

Fig. 2.1*: A 2-D slice of the acqusition geometry for the simulated acoustic scattering system. The black triangles denote the receivers, the red star represents the source and the blue circle represents the scatterer.*

Lippmann-Schwinger equation [5]

$$p_s(\mathbf{r},\omega) = \iiint_V k_0^2(\mathbf{r}',\omega) G_0(\mathbf{r},\mathbf{r}',\omega)\gamma(\mathbf{r}')p(\mathbf{r}',\omega)dV' \,, \tag{2.2}$$

where, $G_0(\mathbf{r},\mathbf{r}',\omega)$ is the background medium time-retarded Green's function from the scatterer location $\mathbf{r}'$ to the receiver point $\mathbf{r}$ and $p(\mathbf{r}',\omega)$ is the total wavefield within a volume V containing the whole scattering system.

The scattered wavefield in Eq. (2.2) can be interpreted as the result of a superposition of waves generated by a series of secondary sources each of them with a strength $k_0^2(\mathbf{r}',\omega)\gamma(\mathbf{r}')p(\mathbf{r}',\omega)$ which propagate forward in time as expressed by the time-retarded Green's function $G_0(\mathbf{r},\mathbf{r}',\omega)$. Moreover, Eq. (2.2) provides an exact representation of the scattered wavefield being a non-linear function of the scattering potential. If the scattered wavefield is small in magnitude compared to the incident field (i.e. if we consider weak scattering) we can use the first Born approximation where we replace the total wavefield in Eq. (2.2) with the incident wavefield [4].

To illustrate the fundamental properties of the scattered wavefield, we simulated an acoustic scattering system defined by a homogeneous background medium (velocity of 2000 m/s) embedded a weak point scatterer. The medium was probed with a wavefield excited by a point source with a 20 Hz center-frequency Ricker wavelet. The scattered waves were measured using an array of receivers uniformly distributed over a spherical surface (cf. Fig. 2.1). The scattered wavefield could be computed using the first Born approximation in Eq. (2.2). Let time zero represent the time when the incident field hits the scatterer. We generated three snapshots of the scattered wavefield at $t = -20$ ms (cf. Fig. 2.2(a)), $t = 0$ ms (cf. Fig. 2.2(b)) and $t = 20$ ms (cf. Fig. 2.2(c)). At the negative time the incident wavefield has not reached the scatterer and thus no scattered wavefield exists (cf. Fig. 2.2(a)). At $t = 0$ ms, the scattered wavefield starts to be generated (cf. Fig. 2.2(b)) and propagates forward in the positive time direction (cf. Fig. 2.2(c)). Therefore, the scattered wavefield represents a causal phenomenon (i.e. it only exists for time $t \geq 0$).

To further understand the concept of diffraction-limited imaging, we introduce the corresponding backpropagated (or extrapolated) wavefield. This wavefield is generated by backpropagating the

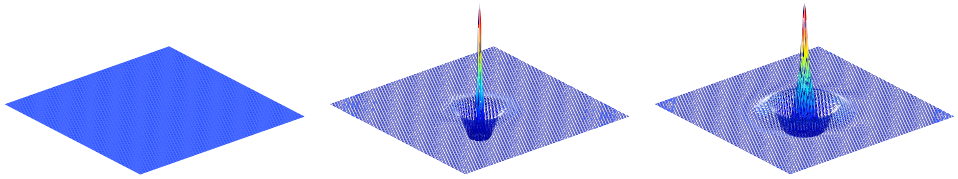

Fig. 2.2: *Snapshots of the scattered wavefield at (a)* $t = -20$ *ms, (b)* $t = 0$ *sec and (c)* $t = 20$ *ms.*

scattered wavefield recorded at the receiver array towards the scatterer(s). Following the approach of [6], the backpropagated wavefield can be represented in terms of the volume integral

$$p_{bp}(\mathbf{r},\omega) = \iiint_V k_0^2(\mathbf{r}',\omega)B(\mathbf{r},\mathbf{r}',\omega)\gamma(\mathbf{r}')p(\mathbf{r}',\omega)dV' \,, \tag{2.3}$$

where, $B(\mathbf{r},\mathbf{r}',\omega)$ is the backpropagation kernel. Ideally, at a given receiver location $\mathbf{r}$ the backpropagated wavefield and the scattered wavefield should be the same. However, direct comparison between Eqs. (2.2) and (2.3) shows that this is not the case due to different integration kernels ($G_0(\mathbf{r},\mathbf{r}',\omega)$ and $B(\mathbf{r},\mathbf{r}',\omega)$ respectively).

In case of a complete aperture, like the one in Fig. 2.1 where the receiver array completely surrounds the scatterer, the backpropagation kernel is simply expressed as the superposition of the time-retarded and time-advanced Green's functions [7]

$$B(\mathbf{r},\mathbf{r}',\omega) = G_0(\mathbf{r},\mathbf{r}',\omega) - G_0^*(\mathbf{r},\mathbf{r}',\omega) \,, \tag{2.4}$$

where $G_0^*(\mathbf{r},\mathbf{r}',\omega)$ is the the time-advanced Green's function. Combination of Eqs. (2.3) and (2.4) together with Eq. (2.2) gives

$$p_{bp}(\mathbf{r},\omega) = \begin{cases} p_s(\mathbf{r},\omega) - p_s^*(\mathbf{r},\omega) \,; & \mathbf{r} \in V \\ -p_s^*(\mathbf{r},\omega) \,; & \text{otherwise} \,, \end{cases}$$

with the time-advanced scattered wavefield $p_s^*(\mathbf{r},\omega)$ defined as

$$p_s^*(\mathbf{r},\omega) = \iiint_V k_0^2(\mathbf{r}',\omega)G_0^*(\mathbf{r},\mathbf{r}',\omega)\gamma(\mathbf{r}')p(\mathbf{r}',\omega)dV' \,. \tag{2.5}$$

The artificial wavefield $p_s^*(\mathbf{r},\omega)$ can be interpreted as the time-reverse of the physical scattered wavefield $p_s(\mathbf{r},\omega)$ and will therefore lead to non-causal contributions. It is the interaction between $p_s(\mathbf{r},\omega)$ and $p_s^*(\mathbf{r},\omega)$ which gives the diffraction-limited focus at the scatterer. This can be further seen as follows.

For $\mathbf{r} \in V$, Eq. (2.4) can be simplified as

$$B(\mathbf{r},\mathbf{r}',\omega) = 2i(imag[G_0(\mathbf{r},\mathbf{r}',\omega)]) \,, \tag{2.6}$$

where $i = \sqrt{-1}$ and $imag[G_0(\mathbf{r},\mathbf{r}',\omega)]$ denotes the imaginary part of the the time-retarded Green's function (corresponds to an impulse response which is odd-symmetric in time). Now, substituting

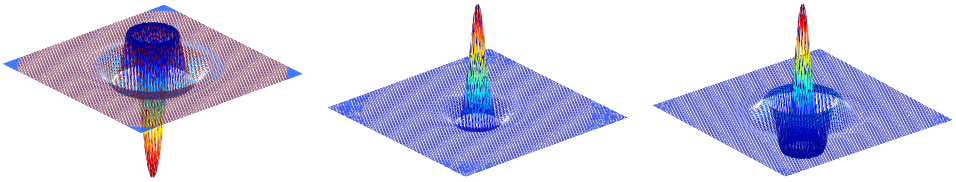

(a) (b) (c)

Fig. 2.3*: Snapshots of the backpropagated wavefield at (a) $t = -20$ ms, (b) $t = 0$ ms and (c) $t = 20$ ms.*

Eq. (2.6) into Eq. (2.3) gives

$$p_{bp}(\mathbf{r},\omega) = 2i \iiint_V k_0^2(\mathbf{r}',\omega)(imag[G_0(\mathbf{r},\mathbf{r}',\omega)])\gamma(\mathbf{r}')p(\mathbf{r}',\omega)dV' \,. \tag{2.7}$$

Due to the odd-symmetric nature of the imaginary part of the Green's function, the backpropagated wavefield becomes anti-causal with contributions propagating both in the negative and positive direction.

Figure 2.3 illustrates the backpropagated version of the scattered wavefield shown in Fig. 2.1. It can be easily observed that a non-causal contribution is present at the negative time. Also at time zero the waves do no longer form "singularity" as in Fig. 2.2(b), but represents an interaction between the converging and diverging fields.

2.1.1 Diffraction-limited imaging

An estimate or image of the scattering potential can be obtained from an imaging condition stating the coincidence of incident and scattered waves [6, 7]

$$\langle\gamma(\mathbf{r})\rangle \cong \frac{1}{\pi}\int_{\Delta\omega}\frac{p_{bp}(\mathbf{r},\omega)}{i\omega p(\mathbf{r},\omega)}d\omega = \iiint_V \gamma(\mathbf{r}')\Gamma(\mathbf{r},\mathbf{r}')dV' \,, \tag{2.8}$$

where, $\Gamma(\mathbf{r},\mathbf{r}')$ is the *point spread function (PSF)* of the scattering system. The PSF can be interpreted as a filter that smoothens the scattering potential. As can be seen from Eq. (2.8), the RP of the imaging system is only dependent on its PSF. Use of Eqs. (2.3) and (2.4) in combination with Eq. (2.8) (also assuming $\frac{p(\mathbf{r}',\omega)}{p(\mathbf{r},\omega)} \cong 1$ due to the typical behaviour of a PSF) gives the explicit expression for the point spread function

$$\Gamma(\mathbf{r},\mathbf{r}') = \frac{2}{\pi}\int_{\Delta\omega}\frac{k_0^2(\mathbf{r}',\omega)}{\omega}\left[G_0(\mathbf{r},\mathbf{r}',\omega) - G_0^*(\mathbf{r},\mathbf{r}',\omega)\right]d\omega \,. \tag{2.9}$$

The PSF can now be interpreted as an interaction between a converging (due to $G_0^*(\mathbf{r},\mathbf{r}',\omega)$) and diverging (due to $G_0(\mathbf{r},\mathbf{r}',\omega)$) wave. The superposition of these two waves results in a *diffraction-limited* focus at the scatterer location. This is in accordance with our earlier observations that the backpropagated wavefield contains both time-retarded and time-advanced components at zero time. This lack of perfect focusing of the backpropagated wavefield is caused by the fact that the scattered wavefield recorded at the receivers does not contain evanescent contributions [7].

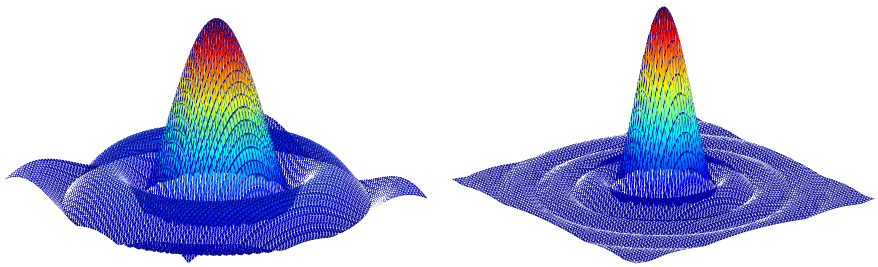

(a) (b)

Fig. 2.4*: The PSF computed for the scattering system in Fig. 2.1 at a frequency of (a)* 20 *Hz and (b) using a band between* $0 - 40$ *Hz.*

Figures 2.4(a) and 2.4(b) show the PSF computed using Eq. (2.9) for a single frequency of 20 Hz and a band of frequencies between $0 - 40$ Hz, respectively. In both cases, the PSF shows a characteristic *mainlobe* of a certain width and *sidelobes* of certain heights. In case of a band of frequencies, the mainlobe width of the PSF is narrower than the single frequency case, resulting in a better RP. Based on the observation of such a PSF pattern, Rayleigh's criterion for resolving two point scatterers states that: *the scatterers are resolved if the mainlobe peak of one PSF falls on the first zero crossing of the other PSF*. Hence, for a full aperture scattering system, Rayleigh's criterion puts a resolution-limit of $\lambda/2$ (where λ being the wavelength).

Until now we have investigated the problem of diffraction-limited imaging from a complete aperture point of view. However, a limited acquisition geometry is often more likely in reality. The effect that a limited aperture has on the PSF of the imaging system is illustrated in Figure 2.5, where two acquisition geometries are considered; one with receivers uniformly distributed over half of a spherical surface (cf. Fig. 2.5(a)) and another with receivers uniformly distributed over quarter of a spherical surface (cf. Fig. 2.5(b)). For both cases the PSF was computed using a band of frequencies between 0 and 40 Hz (cf. Figs. 2.5(c) and 2.5(d)). On comparison with Fig. 2.4(b), we can clearly see that the mainlobes become wider and the sidelobes become heigher as the aperture becomes more limited. As a consequence, the more limited aperture the more is the RP of the imaging system reduced. In general, in order to obtain an ideal RP one needs a scattering system with full aperture and infinite bandwidth source(s).

2.1.2 Time-reversal imaging and super-resolution

During the years, several attempts have been made to beat the diffraction limit in order to be able to visualize features within sub-wavelength scale. Most of these works are based on the principle of measuring the evanescent components of the wavefield. However, this is not feasible within seismic since both sources and receivers are placed many wavelengths away from the target area(s), and the corresponding evanescent waves fall below the noise threshold. In this section, an alternative approach is introduced based on the time-reversal Multiple SIgnal Classification (MUSIC) algorithm. This technique has a resolving power beyond the diffraction-limit in case of point-like scatterers.

In the following assume a monochromatic case and consider a scattering system with a multiple number of point sources with spectra $S_i(\omega)$, $i = 1, 2, ..., N_s$ each of them exciting waves propa-

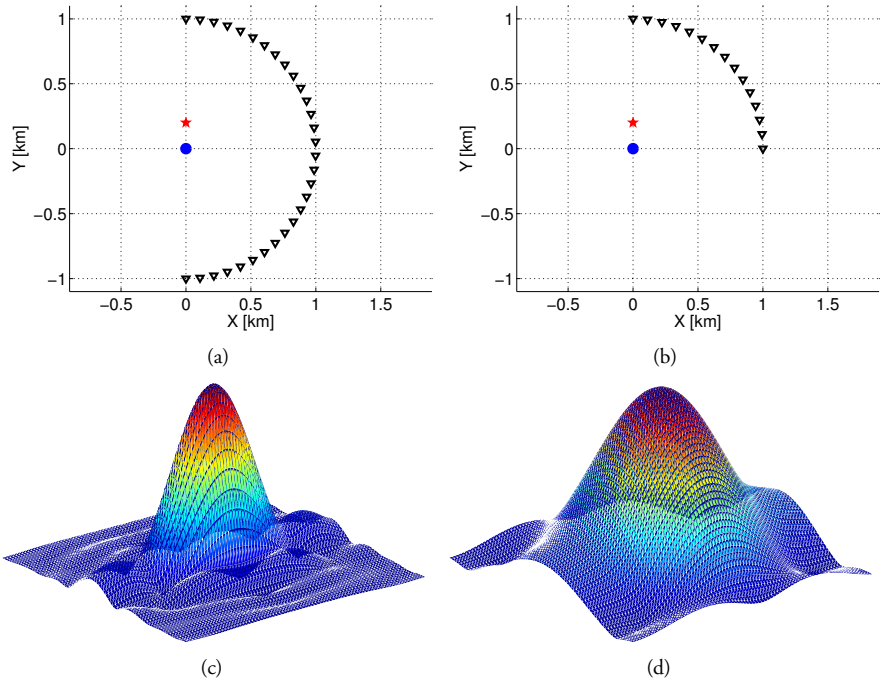

Fig. 2.5*: A 2-D slice of the acquisition geometry for a half spherical (a) and quarter of a spherical (b) receiver surface. (c) and (d) show the corresponding PSF computed using a band of frequencies between* $0 - 40$ *Hz.*

gating into a lossless homogeneous (possibly inhomogeneous) background medium with M point scatterers embedded. The scattered wave contributions are measured by a series of receivers $r_j(\omega)$, $j = 1, 2, ..., N_r$. In the following let $\boldsymbol{\alpha}_i$ represent the location of the i^{th} source, $\boldsymbol{\beta}_j$ represent the location of the j^{th} receiver and $\mathbf{x}_m$ denotes the location of the m^{th} scatterer. The recorded wavefield at the receiver $r_j(\omega)$ can formally be written as

$$r_j(\omega) = \sum_{i=1}^{N_s} k_{j,i}(\omega) S_i(\omega) \ , \tag{2.10}$$

where $k_{j,i}(\omega)$ is an element of the *multistatic response (MSR)* matrix $\mathbf{K}(\omega)$ and defined as

$$k_{j,i}(\omega) = \sum_{m=1}^{M} \gamma_m G_0(\boldsymbol{\beta}_j, \mathbf{x}_m) G_0(\mathbf{x}_m, \boldsymbol{\alpha}_i) \ . \tag{2.11}$$

In Eq. (2.11) the two Green's functions represent propagations from a fixed receiver at $\boldsymbol{\beta}_j$ to a given scatterer at $\mathbf{x}_m$ and from the same scatterer to a fixed source at $\boldsymbol{\alpha}_i$ (all propagations in the background medium). To further simplify the analysis we introduce the two Green's function vectors associated with respectively receiver and source side

$$\begin{aligned} g_{0r}(\mathbf{x}_m) &= \left[G_0(\boldsymbol{\beta}_1, \mathbf{x}_m), G_0(\boldsymbol{\beta}_2, \mathbf{x}_m), ..., G_0(\boldsymbol{\beta}_{N_r}, \mathbf{x}_m)\right] \\ g_{0s}(\mathbf{x}_m) &= \left[G_0(\boldsymbol{\alpha}_1, \mathbf{x}_m), G_0(\boldsymbol{\alpha}_2, \mathbf{x}_m), ..., G_0(\boldsymbol{\alpha}_{N_r}, \mathbf{x}_m)\right] \ . \end{aligned} \tag{2.12}$$

Based on Eqs. (2.11) and (2.12) the MSR matrix can be written as

$$\mathbf{K}(\omega) = \sum_{m=1}^{M} \gamma_m g_{0r}(\mathbf{x}_m) g_{0s}^T(\mathbf{x}_m) \ . \tag{2.13}$$

Mathematically, the MSR matrix $\mathbf{K}(\omega)$ represents a linear transformation (or mapping) from the complex N_s dimensional space spanned by the source side Green's functions to the N_r dimensional complex space spanned by the receiver side Green's functions. Thus, we can perform a singular value decomposition (SVD) of $\mathbf{K}(\omega)$ to obtain

$$\mathbf{K}(\omega) = \mathbf{U}_s(\omega) \boldsymbol{\Sigma}_s(\omega) \mathbf{V}_s^{\dagger}(\omega) + \mathbf{U}_n(\omega) \boldsymbol{\Sigma}_n(\omega) \mathbf{V}_n^{\dagger}(\omega) \ , \tag{2.14}$$

where $\mathbf{U}(\omega)$ ($\mathbf{V}(\omega)$) is the receiver (source) side singular matrix containing the column receiver (source) side singular vectors $\mathbf{u} \in C^{N_r}$ ($\mathbf{v} \in C^{N_s}$). The sub-scripts s and n denote respectively the signal and noise sub-spaces and $\dagger$ is the Hermitian operator. Moreover, $\boldsymbol{\Sigma}(\omega)$ represents the diagonal singular value matrix. The SVD transforms the active experiment into two purely passive experiments where the scatterers become secondary sources and the associated waves are recorded at the orignal source and receiver lines. In addition, these responses are decomposed into *signal sub-space* and *noise sub-space* components. The signal sub-space contributions are associated with the M number of scatterers while the noise sub-space is associated with the nill solutions (overdetermined system assumed). In case of an ideally resolved case with well separated scatterers, the SVD will give M non-zero singular value contributions (signal sub-space) with corresponding singular vectors $\mathbf{u}_m \propto g_{0r}(\mathbf{x}_m)$ and $\mathbf{v}_m^* \propto g_{0s}(\mathbf{x}_m)$, $m = 1, 2, ..., M$.

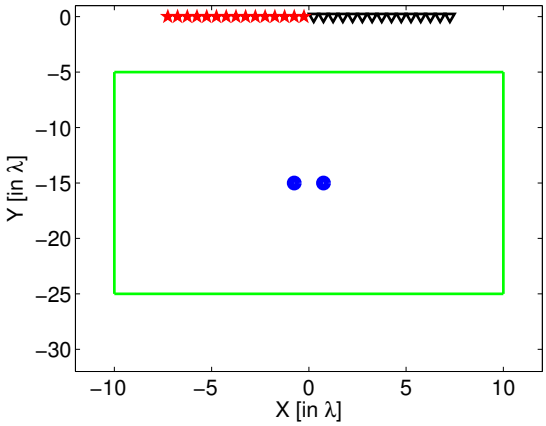

Fig. 2.6: *Geometry in case of* 15*-element source (red) and receiver (black) arrays and two point scatterers (blue). The green rectangle defines the boundaries of the actual image.*

Time-reversal monochromatic images with respect to both the source and receiver side array can now be formed employing the formulas

$$\begin{aligned} I(\mathbf{r};\boldsymbol{\beta}) &= \|g_{0r}(\mathbf{r})^{\dagger}\mathbf{U}_s(\omega)\|^2 \\ I(\mathbf{r};\boldsymbol{\alpha}) &= \|g_{0s}(\mathbf{r})^{T}\mathbf{V}_s(\omega)\|^2 \,, \end{aligned} \tag{2.15}$$

which will focus at each scatterer location. Combined source and receiver side images can also be formed employing the expression [8]

$$\mathbf{I}(\mathbf{r}) = \|g_{0r}(\mathbf{r})^{\dagger}\mathbf{U}_s(\omega)\|^2 + \|g_{0s}(\mathbf{r})^{T}\mathbf{V}_s(\omega)\|^2 \,, \tag{2.16}$$

or alternatively [9]

$$\mathbf{I}(\mathbf{r}) = g_{0r}(\mathbf{r})^{\dagger}\left(\mathbf{U}_s(\omega)\mathbf{V}_s^{\dagger}(\omega)\right) g_{0s}^{*}(\mathbf{r}) \,. \tag{2.17}$$

The latter expression also contains phase information. Thus it can be used to carry out phase-coherent multi-frequency imaging [9, 10].

The key question is now what will happen with the time-reversal technique if scatterers are so close that they start to interact with each others. To investigate this matter we generated synthetic data using the Foldy-Lax model [11] for a scattering system composed of two point scatterers embedded in a homogeneous background with a constant acoustic velocity of 2000 m/s. The source and receiver arrays consisted each of 15 elements. A source signal represented by a Ricker wavelet with a 20 Hz center-frequency was used. The two scatterers were separated by 150 m $= 1.5\lambda_d$ (λ_d being the dominant wavelength) and placed at a distance of $15\lambda_d$ away from the source and receiver lines (cf. Fig. 2.6).

Scattered data were computed in the time-domain (Foldy-Lax) and monochromatic data were obtained using the Fourier transform. For each frequency a SVD of the monochromatic MSR matrix was carried out. Since this is a two scatterers experiment, only two non-zero singular values will dominate. Figure 2.7 shows a plot of these singular values for various frequencies within the dominant band of the source pulse. The pattern of the two large singular values as a function of

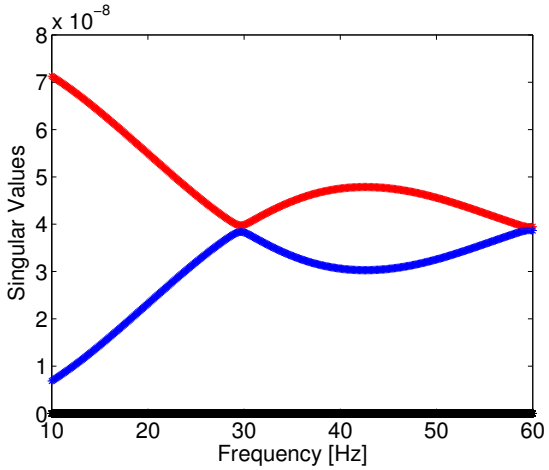

Fig. 2.7*: Singular values of the MSR matrix as a function of frequency. The red and blue curves represent the two large singular values while the black curve denotes the rest of the singular values corresponding to the nill solutions.*

frequency indicates the presence of Foldy-Lax type of interaction between the two scatterers.

The classical resolution limit δ for a given linear array is given by the Rayleigh criterion

$$\delta = \frac{R\lambda}{D} \,, \tag{2.18}$$

where D is the aperture of the array and R is the range. In the current example $\delta \approxeq 2.14\lambda_d$ and the distance between the two scatterers is 150 m. In the following, we therefore limit the upper frequency to 25 Hz in order to ensure a diffraction-limited case.

First we considered time-reversal imaging at the center-frequency of 20 Hz. To investigate the information carried by each of the signal sub-space singular vectors corresponding to the two large singular values, monochromatic time-reversal images were calculated for respectively the first set (cf. Fig. 2.8(a)), the second set (cf. Fig. 2.8(b)) and the combined set (cf. Fig. 2.8(c)) of the singular vectors. Because of the interaction between the scatterers and the diffraction-limited nature of the experiment, none of the singular values map uniquely to a specific scatterer. However, the combined information from both singular-vector sets results in an image that focuses on each scatterer (cf. Fig. 2.8(c)). By including a band of frequencies between 15 and 25 Hz, the latter image is replaced by that shown in Fig. 2.9(a) or 2.9(c) demonstrating again that the two scatterers can be discriminated. Application of prestack Kirchhoff depth migration (without weights) to the same frequency band of data gave the image shown in Fig. 2.9(b) or 2.9(d). As expected, the two scatterers can not be resolved due to the diffraction-limited geometry (cf. discussion in Section 2.1.1). The results obtained employing the time-reversal technique are of higher resolution than standard migration, but still not of super-resolved quality (i.e. with a resolution beyond the classical resolution limit of $\lambda/2$). This can be seen from Fig. 2.9(a) where the circle surrounding each scatterer location has a radius of $\lambda/2$ (with λ representing the wavelength corresponding to the center-frequency of 20 Hz). However, a super-resolution version of the time-reversal algorithm can

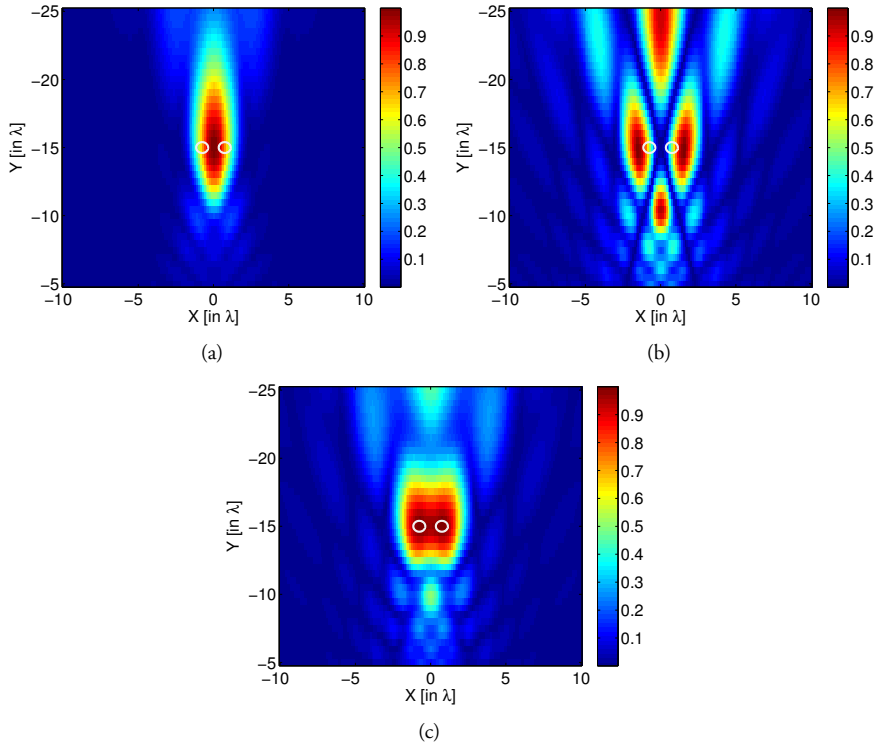

Fig. 2.8: *Time-reversal images computed at a frequency of* 20 *Hz using (a) the first set, (b) the second set and (c) combined set of the singular vectors. The two circles surrounding the two scatterers have a radius of* $\lambda/2$*, where* λ *corresponds to the center frequency of* 20 *Hz.*

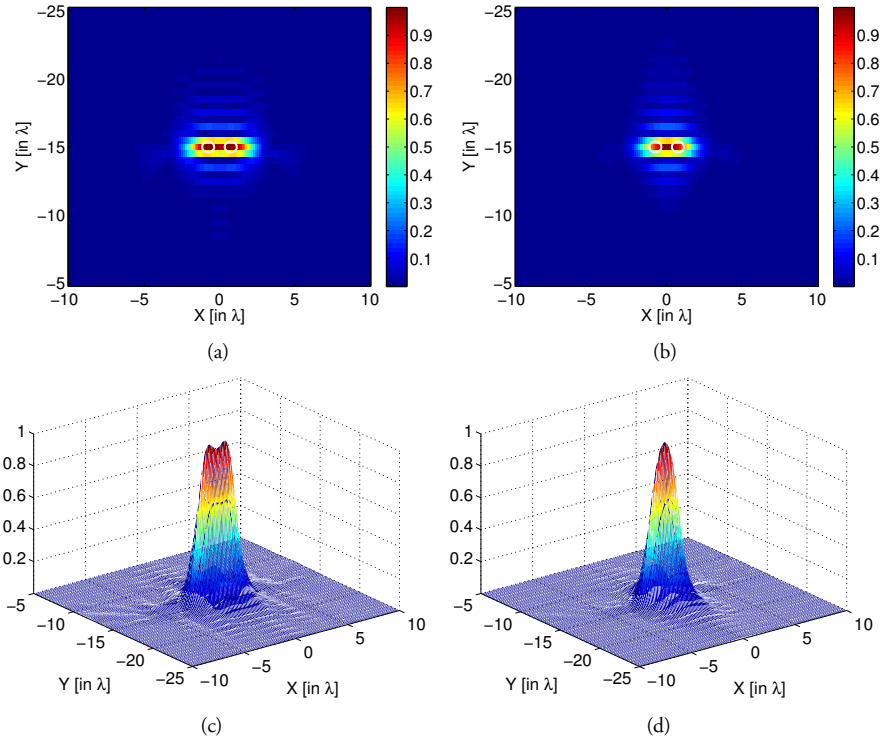

Fig. 2.9: *(a) Time-reversal and (b) Kirchhoff migration results for a band of frequencies between* 15 *and* 25 *Hz. Figures (c) and (d) show* 3D *views of the same results. The two circles surrounding the two scatterers have a radius of* $\lambda/2$*, where* λ *is computed for a frequency of* 25 *Hz.*

be constructed and is known in the literature as time-reversal MUSIC [12]. The main idea behind time-reversal MUSIC is that all the signal sub-space singular vectors and the Green's functions of the background medium span the signal sub-space while the noise sub-space singular vectors span the noise sub-space which is orthogonal to the signal sub-space. This implies that the signal sub-space singular vectors are linear combinations of the Green's functions of the background medium. Therefore, taking the inner product between these Green's function at each scatterer location $\mathbf{x}_m$ with the noise sub-space singular vectors (or projecting the Green's function onto the noise sub-space) will result in a nill value

$$\begin{aligned} g_{0r}(\mathbf{x}_m)^\dagger \left[\mathbf{U}_n(\omega)\mathbf{U}_n^\dagger(\omega)\right] g_{0r}(\mathbf{x}_m) &= 0 \\ g_{0s}(\mathbf{x}_m)^T \left[\mathbf{V}_n(\omega)\mathbf{V}_n^\dagger(\omega)\right] g_{0s}^*(\mathbf{x}_m) &= 0\,, \end{aligned} \tag{2.19}$$

where $\left[\mathbf{U}_n(\omega)\mathbf{U}_n^\dagger(\omega)\right]$ and $\left[\mathbf{V}_n(\omega)\mathbf{V}_n^\dagger(\omega)\right]$ are the receiver and source side noise sub-space projection matrices, respectively. Based on these observations, the MUSIC pseudo-spectra can be formed as

$$\begin{aligned} \mathbf{P}(\mathbf{r};\boldsymbol{\beta}) &= \frac{\|g_{0r}(\mathbf{r})\|}{g_{0r}(\mathbf{r})^\dagger \left[\mathbf{U}_n(\omega)\mathbf{U}_n^\dagger(\omega)\right] g_{0r}(\mathbf{r})} \\ \mathbf{P}(\mathbf{r};\boldsymbol{\alpha}) &= \frac{\|g_{0s}(\mathbf{r})\|}{g_{0s}(\mathbf{r})^T \left[\mathbf{V}_n(\omega)\mathbf{V}_n^\dagger(\omega)\right] g_{0s}^*(\mathbf{r})}\,, \end{aligned} \tag{2.20}$$

where $\mathbf{P}_r(\mathbf{r};\boldsymbol{\beta})$ and $\mathbf{P}_s(\mathbf{r};\boldsymbol{\alpha})$ are respectively the receiver and source side MUSIC pseudo-spectrum which will peak at the scatterer locations (ideally go to infinity). The super-resolution characteristics of time-reversal MUSIC has been demonstrated both computationally [12, 8, 11] as well as experimentally [13]. In practice, time-reversal MUSIC is quite senstive to noise especially for limited acquisition geometries [7]. The standard formulation as given by Eq. (2.20) contains no phase information. Thus, summation over a band of frequencies will not increase the signal-to-noise ratio in case of random noise. In this thesis work a novel phase-coherent MUSIC (PC-MUSIC) algorithm has therefore been developed [10]. The main idea is to carry out the time-reversal operation employing a mixed phase-preserving operator as shown in Eq. (2.17). In case of a band of frequencies $\Delta\omega$, the phase-coherent time-reversal image can be computed as (N_ω being number of frequency components)

$$\mathbf{I}_{PC}(\mathbf{r},\Delta\omega) = \frac{1}{N_\omega}\sum_{\Delta\omega} \frac{g_{0r}(\mathbf{r})^\dagger \left(\mathbf{U}_s(\omega)\mathbf{V}_s^\dagger(\omega)\right) g_{0s}^*(\mathbf{r})}{\|g_{0r}(\mathbf{r})\|\|g_{0s}(\mathbf{r})\|}\,, \tag{2.21}$$

and the corresponding PC-MUSIC pseudo-spectrum will read [10]

$$\mathbf{P}(\mathbf{r}) = \frac{1}{1-\mathbf{I}_{PC}(\mathbf{r},\Delta\omega)}\,. \tag{2.22}$$

To illustrate the advantages of PC-MUSIC, we used the same scattering data as in Fig. 2.6 and added white Gaussian random noise with a variance of 50% of the recorded signal energy in the time domain. Figures 2.10(a) and 2.10(b) show respectively the time-reversal MUSIC and the PC-MUSIC pseudo-spectra for a band of frequencies between 15 and 25 Hz. Due to the noise present,

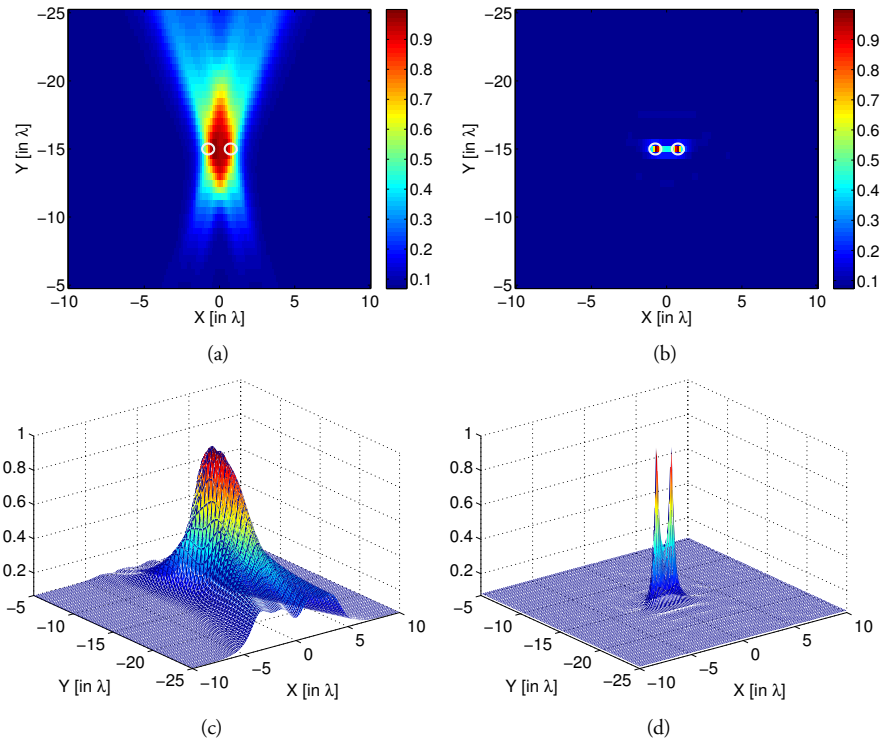

Fig. 2.10: *(a) Time-reversal MUSIC and (b) PC-MUSIC results for a band of frequencies between* 15 *and* 25 *Hz. Figues (c) and (d) show* 3*D view of the same results in (a) and (b). The two circles surrounding the two scatterers have a radius of* $\lambda/2$*, where* λ *is computed for a frequency of* 25 *Hz.*

the time-reversal MUSIC has lost its super-resolution property and could not distingush the two scatterers (cf. Figs. 2.10(a) and 2.10(c)). PC-MUSIC, however, has a super-resolution capability even in the presence of noise, which can be seen from Fig. 2.10(b) where the focusing spot of each scatterer is smaller than the diffraction-limit of $\lambda/2$ (with λ representing the wavelength computed for a frequency of 25 Hz).

PC-MUSIC and also standard time-reversal MUSIC do not give reliable amplitude information as in more conventional imaging like migration. These types of techniques can be regarded as extreme localization methods, but the amplitudes can be balanced when combined with more standard imaging. The practical use of PC-MUSIC within seismic relies on:

(i) Ability to separate diffractions (carrying the sub-wavelength information) from reflections. This is discussed in Section 2.3.

(ii) Use of time-gated data (corresponding to target area(s)) to ensure the needed sparsity.

In the next Section, the classical MUSIC algorithm will be briefly disscussed. It can be regarded as a high-coherency measure which easily outperform Semblance normally employed in seismic. The use of the classical MUSIC concept in this thesis work has been (with some additional modifications):

(i) To construct a high-resolution imaging technique denoted Semblance balanced MUSIC (SB-MUSIC) imaging which is conceptually simpler than PC-MUSIC [14, 15].

(ii) To be able to carry out the diffraction separation with a higher accuracy (resolving power) [16].

2.2 Coherency measures and SB-MUSIC imaging

Coherence is a mathematical measure of similarity [17]. In seismic signal processing, coherency (or similarity) measures have many important applications. They are used to determine the subsurface velocity, to estimate traveltime parameters, to detect event discontinuities and determine the signal-to-noise ratio (SNR) among others [18, 19, 20, 21, 22]. The coherency measures discussed here are developed based on the data covariance matrix. This matrix contains the second order statistics providing independent measures of information about the data. Unlike the Fourier transform which provides one-to-one mapping of the data, the data covariance matrix provides many-to-one mapping and hence compresses the voluminous data into a much smaller subset, but still sufficient to adequately estimate the desired unknown data parameters [22].

We start by defining the signal model required for constructing the different coherency measures. The recorded data vector $\mathbf{d}(t)$ is modeled as a linear combination between the N_s signals $s_j(t), j = 1, 2, ..., N_s$ and the additive noise vector $\mathbf{n}(t)$. Mathematically this can be stated as

$$\mathbf{d}(t) = \sum_{j=1}^{N_s} s_j(t - \tau_j(\boldsymbol{\theta})) + \mathbf{n}(t) \ , \tag{2.23}$$

where, $\tau_j(\boldsymbol{\theta})$ denotes the traveltime of the j^{th} event and is described by a function of one or more parameters $\boldsymbol{\theta}$. Our main goal now is to determine the optimal traveltime parameters $\boldsymbol{\theta}$ from the data. In seismic we often perform the parameter search within an analysis window usually arranged to follow the events in the data (cf. Fig. 2.11). The $N_t \times M$ data matrix (where N_t is the number of time samples and M is the number of traces) corresponding to the analysis window represents the steered data and is denoted by $\mathbf{D}(\boldsymbol{\theta})$. Assuming zero-mean and stationary signals within the selected analysis window the corresponding covariance matrix $\mathbf{R}(\boldsymbol{\theta})$ is given by

$$\mathbf{R}(\boldsymbol{\theta}) = E\{\mathbf{D}(\boldsymbol{\theta})\mathbf{D}(\boldsymbol{\theta})^\dagger\} = \mathbf{R}_s(\boldsymbol{\theta}) + \mathbf{R}_n(\boldsymbol{\theta}) \ , \tag{2.24}$$

where $\mathbf{R}_s(\boldsymbol{\theta})$ and $\mathbf{R}_n(\boldsymbol{\theta})$ are the steered signal and noise covariance matrices, respectively. Moreover, $E\{\}$ represents the expectation operator. In practice the true covariance matrix based on Eq. (2.24) is not available; therefore, it is replaced by its maximum likelihood estimate

$$\mathbf{R}(\boldsymbol{\theta}) = \frac{1}{N_t}\mathbf{D}(\boldsymbol{\theta})\mathbf{D}(\boldsymbol{\theta})^\dagger \ , \tag{2.25}$$

which provides the data covariance matrix as a result of averaging over the array temporal snapshots.

We will now discuss some important characteristics of the data covariance matrix. Consider the case of a perfectly aligned event (or signal) within the anaysis window (cf. Fig. 2.11) with superimposed random white Gaussian noise with a variance of σ_n^2. For such a case, we can express

the data covariance matrix as

$$\mathbf{R}(\boldsymbol{\theta}) = \|\mathbf{s}\|^2 \mathbf{u}\mathbf{u}^\dagger + \sigma_n^2 \mathbf{I}\,, \tag{2.26}$$

where $\mathbf{s}$ is the $N_t \times 1$ signal vector, $\mathbf{u} = [1, 1, ..., 1]^T$ is a unitary $M \times 1$ column vector and $\mathbf{I}$ is a $M \times M$ identity matrix. The signal part of the data covariance matrix $\mathbf{R}_s(\boldsymbol{\theta}) = \|\mathbf{s}\|^2 \mathbf{u}\mathbf{u}^\dagger$ is an $M \times M$ matrix with a rank of unity and the corresponding noise part $\mathbf{R}_n(\boldsymbol{\theta}) = \sigma_n^2 \mathbf{I}$ is also an $M \times M$ matrix but has a full rank. Therefore, once we know the Eigenvectors and Eigenvalues of $\mathbf{R}_s(\boldsymbol{\theta})$ and $\mathbf{R}_n(\boldsymbol{\theta})$, we can easily determine the corresponding Eigenvectors and Eigenvalues of $\mathbf{R}(\boldsymbol{\theta})$ or vice versa.

The Eigendecomposition of $\mathbf{R}(\boldsymbol{\theta})$ is mathematically defined as

$$\mathbf{R}(\boldsymbol{\theta}) = \mathbf{V}_s(\boldsymbol{\theta}) \boldsymbol{\Sigma}_s(\boldsymbol{\theta}) \mathbf{V}_s(\boldsymbol{\theta})^H + \mathbf{V}_n(\boldsymbol{\theta}) \boldsymbol{\Sigma}_n(\boldsymbol{\theta}) \mathbf{V}_n(\boldsymbol{\theta})^H\,, \tag{2.27}$$

where $\mathbf{V}$ and $\boldsymbol{\Sigma}$ are respectively the Eigenvector and Eigenvalue matrices (subscripts n and s denote noise and signal sub-spaces,respectively). Based on this definition, the Eigendecomposition of $\mathbf{R}(\boldsymbol{\theta})$ have the following properties:

(i) The largest Eigenvalue is equal to $M\|\mathbf{s}\|^2 + \sigma_n^2$ and the associated Eigenvector $\mathbf{v}_1 = \frac{1}{\sqrt{M}}\mathbf{u}$ spans the signal-and-noise sub-space (we denote this simply as signal sub-space).

(ii) The smallest $M-1$ Eigenvalues of $\mathbf{R}(\boldsymbol{\theta})$ are equal to σ_n^2 and the corresponding Eigenvectors span the noise sub-space.

(iii) The Eigenvectors spanning the signal and noise sub-spaces are orthogonal to each other.

Now consider the presence of more than one event (or signal) within the analysis window. Depending on the degree of correlation between the events, the rank of the signal space covariance matrix $\mathbf{R}_s(\boldsymbol{\theta})$ will vary from one (when they are completly correlated) to a value equal to the number of signals present (when they are uncorrelated). Hence, correlated signals introduce a rank deficiency in $\mathbf{R}_s(\boldsymbol{\theta})$ that results in a mixing between its (or that of $\mathbf{R}(\boldsymbol{\theta})$) signal and noise sub-spaces. In order to handle this problem, spatial smoothing of the data covariance matrix can be employed [23, 22]. The idea is that the M elements of the array are subdivided into L overlapping subarrays, each with P elements. Using the data from each subarray, L data covariance matrices are estimated, each of dimension $P \times P$. This spatially-smoothed data covariance matrix is given by

$$\mathbf{R}_L = \frac{1}{L} \sum_{l=1}^{L} \mathbf{R}_l\,. \tag{2.28}$$

In addition to minimizing the problem of correlated signals, spatial smoothing also adds statistical stability to the covariance matrix estimate. However, spatial smoothing reduces the number of array elements used for measuring coherency, therefore the resolution ability is also reduced. Hence, a compromise must be made before utilizing spatial smoothing of a certain subarray size.

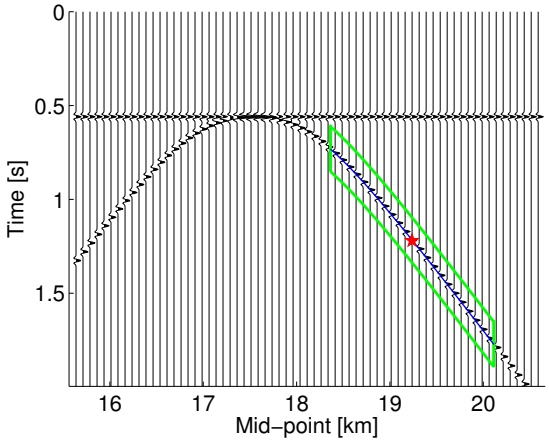

Fig. 2.11*: Synthetic data example. The blue curve represents the traveltime constructed by some trial parameters for the point* (t_0, m_0) *denoted by the red star. The green curves define the analysis window corresponding to the trial traveltimes.*

2.2.1 Semblance

Semblance is a measure of similarity or likeness defined as a normalized output/input energy ratio. Here, the output is the sum of the input traces present within the analysis window. The Semblance coherency measure described in terms of the covariance matrix of the data can be written as [21]

$$S = \frac{\mathbf{u}^H \mathbf{R}(\boldsymbol{\theta})\mathbf{u}}{M tr\{\mathbf{R}(\boldsymbol{\theta})\}} \,, \tag{2.29}$$

where $tr\{\}$ denots the trace of a matrix. The Semblance value varies between 0 and 1. A value close to one means that the different traces within the selected analysis window are highly correlated while a value close to zero corresponds to highly random events.

Making use of the fact that the sum of all the Eigenvalues of a matrix is the same as its trace value and employing Eqs. (2.27) and (2.29) assuming the case of a perfectly flat single event within the analysis window, Semblance reduces to

$$\begin{aligned} S &= \frac{\lambda_1}{\sum_{i=1}^{M} \lambda_i} \\ &= \frac{1}{1 - \sum_{i=2}^{M} \frac{\lambda_i}{\lambda_1}} \,, \end{aligned} \tag{2.30}$$

where λ_1 is the largest Eigenvalue of $\mathbf{R}(\boldsymbol{\theta})$. Here, the Semblance value is highly determined by the SNR (or the summed noise space to signal space Eigenvalue ratio). However, if we consider the case of a non-flat event within the analysis window, then [17] demonstrated by use of the Rayleigh's qoutient that the smallest possible value for Semblance is now

$$S = \frac{\lambda_M}{\sum_{i=1}^{M} \lambda_i} \,, \tag{2.31}$$

where λ_M is the smallest Eigenvalue of $\mathbf{R}(\boldsymbol{\theta})$.

The Semblance coherency measure as represented by Eq. (2.29) has the structure of a normalized conventional beamformer (which is a commonly used imaging algorithm in acoustics) [21, 24, 22]. Dispite its high robustness, conventional beamforming suffers from the diffraction-limit. This property also characterizes Semblance, which is highly robust to noise and model perturbation but has a poor resolving power in case of interfering events.

2.2.2 MUSIC

The MUSIC algorithm was first developed as an improvement to Piserenko's harmonic decompositon [25] to estimate the frequencies of a sum of complex exponentials in white noise. MUSIC utilizes the Eigendecomposition of the data covariance matrix and specifically the orthogonality between the signal and noise sub-space Eigenvectors. By utilizing the fact that a unitary steering vector $\mathbf{u}$ spans the signal sub-space of a data covariance matrix for a perfectly flat event within the anaysis window (i.e. the case when the traveltime is described by the correct parameters) then the projection of $\mathbf{u}$ into the noise sub-space results in a nill value. As a consequence the MUSIC pseudo-spectrum can be constructed as [26, 24, 22]

$$P_{MU}(\boldsymbol{\theta}) = \frac{\mathbf{u}^\dagger \mathbf{u}}{\mathbf{u}^\dagger \left[\mathbf{v}_n(\boldsymbol{\theta})\mathbf{v}_n^\dagger(\boldsymbol{\theta})\right] \mathbf{u}} , \tag{2.32}$$

here $\mathbf{v}_n(\boldsymbol{\theta})$ represents the noise sub-space Eigenvectors of $\mathbf{R}(\boldsymbol{\theta})$. The optimal parameters $\boldsymbol{\theta}$ are then obtained by locating the peak values of the MUSIC pseudo-spectrum.

To demonstrate the difference in performance between Semblance and MUSIC, a synthetic CMP gather was generated as shown in Fig. 2.12. A Ricker wavelet with a center-frequency of 20 Hz was used as a source wavelet and a two-layer model was assumed. The RMS-velocities of the shallow and slightly deeper events were respectively 3400 m/s and 3600 m/s. In the coherency computation we used an analysis window of 22 ms. To avoid the correlated signals creating a rank deficient covariance matrix and to increase the stablity of the covariance matrix estimate, we performed spatial smoothing using 34 subarrays, each consisting of 67 receivers. Figure 2.13 shows velocity analysis results obtained using both Semblance and MUSIC as a coherency measure. In both cases the two velocity parameters can be recovered, but the resolution of MUSIC is superior.

2.2.3 SB-MUSIC diffraction imaging

In order to fully extract the information contained in the diffraction-only data, we need an imaging algorithm that can handle interfering events and provide a highly-resolved image of the scatterers. First we make the observation that conventional imaging of diffractions typically consists of the following procedure:

(i) For every point in the image-domain we construct a diffraction traveltime using the optimal stacking velocity.

(ii) Within a window following the traveltime obtained from (i) we stack the diffraction-only data. The locations in the image-space with the largest stacking energy represent the diffractors location.

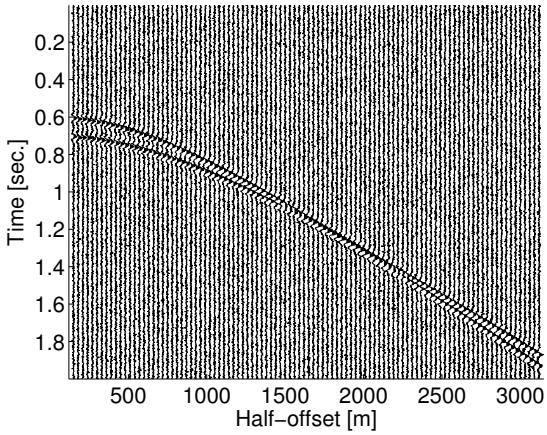

Fig. 2.12: *CMP data used to asses the performance of the coherency measures.*

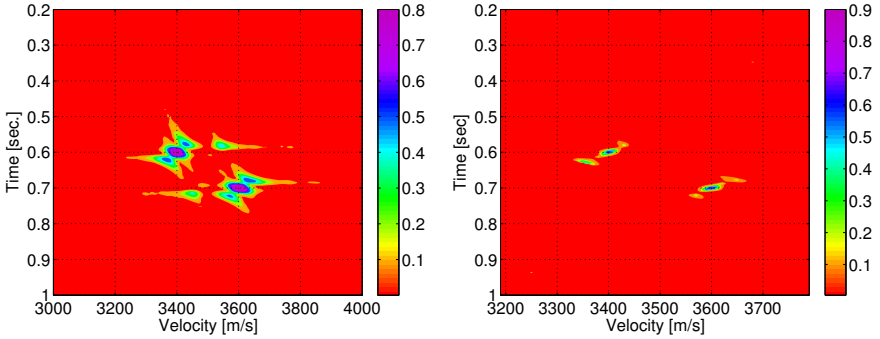

Fig. 2.13: *Velocity analysis using (a) Semblance and (b) MUSIC.*

By analogy, we propose to replace the diffraction stacking operation by MUSIC. Thus, by computing the MUSIC pseudo-spectrum at a given time sample t_0 and mid-point coordinate m_0, namely,

$$\mathbf{P}_{MU}(t_0, m_0) = \frac{\mathbf{u}\mathbf{u}^\dagger}{\mathbf{u}\mathbf{P}_n\mathbf{u}^\dagger} \,, \tag{2.33}$$

a large value will be obtained in case of a diffractor (super-resolved localization). In Eq. (2.33) $\mathbf{P}_n = \mathbf{V}_n\mathbf{V}_n^\dagger$ represents the (steered) noise sub-space projection matrix. However, unlike conventional migration (or Semblance) the MUSIC algorithm does not give constrained magnitudes of the measured coherency. Therefore, by utilizing the high-resolving nature of the MUSIC algorithm and the constrained magnitude values of Semblance, we introduced Semblance balanced MUSIC (SB-MUSIC) [16]. The main principle of SB-MUSIC is that, for every point in the MUSIC pseudo-spectrum $\mathbf{P}_{MU}(t_0, m_0)$ we define a rectangular window of size $N_T \times N_R$ around the point (t_0, m_0). We then compute the total energy of both MUSIC $E_{MU}(t_0, m_0)$ and Semblance $E_S(t_0, m_0)$ within this window and finaly weight the MUSIC pseudo-spectrum. Mathematically, this can be given as

$$\mathbf{P}_{SB-MU}(t_0, m_0) = \frac{E_S(t_0, m_0)}{E_{MU}(t_0, m_0)}\mathbf{P}_{MU}(t_0, m_0) \,, \tag{2.34}$$

where $E_{MU}(t_0, m_0)$ and $E_S(t_0, m_0)$ are defined as

$$\begin{aligned} E_S(t_0, m_0) &= \sum_{k=-N_T/2}^{N_T/2} \sum_{l=-N_R/2}^{N_R/2} \mathbf{S}(t_0 + k, m_0 + l) \\ E_{MU}(t_0, m_0) &= \sum_{k=-N_T/2}^{N_T/2} \sum_{l=-N_R/2}^{N_R/2} \mathbf{P}_{MU}(t_0 + k, m_0 + l) \,. \end{aligned} \tag{2.35}$$

SB-MUSIC has been tested both as a coherency meaure [16, 14] as well as an imaging algorithm [15]. In both cases, SB-MUSIC outperformed Semblance and conventional migration in case of interfering events.

2.3 Diffraction separation

Diffraction is a physical phenomenon that occurs when a propagating wave encounters an obstacle and the energy of the wave is redistributed in space producing constructive and destructive interference. The classical example is when light propagates through a narrow slit and generates a fringe pattern (i.e. bands of light and dark regions) at the edges of the shadow observed on the screen. Diffraction can be associated with all types of waves; however in our day to day activity we rarely notice the diffractive effects of waves (e.g. diffraction of visible light). The reason for this is that, diffraction is the result of confinement of the lateral extent of a wave, and is most appreciable when the confinement size is comparable with the wavelength of the incident wave [27] (e.g. for visible light this is within the order of hundreds of nanometers).

The history of diffraction origins from the ancient search for the true nature of light. The first person to observe diffractions experimentally was Francesco Maria Grimaldi ($1618 - 1663$)

who also introduced the term diffraction, from the Latin *diffringere* meaning to break into pieces. Christian Huygens ($1629-1695$) who proposed the wave theory of light also noticed diffractions, but was unable to explain it. The physical explanation of the cause of diffractions had to wait until Thomas Young ($1773-1829$) discovered the law of interference of light. This allowed Augustin Jean Fresnel ($1788-1827$) to realize that diffraction of light is caused by mutual interference of secondary waves generated at the aperture and the primary wavefront not obstructed by the screen [4]. Gustave Robert Kirchhoff ($1824-1887$) refined the assumptions made by Fresnel and put the whole idea on a sounder mathematical basis. Later, important extensions to the mathematical description of diffractions were made by Lord Rayleigh ($1842-1919$) and also Arnold Sommerfeld ($1868-1951$).

In this thesis we consider seismic and Ground Penetrating Radar (GPR) diffracted waves. Seismic diffractions occur when the propagating waves encounter a sudden change in the elastic properties of the medium within the scale of the wavelength. Such geologic structures include faults, fractures, pinch-outs, wedge-outs and channels. Therefore, in order to be able to image small scale discontinuities or inhomogeneities in the subsurface, we need to utilize the diffracted wavefield contributions. However, these diffracted waves are often much weaker than the specular reflections which poses difficulties on their identification and interpretation. Thus, we need to enhance the diffractions or possibly separate them from the dominating specular reflections.

In this thesis we use the kinematic differences (i.e. traveltimes) between diffractions and reflections to construct robust separation schemes. However, since these formulations are based on analytical traveltime expressions it implies a subsurface model with smooth lateral variations in the velocity. In case of more complex velocity behaviour these techniques will not work so well. This is by analogy with the basic differences between prestack time and depth migrations.

To illustrate typical differences between the traveltimes of diffractions and reflections employing different data sorting, a simple synthetic data example is considered. The model consists of a horizontal reflector and a scatterer located on top of it. This point scatterer can be either placed in the symmetry center or to the side. The case of a Common Offset (CO) gather is shown in Fig. 2.14 for an offset of 337.5 m and 1337.5 m, respectively. For both, the small and the large offset major parts of the two traveltime curves are rather different. However, a region exists where the two responses coincide. This region is denoted the *first Fresnel zone* and it can be easily observed that it grows larger with incresing offset. Thus, in order to properly discriminate between the kinematics of diffractions and reflections in the CO-domain, an aperture of at least two times the first Fresnel zone is needed.

Figure 2.15 shows the traveltime response in the CMP-domain. In case the scatterer is located vertically beneath the mid-point, the diffraction and reflection traveltimes coincide and can not be separated. If the scatterer is horizontally displaced, differences start to occur between the two events. Finally, the Common-Shot (CS) (or alternatively Common-Receiver (CR) by reciprocity) sorting is considered. Figure 2.16 shows how the two responses vary with diffractor position. In case the scatter is placed vertically below the source, only small differences exist in traveltime. By displacing the scatterer the responses become more different.

From these simple simulations we have observed that sorting in the CO-domain gives a good separation between diffractions and reflections outside the first Fresnel zone. In case of CMP and CS (or CR) sorting the discrimination is not so good unless the scatterer is displaced to the side. In the next two subsections we will briefly introduce two alternative traveltime expressions

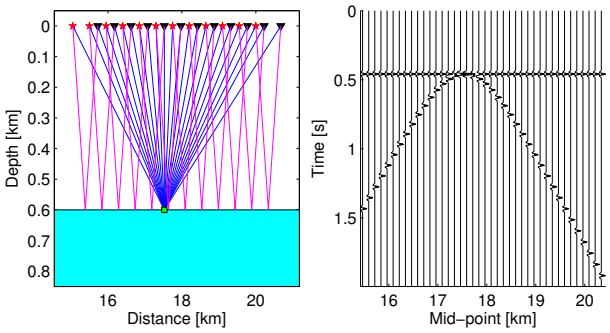

(a)

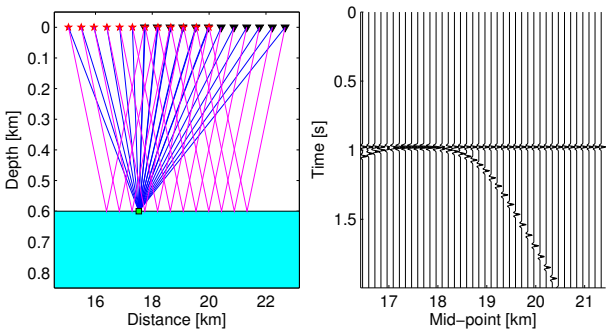

(b)

Fig. 2.14: *CO acqusition (left) and the corresponding traveltime (right) for an offset of (a)* 337.5 *m and (b)* 1337.5 *m.*

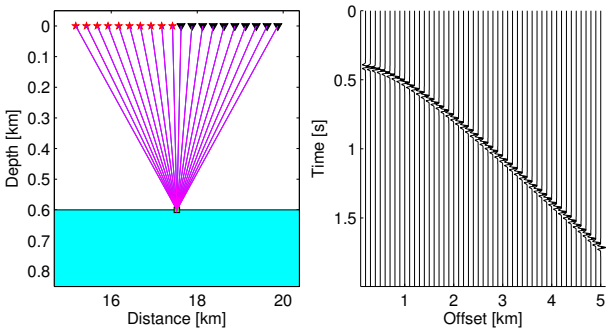

(a)

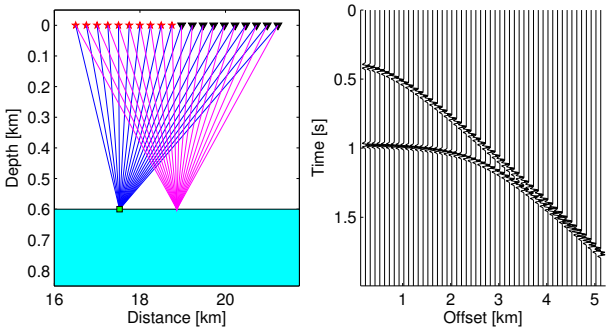

(b)

Fig. 2.15: *CMP acqusition (left) and the corresponding traveltime (right) when the diffractor is (a) beneath the mid-point and (b) when the diffractor is displaced by* 1337 *m.*

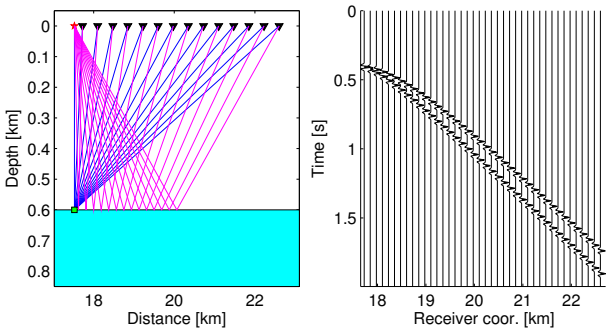

(a)

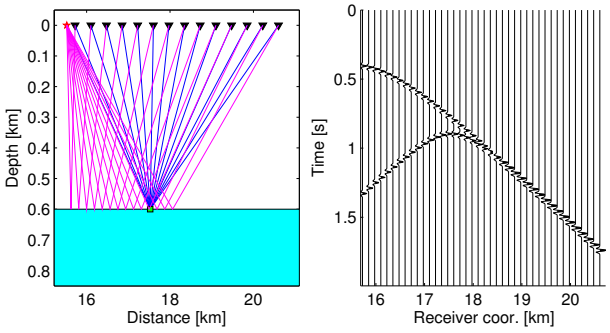

(b)

Fig. 2.16*: CS acqusition (left) and the corresponding traveltime (right) when the diffractor is (a) beneath the source location and (b) when the diffractor is displaced by* 2500 *m.*

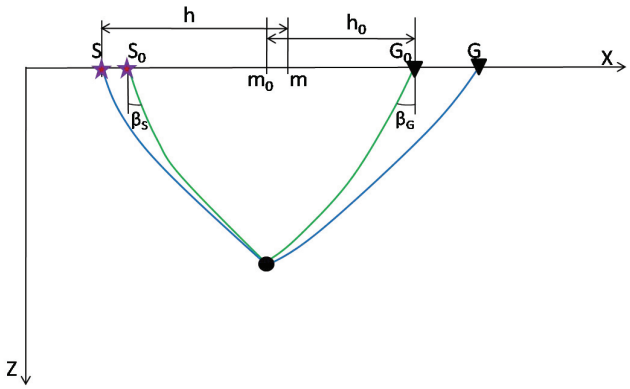

Fig. 2.17*: Ray diagram illustrating the central ray (green) and the paraxial ray (blue).*

for diffraction events. These traveltimes are on parameteric form and optimal values need to be determined for these parameters before actual separation (by analogy with velocity analysis followed by stacking). To be able to obtain optimal and highly resolved parameter values, we will employ MUSIC as a coherency measure. We will also simplify the parameteric analysis by using different data sorting. In this way we reduce the dimensionality of the parametric space. Two different data sorting will be employed; CO and CMP. A combination of these two domains give a good separation and is also supported by our simple simulations.

2.3.1 Diffraction separation based on modified CRS

The Common Reflection Surface (CRS) technique was originally developed with the purpose of enhancing the signal-to-noise ratio during stacking. In stead of using a simple CMP gather also neighbouring CMP's were included to define a stacking surface [28, 29, 30]. The traveltime expression associated with such a surface was then describing reflections. However, the case of diffractions can be thought of as the limiting case when the reflector (surface) shrinks to a point [30].

In [31, 30] a 2D hyperbolic reflection traveltime approximation for paraxial rays in the vicinity of a constant-offset central ray was developed. In this thesis we have considered the limiting case of diffractions and modified this formulation accordingly (cf. Fig. 2.17). This diffraction traveltime can be explicitly written as

$$\begin{aligned} t^2(m,h) &= \left[t_0 + \left(\frac{sin\beta_G}{V_G} - \frac{sin\beta_S}{V_S}\right)\Delta m + \left(\frac{sin\beta_G}{V_G} + \frac{sin\beta_S}{V_S}\right)\Delta h\right]^2 \\ &+ t_0\left[\left(K^G_{CMP}\frac{cos^2\beta_G}{V_G} - K^S_{CMP}\frac{cos^2\beta_S}{V_S}\right)\Delta m^2\right] \\ &+ t_0\left[\left(K^G_{CMP}\frac{cos^2\beta_G}{V_G} - K^S_{CMP}\frac{cos^2\beta_S}{V_S}\right)\Delta h^2\right] \\ &+ 2t_0\left[\left(K^G_{CMP}\frac{cos^2\beta_G}{V_G} - K^S_{CMP}\frac{cos^2\beta_S}{V_S}\right)\Delta m\Delta h\right] . \end{aligned} \tag{2.36}$$

In Eq. (2.36), t_0 denotes the traveltime along the central ray assosiated with the mid-point m_0 and

half-offset h_0, and K^S_{CMP} and K^G_{CMP} are wavefront curvatures associated with a wave originating from the point scatterer and measured arround respectively the source and receiver location of the central ray (assuming CMP geometry). The quantities Δm and Δh are defined as follows

$$\Delta m = m - m_0 \quad , \quad \Delta h = h - h_0 \, , \tag{2.37}$$

where m and h are respectively the mid-point and half-offset of the paraxial ray. Moreover, V_S and β_S are respectively the near-surface velocity and take-off angle of the central ray at its source point, with analogous definitions for the quantities V_G and β_G.

Consider now the special case of CO. The diffraction traveltime expression now reads (obtained by setting $\Delta h = 0$ in Eq. (2.36))

$$t^2_{CO}(m, h_0) = [t_0 + a_{CO}\Delta m]^2 + b_{CO}\Delta m^2 \, , \tag{2.38}$$

where

$$\begin{aligned} a_{CO} &= \frac{sin\beta_G}{V_G} - \frac{sin\beta_S}{V_S} \\ b_{CO} &= t_0 \left[K^G_{CO} \frac{cos^2\beta_G}{V_G} - K^S_{CO} \frac{cos^2\beta_S}{V_S} \right] \, . \end{aligned} \tag{2.39}$$

In order to obtain Eq. (2.39) we have also assumed that the wavefront curvatures in a CMP- and CO-geometry are the same in case of a diffraction.

The main challenge is now to assign proper bounds on a_{CO} and b_{CO} to be used in the parameter coherency analysis. Such bounds are seen to be dependent on actual four parameters in practice; β_G, β_S, K^G_{CO} and K^S_{CO}. In [15] we suggest a simplified approach where a symmetric medium case is initially assumed and later slightly perturbed to obtain optimal parameters.

2.3.2 REM based diffraction separation

The modified CRS-technique is based on a ray type approach (each of the parameters describe ray quantities). Since the underlying assumption for kinematic based separation method is that of a laterally smooth velocity medium, another approach will be to assume a locally stratigraphic earth model. For such a case, we can introduce a replacement medium described by the NMO (or RMS)-velocities and straight rays. Starting from the double-square-root equation it is shown in [15] how to derive the replacement medium analogy to the modified CRS-technique. We denote it REM (replacement medium) based diffraction separation. In case of CO-domain data the traveltime parameteric equation reads

$$t^2_{CO}(m, h_0) = [t_0 + a_{CO}\Delta m]^2 + b_{CO}\Delta m^2 \, , \tag{2.40}$$

this has exactly the same form as in the modified CRS case, but the parameters are now defined by alternative quantities

$$\begin{aligned} a_{CO} &= \frac{4\Delta m_d \gamma_{ho}}{t_0 V^2} \\ b_{CO} &= \frac{4}{V^2}\left[\gamma_{ho} - \left(\frac{a_{CO} V}{2\gamma_{ho}}\right)^2 \rho_{ho}\right] , \end{aligned} \tag{2.41}$$

here $\Delta m_d = m_0 - m_d$, with m_d being the diffractor location, V is the NMO velocity (eventually corrected for dipping reflectors using the Levin factor [32] and mapped from ZO to CO using the conventional hyperbolic equation). The constants γ_{ho} and ρ_{ho} are defined by

$$\begin{aligned} \gamma_{ho} &= 1 - \left[\frac{2h_0}{V t_0}\right]^2 \\ \rho_{ho} &= \gamma_{ho}^2 + 4\gamma_{ho} - 4 . \end{aligned} \tag{2.42}$$

Differently from the modified CRS technique, the two unknown parameters are now linked together as shown in Eq. (2.41). The actual diffraction separation procedure will involve similar steps as in case of modified CRS, but putting realistic bounds on each parameter is now an easier task. However, NMO velocities need to be known (from CMP-domain velocity analysis).

To illustrate diffraction separation using the REM apprach, 2D synthetic data was generated using a model consting of a point diffractor and a plane reflector (cf. Fig. 2.14). The data was corrupted by white Gaussian noise with a variance of 10% of the variance of the signal. Since the interval velocities of the medium were known, the RMS-velocities could then be directly computed and used as NMO-velocities. In this demonstration we selected CO data corresponding to an offset of 200 m (cf. Fig. 2.18(a)). For every constant-offset central ray traveltime t_0 and mid-point location m_0, we performed a 2D parameter search using Eq. (2.40) to obtain optimal parameters a_{CO} and b_{CO} using Semblance as a coherency measure (cf. Fig. 2.18(b)). Based on the optimal sets of parameters a_{CO} and b_{CO} and using a coherency threshold of 0.3, we finally performed stacking along the diffraction curve to obtain the CO diffraction-only stack (cf. Fig. 2.18(c)). The diffraction-only stack in Fig. 2.18(c) demostrates that the diffraction signal as well as the signal-to-noise ratio are significantly enhanced.

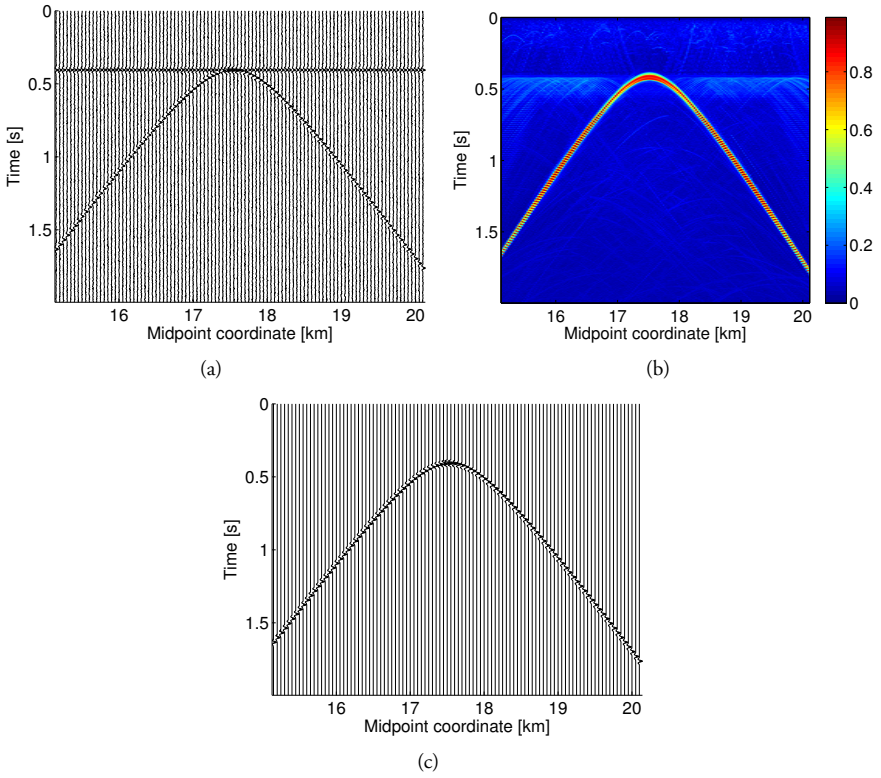

Fig. 2.18*: (a) Synthetic CO data before diffraction separation. (b) Parameter estimation based on Semblance coherency measure to find the optimal* a_{CO} *and* b_{CO}*. (C) Separated-diffraction CO data.*

Chapter 3

Summary of publications

3.1 Paper I

Leiv -J. Gelius and Endrias G. Asgedom, "Diffraction-limited imaging and beyond-the concept of super resolution," *Geophysical Prospecting*, vol. 59 no. 3, pp. 400-421, 2011.

The paper provides a framework for understanding and analyzing both diffraction-limited imaging as well as super-resolution. In this paper we have demonstrated that the backpropagated wavefield exibits an inherent odd-symmetric nature which results in a diffraction-limited focus at the scatterers as a result of superposition between diverging and converging contributions. A super-resolution imaging algorithm known as time-reversal MUltiple SIgnal Classification (MUSIC) is introduced and analyzed. In case of point-like scattering features this method has a resolving power beyond the classical limit without measuring evanescent wavefield components. The basic idea of the algorithm is to perform a singular value decomposition of the element response matrix and utilize the null sub-space singular vectors. Therefore, extreme localization of scatterers can be obtained by making use of the orthogonality between signal and noise sub-spaces. Numerical simulation using controlled data based on two strongly interacting point targets illustrated the super-resolution capabilities of time-reversal MUSIC. In addition, the effects of noise, acquisition geometry and signal frequency bandwidth on the resolving power were examined. This technique has the potential of giving high-resolution images of seismic diffractions and thus may have the potential to add more details to the big picture.

3.2 Paper II

Endrias G. Asgedom, Leiv -J. Gelius and Martin Tygel, "Higher-Resolution Determination of Zero-Offset Common-Reflection-Surface Stack Parameters," *International Journal of Geophysics*, vol. 2011, 10 pages, 2011, Article ID 819831 doi:10.1155/2011/819831.

The main focus of the paper is to obtain well resolved parameters of the 2D Zero-Offset (ZO) Common Reflection Surface (CRS) traveltime approximation. The problem the conventional Semblance coherency measure is facing, in the presence of highly interfering events (or signals), is first discussed. Next we introduced a class of higher-resolution coherency measures developed for nar-

rowband and uncorrelated signals (like radar and sonar). The MUSIC technique was specifically analyzed and modified to handle the case of seismic (wideband and correlated signals). Implementations both in time and frequency-domain were considered. Due to its simplicity, and similarity with the conventional Semblance coherency measure, we used the time-domain based MUSIC algorithm to calculate parameter estimates of the CRS traveltime. The performance of the higher-resolution MUSIC and the conventional Semblance were tested using both synthetic and field GPR data. As expected, the higher-resolution coherency measure MUSIC provided a significant improvement in the parameter estimation as compared to Semblance.

3.3 Paper III

Endrias G. Asgedom, Leiv -J. Gelius, Andreas Austeng, Sverre Holm and Martin Tygel, "Time-reversal multiple signal classification in case of noise: A phase-coherent approach," *J. Acoust. Soc. Am.*, vol. 130, no.4, pp. 2024-2034, 2011.

This paper addresses the problem of noise sensitivity of the time-reversal MUSIC algorithm. The super-resolution nature of time-reversal MUSIC has been confirmed both experimentally and computationally. However, the noise sensitivity of this algorithm has long been overseen. In this paper we modify the time-reversal MUSIC algorithm in order to be able to handle the presence of additive noise in the experiment. The basic idea of the modification includes the utilization of the wideband nature of the source pulse and the phase-coherent nature of the time-reversal operator. Therefore, we named the new algorithm phase-coherent MUSIC (PC-MUSIC). The performance of the algorithm has been tested employing synthetic multiple scattering data based on the Foldy-Lax model, as well as experimental ultrasound data acquired in a water tank. Using a limited frequency band, it was demonstrated that PC-MUSIC preserved its super-resolution property while the standard time-reversal MUSIC become severely affected and lost its super-resolution nature in case of noise.

3.4 Paper IV

Endrias G. Asgedom, Leiv -J. Gelius and Martin Tygel, "Seismic Coherency Measures in Case of Interfering Events: A Focus on the Most Promising Candidates of Higher-Resolution Algorithms," *IEEE Signal Processing Magazine*, vol. 29, no. 3, pp. 47-56, 2012.

To identify the most promising higher-resolution coherency measuring algorithm, to be applied in seismic (or GPR) signal processing, has been the main focus of this paper. It starts to discuss the conventional Semblance coherency measure and creates a link between this measure and higher-resolution algorithms like MUSIC, Eigen Vector (EV) and Minimum Variance (MV). The problem investigated was that of optimal parameter estimation in connection with diffraction separation within seismic (or GPR). The diffraction traveltime was parameterized employing an analytical equation obtained by modifying the Common Reflection Surface (CRS) traveltime for reflection. The most optimal diffraction traveltime parameters were estimated by testing different trial parameters within a selected analysis window and measuring the coherency using all the various coherency measures introduced above. The validity of each algorithm was tested employing controlled seismic

data from the Marmousi model as well as field data acquired by a ground-penetrating radar (GPR). The MUSIC algorithm was found to provide the most optimal results slightly ahead of EV and with MV falling somewhere between EV and Semblance.

3.5 Paper V

Endrias G. Asgedom, Leiv -J. Gelius, and Martin Tygel, "2D Common-Offset Traveltime Based Diffraction Enhancement and Imaging," *Geophysical Prospecting*, Submitted for publication, 2012.

This paper focuses on the problem of separating diffractions from reflections. Since diffractions often are much weaker than the specular reflections, diffraction enhancement is needed in order to obtain higher-resolution images of the subsurface. In order to be able to handle large offsets two different paraxial traveltime approximations were introduced. The first one is based on the modified CRS technique and the second represents an alternative formulation based on the replacemenet (effective) medium view and straight rays. They both have in common that the central ray is defined for a finite (non-zero) offset. The process of diffraction separation consists of two main steps; firstly the optimal diffraction traveltime parameters are determined using a proper coherency measure and secondly stacking along the diffraction traveltime surface constructed by using the most optimal parameters. Finally, after separating the diffractions using any of the two traveltime approximations, the diffractions are imaged using the higher-resolution coherency measure MUSIC. This separation scheme has been tested using controlled data taken from the Marmousi model as well as 2D seismic field data from the Jequitinhonha basin, offshore Brazil. It was demonstrated that diffractions were significantly enhanced and that a high-resolution image of the small-scale discontinuities of the subsurface could be obtained.

Chapter 4

Contributions and future work

In this section, we summarize the main contributions made in this thesis and point out possible future directions of research. The main contributions can be stated as follows

(i) Provides basic discussions and analyses of diffraction-limited imaging, supported by a rigorous mathematical description as well as numerical simulations [7].

(ii) Introduces the use of higher-resolution coherency measures in seismic as an alternative to Semblance. Most attention is paid to the MUSIC algorithm and how to modify it to be able to handle seismic signals (i.e. wideband and correlated sources) [16, 14].

(iii) Development of two diffraction separation schemes where both can be applied to offset data. The key element of both approaches is a parametric representation of the diffraction traveltimes [14, 15].

(iv) Two different high-resolution imaging techniques tailored for diffractions have been developed. The first one represents an extension of time-reversal MUSIC to make this algorithm more robust with respect to noise. Such an algorithm can be applied to seismic diffraction data as long as the input data are time-gated to fulfill sparsity [10].

The other approach is more analogue to Kirchhoff migration, where input data are limited to a small window. In classical migration data are summed along the trajectory of the window defined by the optimal velocity. Alternatively, this operation can be replaced by a MUSIC like formulation introducing the concept of a steered covariance matrix. The resolution power of this technique has been demonstrated using both GPR and seismic field data [16, 15].

Among many possible future directions, we suggest the following as the most direct continuation of this thesis.

(i) The problem of correlated signals in space and time plays a major role in higher-resolution algorithms. The standard method to solve this problem is by using spatial smoothing. However this technique reduces the resolution capabilities of the algorithms. Therefore, one possible future topic would be to intoduce random time or space-shifts to the data to reduce the correlation problem. This technique, would have the advantage of not reducing the resolution power of the algorithms.

(ii) In this thesis, both time-reversal MUSIC as well as classical MUSIC have been discussed. In some aspects the two formulations are apparently complementary since time-reversal is robust with respect to source correlation and sensitive to noise as opposed to classical MUSIC. An interesting question is then if the two techniques can be combined in a way to utilize this complementarity.

(iii) The diffraction separation schemes used in this thesis are based on hyperbolic and paraxial traveltime approximations. However, also other diffraction traveltime approximations exist for example Multi-Focusing (MF). A more extensive testing including such alternative formulations could be an interesting future research topic.

(iv) The diffraction separation and imaging techniques discussed in this thesis are time-domain based. However, it is well known that in case of large lateral velocity variations all these techniques will fail. Therefore, future diffraction separation and imaging scheme should preferably be designed in the depth-domain.

Bibliography

[1] A. J. den Dekker and A. van den Bos, "Resolution: a survey," *Journal of Optical Society of America*, vol. 14, no. 3, pp. 547–557, 1997.

[2] V. Ronchi, "Resolving power of calculated and detected images," *Journal of Optical Society of America*, vol. 51, pp. 458–460, 1960.

[3] L. Rayleigh, "Investigations in optics, with special reference to the spectroscope," *Phil. Mag. S.*, vol. 8, no. 49, pp. 261–274, 403–411, 477–486, 1879.

[4] M. Born and E. Wolf, "Principles of optics, 7^{th} edition," *Cambridge University Press*, 1999.

[5] R. G. Newton, "Scattering theory of waves and particles, 2^{nd} edition," *Dover Publications, Inc.*, 1982.

[6] C. Esmersoy and M. Oristaglio, "Revese-time wave-field extrapolation, imaging, and inversion," *Geophysics*, vol. 53, pp. 920–931, 1988.

[7] L. J. Gelius and E. G. Asgedom, "Diffraction-limited imaging and beyond - the concept of super resolution," *Geophysical Prospecting*, vol. 59, no. 3, pp. 400–421, 2011.

[8] S. K. Lehman and A. J. Devaney, "Transmission mode time-reversal super-resolution imaging," *J. Acoust. Soc. Am.*, vol. 113, pp. 2742–2753, 2003.

[9] S. Hou, K. Huang, K. Solna, and H. Zhao, "A phase and space coherent direct imaging method," *J. Acoust. Soc. Am.*, vol. 25, pp. 227–238, 2009.

[10] E. G. Asgedom, L. J. Gelius, A. Austeng, S. Holm, and M. Tygel, "Time-reversal multiple signal classification: A phase-coherent apprach," *J. Acoust. Soc. Am.*, vol. 130, no. 4, pp. 2024–2034, 2011.

[11] F. K. Gruber, E. A. Marengo, and A. J. Devaney, "Time-reversal imaging with multiple signal classification considering multiple scattering between the targets," *J. Acoust. Soc. Am.*, vol. 115, pp. 3042–3047, 2004.

[12] A. J. Devaney, "Super-resolution processing of multi-static data using time-reversal and music," *Northeastern University, Report available at http://www.ece.neu.edu/faculty/devaney/ajd/preprints.htm (date last viewed 02/10/11)*, 2000.

[13] C. Prada and J. L. Thomas, "Experimental subwavelength localization of scatterers by decomposition of the time reversal operator interpreted as a covariance matrix," *J. Acoust. Soc. Am.*, vol. 114, pp. 235–243, 2003.

[14] E. G. Asgedom, L. J. Gelius, and M. Tygel, "Seismic coherency measures in case of interfering events," *Signal Processing Magazine*, vol. 29, no. 3, pp. 47–56, 2012.

[15] ——, "2d common-offset diffraction enhancement and imaging," *Geophysical Prospecting, Submitted for publication*, 2012.

[16] ——, "Higher-resolution determination of zero-offset common-reflection-surface stack parameters," *International Journal of Geophysics*, vol. 2011, pp. 10 pages, Article ID 819 831 doi:10.1155/2011/819 831, 2011.

[17] A. Gersztenkorn and K. Marfurt, "Eigenstructure-based coherence computations as an aid to 3-d structural and stratigraphic mapping," *Geophysics*, vol. 64, no. 5, pp. 1468–1479, 1999.

[18] T. Taner and F. Koehler, "Velocity spectra - digital computer derivation and applications of velocity functions," *Geophysics*, vol. 34, pp. 859–881, 1969.

[19] N. Neidell and M. Taner, "Semblance and other coherency measures for multichannel data," *Geophysics*, vol. 36, pp. 482–497, 1971.

[20] B. Biondi and C. Kostov, "High-resolution velocity spectra using eigenstructure methods," *Geophysics*, vol. 54, pp. 832–842, 1989.

[21] W. Du and R. L. Kirlin, "Discrimination power enhancement via high resolution velocity estimators," *IEEE Acoustics, Speech, and Signal Processing*, 1993.

[22] R. L. Kirlin, "Covariance analysis for seismic signal processing," *Society of exploration geophysics*, 1999.

[23] D. H. Johnson and D. E. Dudgeon, "Array signal processing: Consepts and techniques," *Prentice Hall*, 1993.

[24] H. Krim and M. Viberg, "Two decades of array signal processing research, the parametric approach," *IEEE Signal Processing Magazine*, pp. 67–94, 1996.

[25] V. F. Pisarenko, "The retrieval of harmonics from a covariance function," *Geophysics J. Roy. Astron. soc.*, vol. 33, pp. 347–366, 1973.

[26] R. O. Schmidt, "Multiple emitter location and signal parameter estimation," *IEEE Trans. Antennas and Propagation*, vol. AP-34, pp. 276–280, 1986.

[27] J. W. Goodman, "Introduction to fourier optics, 2^{nd} edition," *McGRAW-HILL Companies, Inc.*, 1996.

[28] J. Mann, R. Jäger, T. Müller, G. Höcht, and P. Hubral, "Common-reflection-surface stack - a real data example," *J. Appl. Geoph.*, vol. 42, no. 3,4, pp. 301–318, 1999.

[29] R. Jäger, J. Mann, G. Hocht, and P. Hubral, "Common-reflection-surface stack: image and attributes," *Geophysics*, vol. 66, pp. 97–109, 2001.

[30] Y. Zhang, S. Bergler, and P. Hubral, "Common-reflection-surface (crs) stack for common offset," *Geophysical Prospecting*, vol. 61, no. 3, pp. 759–775, 2001.

[31] R. Bortfeld, "Geometrical ray theory: rays and traveltimes in seismic systems (second order approximation of the traveltimes)," *Geophysics.*, vol. 1, pp. 342–349, 1989.

[32] F. K. Levin, "Apparent velocity from dipping interface reflections," *Geophysics*, vol. 36, no. 3, pp. 510–516, 1971.

Chapter 5

"Diffraction-limited imaging and beyond-the concept of super resolution," Leiv -J. Gelius and Endrias G. Asgedom, *Geophysical Prospecting*, vol. 59 no. 3, pp. 400-421, 2011.

Chapter 6

"Higher-Resolution Determination of Zero-Offset Common-Reflection-Surface Stack Parameters," Endrias G. Asgedom, Leiv -J. Gelius and Martin Tygel, *International Journal of Geophysics*, vol. 2011, 10 pages, 2011, Article ID 819831 doi:10.1155/2011/819831.

Hindawi Publishing Corporation
International Journal of Geophysics
Volume 2011, Article ID 819831, 10 pages
doi:10.1155/2011/819831

Research Article

Higher-Resolution Determination of Zero-Offset Common-Reflection-Surface Stack Parameters

Endrias G. Asgedom,[1,2] Leiv J. Gelius,[1,2] and Martin Tygel[3]

[1] *Department of Geosciences, University of Oslo, 0316 Oslo, Norway*
[2] *Department of Informatics, Centre for Imaging, University of Oslo, 0316 Oslo, Norway*
[3] *Department of Applied Mathematics, State University of Campinas, Campinas 1083-859 SP, Brazil*

Correspondence should be addressed to Leiv J. Gelius, l.j.gelius@geo.uio.no

Received 14 January 2011; Accepted 26 April 2011

Academic Editor: Sergey Fomel

We developed a higher resolution method for the estimation of the three travel-time parameters that are used in the 2D zero-offset, Common-Reflection-Surface stack method. The underlying principle in this method is to replace the coherency measure performed using semblance with that of MUSIC (multiple signal classification) pseudospectrum that utilizes the *eigenstructure* of the data covariance matrix. The performance of the two parameter estimation techniques (i.e., semblance and MUSIC) was investigated using both synthetic seismic diffraction and reflection data corrupted with white Gaussian noise, as well as a multioffset ground penetrating radar (GPR) field data set. The estimated parameters employing MUSIC were shown to be superior of those from semblance.

1. Introduction

Many important tasks in seismic processing and imaging require the estimation of travel-time parameters. Such parameters include, among others, *velocities* (e.g., for stacking and time-migration purposes), travel-time slopes and curvatures (e.g., for slant, common-reflection-surface (CRS), multifocus (MF) stacks) and event picking for tomographical methods. As shared with many other areas of activity, a basic feature of seismic signals (referred to as *events*) is that they exhibit some sort of *coherent* or *aligned* energy. More specifically, seismic events (e.g., reflections or diffractions) align themselves along curves or surfaces (referred to as *moveouts*) within the data. The basic strategy for signal detection and information extraction is to express these moveouts as a function of a few, meaningful parameters and to estimate such parameters so as the moveout optimally approximates the events. In general, the search for parameters, sometimes referred to as *wavefront shaping parameters*, carry key information about the geological structure under investigation.

To assess how well a moveout, defined by some trial parameters, approximates a target signal, a number of quantifiers (or *coherence measures*) has been proposed. General discussions on coherency measures applied to seismic data can be found in the pioneering papers of [1–3] with a clear emphasis on the second-order coherence measure *semblance*. Semblance quantifies the likelihood between the trial moveout and the target event by stacking the data along that moveout and measuring the energy of the output.

Adopting the notation as in [4], for a given sample, k, at a given (reference) trace, the so-called *semblance coefficient*, or simply *semblance*, S_c, can be mathematically written in the form

$$S_c = \frac{\sum_{j=k-N/2}^{j=k+N/2} \left| \sum_{i=1}^{M} x(j,i) \right|^2}{M \sum_{j=k-N/2}^{j=k+N/2} \sum_{i=1}^{M} |x(j,i)|^2}. \tag{1}$$

Here, the semblance coefficient is computed for N samples taken from M traces in a window centered about the trajectory defined by the moveout equation generated by the

trial travel-time parameters (cf. Figure 1). In the following, the given sample, k, and reference trace, as well as the number of samples, N, and number of traces, M, will be fixed throughout. As a consequence, we do not need to incorporate them into the semblance notation, which will be simply written as S_c. To construct the window in Figure 1, proper interpolation is performed to select the appropriate samples. In the language of electrical engineers, the above-described windowing process *steers* the stacking along the trial moveout.

Semblance can be described in terms of the covariance matrix of the data. Following, for example, [5], within the selected time window along the chosen trial moveout, semblance can be written in the form

$$S_c = \frac{\mathbf{u}^T \mathbf{R} \mathbf{u}}{M \operatorname{tr}(\mathbf{R})}, \tag{2}$$

where $\mathbf{u}$ is a column vector of ones, which can be referred to as the *unitary steering* vector, and $\mathbf{R}$ is the covariance of the data. Assuming that the different sources can be described by a zero-mean stochastic process, the data covariance matrix is given as

$$\mathbf{R} = E\left\{\mathbf{D}\mathbf{D}^H\right\}, \tag{3}$$

where $\mathbf{D} = (d_{ij})$ is the data matrix, in which d_{ij} is the recorded data at the ith trace and jth sample. As in usual notation, $E\{\}$ and tr() represent the expected value and matrix trace, respectively. Moreover, superscripts T and H represent transpose and conjugate transpose, respectively. As pointed out by [2], Equation (2) provides the interpretation that semblance can be regarded, within the selected time window, as a normalized output/input energy ratio. The denominator, tr($\mathbf{R}$), is the normalization used by semblance in order to generate a maximum peak of unity at the "correct" moveout parameters (namely, the ones for which we have the optimal stack).

Even though semblance is a good measure of coherency, it can in many times provide insufficient resolution for the parameter estimation. That is the case, in particular, for interfering events. There is, thus, a motivation to look for alternatives to overcome these difficulties. Attempts have been made to further improve semblance by using only those parts of the data with higher resolving power [6] and also by introducing weights in the standard semblance formulation [7]. Statistical approaches have also been introduced to increase the resolution of the velocity analysis [8]. In this paper, an alternative to semblance-like techniques will be investigated.

As recognized in sonar and radar applications, methods exploiting the properties of the eigenstructure (namely, eigenvalues and eigenvectors) of the data covariance matrix can lead to far better resolution results than semblance [4, 9, 10]. The basic idea of the eigenstructure approach is to decompose the data covariance matrix into two orthogonal subspaces. The first is the *signal* subspace, which is generated by the eigenvectors associated to high eigenvalues. The second is the *noise* subspace, generated by the small or zero eigenvalues. In this paper, we use the eigenstructure method called *multiple signal classification (MUSIC)*, introduced by [9]. MUSIC exploits the fact that the "correct" moveout, represented as a steering vector, must lie in the signal subspace and, therefore, is orthogonal to the noise subspace eigenvectors. As a consequence, the *projection* of the steering vector onto the noise subspace provides a nearly vanishing value. The inverse of such a projection (namely, the sum of the dot products of the steering vector with the noise eigenvectors) should peak when the steering vector represents a correct moveout.

This work can be seen as a followup of [10], in which the application of MUSIC to single-parameter velocity analysis and slant stacks is described. Here, we extend the application of MUSIC to common-reflection-surface (CRS) multi-parameter estimation. Besides the theoretical exposition of the technique, applications to first synthetic examples, consisting of dipping planar reflectors and point diffractors, are provided. Comparisons of the obtained results and conventional semblance confirm, at least for these initial examples, the expected far better resolution of MUSIC. To further support this conclusion a real multioffset GPR data set was also analysed. It was demonstrated that MUSIC, unlike semblance, was able to better resolve interfering events.

2. Classical Music: Narrowband and Uncorrelated Signals

In its original or classical form [9], MUSIC considers an array of N_r receivers recording W incoming reflected or diffracted signals, in an arbitrary background medium. In time domain, the data recorded by the ith receiver can be modeled as

$$d_i(t) = \sum_{w=1}^{W} s_w\left(t - \tau_{i,w}^{\theta}\right) + n_i(t), \quad (i = 1, 2, \ldots, N_r), \tag{4}$$

where $s_w(t)$ is the source pulse associated with event w, and $n_i(t)$ is the additive random noise at the ith receiver. Finally, $\tau_{i,w}^{\theta}$ is the travel-time (or time delay) of the wth incoming signal (or event) arriving at the ith receiver. The superscript, θ, indicates that the moveouts depend on a set of one or more parameters, here denoted, by a so-called *parameter vector*, $\boldsymbol{\theta}$. The most popular trial-moveout example is the normal-moveout (NMO), applied for velocity analysis in the common-midpoint (CMP) configuration. In the 2D situation, the single parameter to be estimated is the NMO-velocity. An example of multiparameter moveout is the general hyperbolic moveout used by the common-reflection-surface (CRS) stacking method. As previously indicated, application of MUSIC to velocity analysis has been described by [10]. Here, we extend the analysis to CRS parameter estimation in 2D data. In this situation, three parameters are to be estimated. In order not to disturb the main flow, the description of the generalized hyperbolic or, more simply, the CRS travel-times, $\tau_{i,w}$, is postponed to the appendix.

2.1. Narrowband Signals. For narrowband signals $s_w(t)$, the travel-times can be expressed as exponential phase shifts

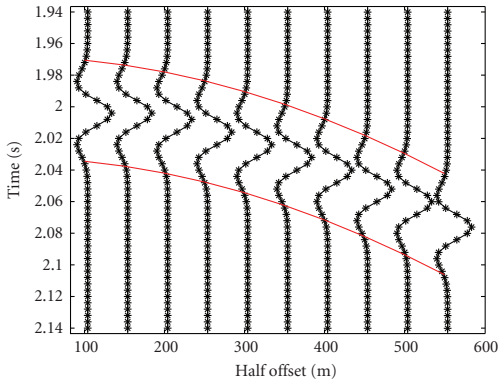

FIGURE 1: Time window used to compute semblance. The two red lines show the travel-time trajectories bounding the window used to select the data.

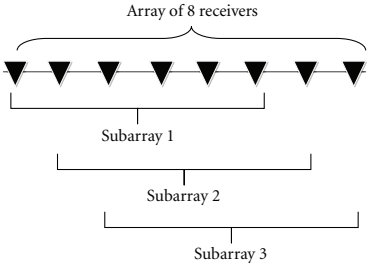

FIGURE 2: Concept of spatial smoothing.

around the center angular frequency ω. For notation simplicity, that fixed frequency will be omitted. As a consequence, the data model in (4) can be recast as

$$d_i(t) = \sum_{w=1}^{W} s_w(t) \exp\left(-i\omega\tau_{i,w}^{\theta}\right) + n_i(t). \tag{5}$$

After time discretization, the above equation can be recast in matrix form as

$$\mathbf{D} = \mathbf{A}(\boldsymbol{\theta})\mathbf{S} + \mathbf{N}, \tag{6}$$

where $\mathbf{D} = (d_{ij}) = (d_i(t_j))$ and $\mathbf{N} = (n_{ij}) = (n_i(t_j))$ are, respectively, the $N_r \times N_t$ *data* and *additive noise* matrices, and $\mathbf{S} = (s_{wj}) = (s_w(t_j))$ is the $W \times N_t$ *source* matrix. Finally,

$$\mathbf{A}(\boldsymbol{\theta}) = (\mathbf{a}_1(\boldsymbol{\theta}), \ldots, \mathbf{a}_w(\boldsymbol{\theta}), \ldots, \mathbf{a}_W(\boldsymbol{\theta})) \tag{7}$$

is the $N_r \times W$ *array response matrix* containing all the *steering vectors*

$$\mathbf{a}_w(\boldsymbol{\theta}) = \begin{bmatrix} \exp\left(-i\omega\tau_{1,w}^{\theta}\right) \\ \exp\left(-i\omega\tau_{2,w}^{\theta}\right) \\ \vdots \\ \exp\left(-i\omega\tau_{N_r,w}^{\theta}\right) \end{bmatrix}. \tag{8}$$

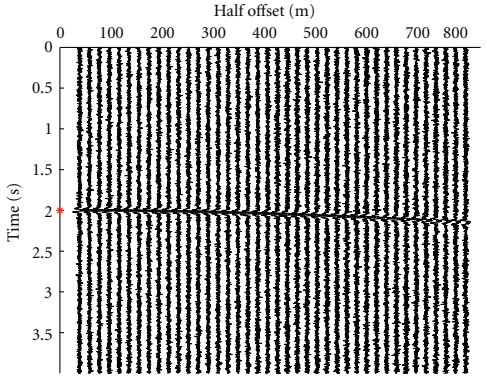

FIGURE 3: Synthetic CMP data used for comparison of MUSIC with semblance. A point diffractor and a dipping reflector ($\beta = 20^0$) with the same $\tau_0 = 2$ sec is used to generate the data. Note that the two events are very close to each other and it is difficult to distinguish them.

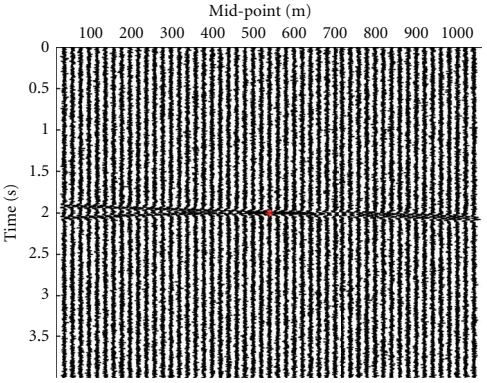

FIGURE 4: Synthetic ZO section used for comparison of MUSIC with semblance. A point diffractor and a dipping reflector ($\beta = 20^0$) is used to generate the data. The red dot ($x_0 = 540$ m and $\tau_0 = 2$ sec) shows the location where we performed the parameter search.

MUSIC utilizes the eigenstructure of the data covariance matrix defined by (3). Substituting (6) into (3) and assuming uncorrelated noise with variance of σ_n^2, the covariance matrix can be recast as

$$\begin{aligned} \mathbf{R} &= \mathbf{A}(\boldsymbol{\theta})\left[E\left\{\mathbf{S}\mathbf{S}^H\right\}\right]\mathbf{A}(\boldsymbol{\theta})^H + E\left\{\mathbf{N}\mathbf{N}^H\right\} \\ &= \mathbf{A}(\boldsymbol{\theta})\mathbf{R}_s\mathbf{A}(\boldsymbol{\theta})^H + \sigma_n^2\mathbf{I}, \end{aligned} \tag{9}$$

where $\mathbf{R}_s$ and $\mathbf{I}$ are, respectively, the source covariance and identity matrices. The MUSIC algorithm performs an eigendecomposition of this covariance matrix

$$\mathbf{R}\mathbf{U} = \boldsymbol{\Lambda}\mathbf{U}, \tag{10}$$

where $\boldsymbol{\Lambda} = \text{diag}(\lambda_1, \lambda_2, \ldots, \lambda_{N_r})$ contains the eigenvalues satisfying $\lambda_1 \geq \lambda_2 \geq \cdots \geq \lambda_{N_r}$, and $\mathbf{U} = [\mathbf{u}_1, \mathbf{u}_2, \ldots, \mathbf{u}_{N_r}]$

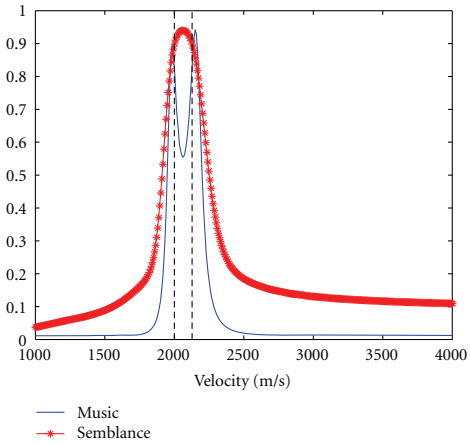

Figure 5: Spectrum of parameter C using both MUSIC and semblance (point diffractor and a dipping reflector $\beta = 20^0$). The black dotted lines show the correct location of the parameters C_{diff} and C_{dip}. We see that only MUSIC was able to resolve the two parameters.

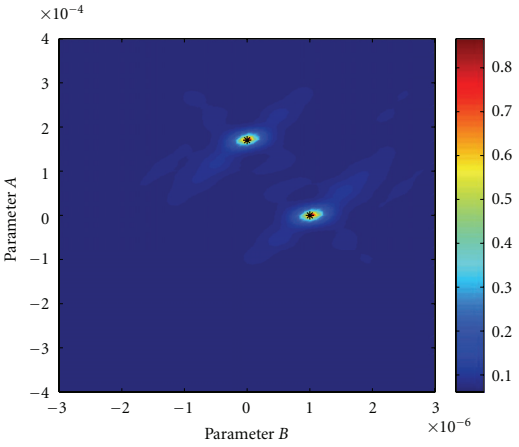

Figure 6: Uncorrelated sources: Determination of parameters A and B based on MUSIC for a diffractor and a dipping reflector $\beta = 20^0$. The black stars show the correct parameter locations.

is the matrix that consists of the corresponding (column) orthonormal eigenvectors of $\mathbf{R}$. The unitary matrix of eigenvectors $\mathbf{U}$ can be decomposed further as $\mathbf{U} = [\mathbf{U}_s\ \mathbf{U}_n]$, where the columns of $\mathbf{U}_s$ comprise the eigenvectors corresponding to the largest eigenvalues of $\mathbf{R}$ (the signal subspace), and with $\mathbf{U}_n$ containing the remaining (noise) eigenvectors.

2.2. Uncorrelated Signals. For MUSIC to be applicable in our parameter search problem, the different source pulses, $s_w(t)$, should be uncorrelated resulting in a covariance matrix

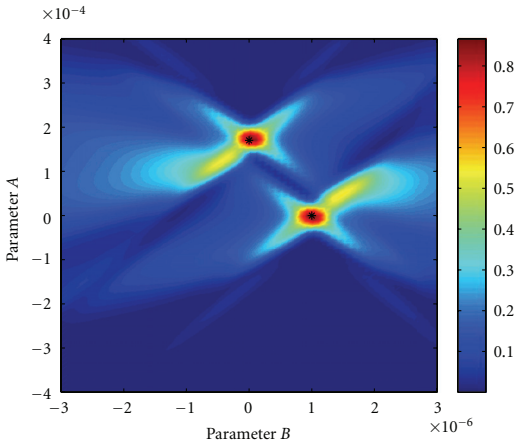

Figure 7: Uncorrelated sources: Determination of parameters A and B based on semblance for a diffractor and a dipping reflector $\beta = 20^0$. The black stars show the correct parameter locations.

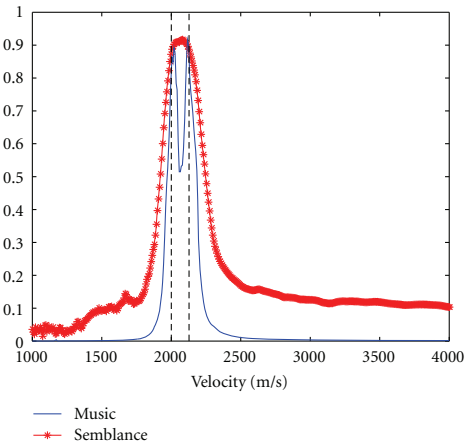

Figure 8: Parameter C determined using both MUSIC and semblance (point diffractor and a dipping reflector $\beta = 20^0$). The black dotted lines show the correct parameter locations.

$\mathbf{R}_s$ having full rank equal to the number of events W recorded at the receivers. If the M source vectors are linearly independent, then the matrix $\mathbf{R}_s$ is positive definite which results in $\mathbf{A}(\boldsymbol{\theta})\mathbf{R}_s\mathbf{A}(\boldsymbol{\theta})^H$ to be a positive semidefinite matrix with its rank spanning the steering vectors corresponding to the appropriate parameters we are searching. With the above condition satisfied and since the noise subspace is orthogonal to the signal subspace, the MUSIC *pseudospectrum*, $\mathbf{P}_{\text{MU}}(\boldsymbol{\theta})$, is given by

$$\mathbf{P}_{\text{MU}}(\boldsymbol{\theta}) = \frac{\mathbf{a}(\boldsymbol{\theta})\mathbf{a}(\boldsymbol{\theta})^H}{\mathbf{a}(\boldsymbol{\theta})\mathbf{P}_n\mathbf{a}(\boldsymbol{\theta})^H}, \tag{11}$$

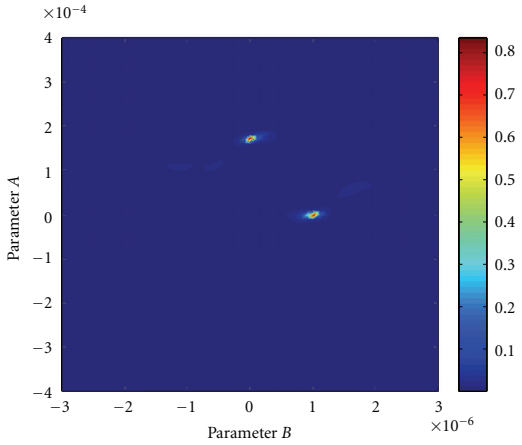

Figure 9: Correlated sources: Determination of parameters A and B based on MUSIC for a diffractor and a dipping reflector $\beta = 20^0$. The black stars show the correct parameter locations.

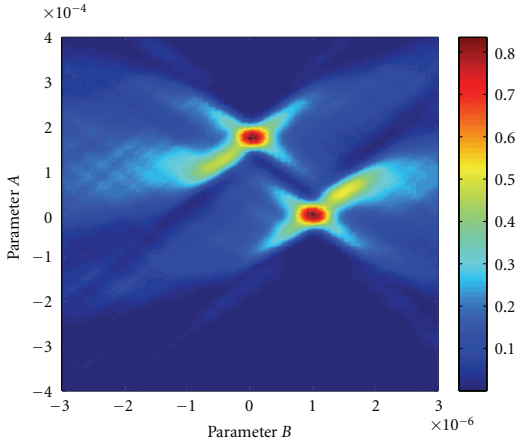

Figure 10: Correlated sources: Determination of parameters A and B based on semblance for a diffractor and a dipping reflector $\beta = 20^0$. The black stars show the correct parameter locations.

where $\mathbf{a}(\boldsymbol{\theta})$ is the test steering vector and $\mathbf{P}_n$ is the noise subspace projection matrix given by $\mathbf{P}_n = \mathbf{U}_n\mathbf{U}_n^H$. Since the steering vectors $\mathbf{a}(\boldsymbol{\theta})$ are orthogonal to the eigenvectors spanning the noise subspace $\mathbf{u}_n$, it follows that the parameter estimates will occur at those parameter values for which we have

$$\mathbf{a}(\boldsymbol{\theta})\mathbf{P}_n\mathbf{a}(\boldsymbol{\theta})^H \approx 0. \tag{12}$$

This corresponds to large peaks in the MUSIC pseudospectrum as given by (11).

2.3. Wideband Uncorrelated Signals. As indicated above, the MUSIC algorithm was originally developed for narrowband and uncorrelated signal applications. If the condition of uncorrelated signals is maintained, an alternative to this situation is to decompose a wideband data into narrowband data components and then treat each narrowband separately [10]. The MUSIC pseudospectrum at the center angular frequency ω_i of the ith narrowband now takes the form

$$\mathbf{P}_{MU}(\boldsymbol{\theta};\omega_i) = \frac{\mathbf{a}(\boldsymbol{\theta};\omega_i)\mathbf{a}(\boldsymbol{\theta};\omega_i)^H}{\mathbf{a}(\boldsymbol{\theta};\omega_i)\mathbf{P}_n(\omega_i)\mathbf{a}(\boldsymbol{\theta};\omega_i)^H}, \tag{13}$$

where $\mathbf{a}(\boldsymbol{\theta};\omega_i)$ and $\mathbf{P}_n(\omega_i)$ are respectively the test steering vector and the noise subspace projection matrix at the ith center angular frequency ω_i. The strategy followed in this work is to Fourier transform the test data and select a narrowband close to the center frequency of the source pulse as input to MUSIC.

3. Seismic Music: Wideband and Correlated Signals

Seismic signals are highly correlated and require a special modification to be used by the original MUSIC algorithm. The consequence of having correlated sources is that there will be a rank deficiency in the source covariance matrix $\mathbf{R}_s$ that will result in a mix of signal and noise subspaces. As a result, the MUSIC algorithm will loose its power to peak at the "right" parameters.

In order to handle correlated sources, spatial smoothing over the covariance matrix, can be employed [10]. The idea is to subdivide the array of N_r sensors into K identical overlapping subarrays of $N_r - K + 1$ receivers (cf. Figure 2) and then compute the covariance for all the subarrays and average the result. If the covariance matrix for subarray k is $\mathbf{R}_k$, the spatially smoothed covariance is given by

$$\mathbf{R}_K = \frac{1}{K}\sum_{k=1}^{K}\mathbf{R}_k. \tag{14}$$

To be able to implement spatial smoothing within seismics, one has to taper the data within a window following the event(s) (cf. Figure 1). The purpose of this tapering is to make the delay times of the event linear (which is the basic requirement behind spatial smoothing) [10].

The other advantage of performing the analysis in a given window is to make the steering vectors, required for generating the MUSIC pseudospectrum, to be frequency independent. This allows us to handle wideband seismic data. This process of windowing the event can also be interpreted as steering of the correlation matrix before eigendecomposition and using unity steering vectors for generating the MUSIC pseudospectrum [4].

Ideally, when the window is "perfectly" matching the event, which will be the case of an optimal choice of the moveout parameters, the signal would be flattened and all traces will nearly have the same moveout. As a consequence, the steering vectors used in (11) will be simply replaced by a vector of ones making them frequency independent. In

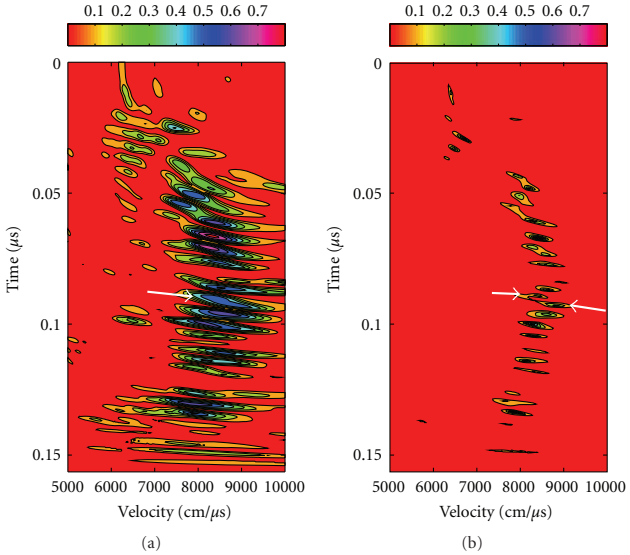

Figure 11: Velocity spectra obtained employing, respectively, semblance (a) and SB-MUSIC (b). The white arrows indicate the apparent single event associated with semblance and the corresponding two events computed from SB-MUSIC.

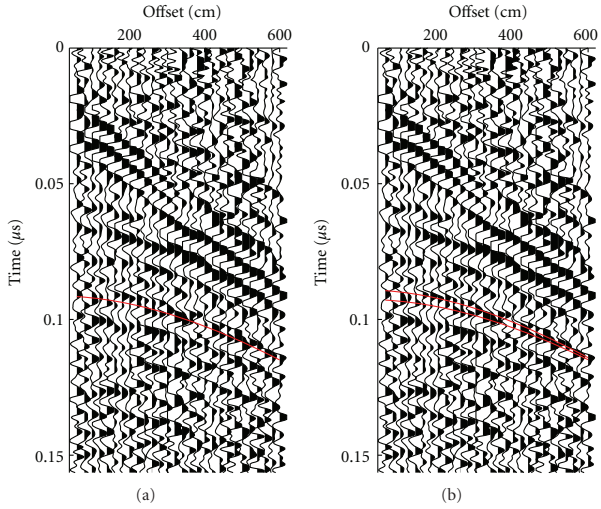

Figure 12: CMP gather superimposed the hyperbolic moveouts (red curves) for the interfering events based on semblance (a) and SB-MUSIC (b).

this situation, the MUSIC pseudospectrum generates a peak resulting in the identification of the optimal estimates of the parameters.

In practice, the windows are constructed by moveouts, defined by trial parameters. Peaking of the corresponding MUSIC pseudospectra identifies, thus, the "correct" parameters. Following this approach, [4] has shown that MUSIC can be applied for the single-parameter case of velocity analysis. The objective was, thus, to obtain a high-resolution velocity spectrum. In this work, we extend that strategy to the CRS

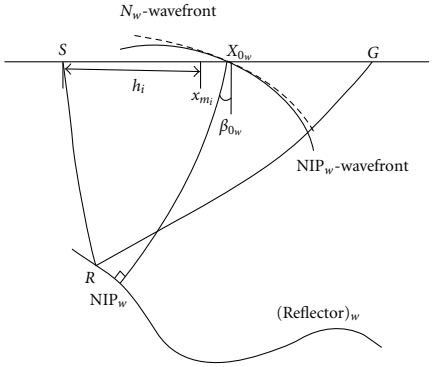

FIGURE 13: CRS parameters for a given source-receiver pair around a central ray at x_{0_w}.

multi-parameter estimating problem. In other words, our objective is to obtain high-resolution estimates of the CRS parameters, which are three in the present 2D situation.

4. Numerical Examples

In this section, we compare MUSIC and semblance for travel-time parameter estimation in the situations of classical MUSIC (narrowband uncorrelated signals) and seismic MUSIC (wideband correlated signals). For a simple model of a point diffractor and a dipping reflector with a homogeneous overburden, we analyzed the cases: (a) CMP configuration, which requires the determination of a single parameter, C of CRS travel-time (cf. (A.1)) and (b) ZO configuration, which requires the determination of two parameters, namely, parameters A and B of the CRS travel-time (cf. (A.1)). The two events (diffraction and reflection) were chosen to be almost undistinguishable. All the test parameter points with RMS velocities within [1000 : 4000] m/s (step size 7.5 m/s) were tested for parameter C and points within $[-4\times10^{-4} : 4\times10^{-4}]$ (step size 1×10^{-5}) for parameter A and points within $[-3\times10^{-6} : 3\times10^{-6}]$ (step size 1×10^{-7}) for parameter B. As seen below, in all situations, MUSIC performed much better then semblance.

4.1. Classical Music. To illustrate the application of MUSIC for narrowband uncorrelated signals, we considered a point diffractor and a dipping reflector illuminated under a CMP configuration. For a given CMP gather, the data consists of (compare with (5))

$$d_i(t) = s_{\text{diff}}(t)\exp(-i\omega\tau_{\text{diff}}) + s_{\text{dip}}(t)\exp\left(-i\omega\tau_{\text{dip}}\right) + n_i(t), \tag{15}$$

where s_{diff} and s_{dip} are the sources and τ_{diff} and τ_{dip} are the travel-times for the diffractor and dipping reflector events, respectively. Moreover, $n_i(t)$ is the additive noise. The travel-times for these two events are described by the ordinary NMO equations

$$\tau^2_{\text{diff}}(h) = \tau_0^2 + C_{\text{diff}}h^2, \qquad \tau^2_{\text{dip}}(h) = \tau_0^2 + C_{\text{dip}}h^2, \tag{16}$$

where the velocity coefficients for the diffractor, C_{diff}, and dipping reflector, C_{dip}, are given by

$$C_{\text{diff}} = \frac{4}{v^2_{\text{RMS}}}, \qquad C_{\text{dip}} = \frac{4\cos^2\beta}{v^2_{\text{RMS}}}. \tag{17}$$

Here, v_{RMS} and β represent the root mean square (RMS) velocity and the dip angle, respectively.

The sources, $s_{\text{diff}}(t)$ and $s_{\text{dip}}(t)$ are produced by a single narrowband source, $s(t)$, modified by two realizations of a random phase perturbation, $\phi_{\text{diff}}(\omega)$ and $\phi_{\text{dip}}(\omega)$, so as to produce uncorrelated sources. In frequency domain, this process is generally described as

$$\begin{aligned} s_{\text{diff}}(\omega) &= s(\omega)\exp\left[i\phi_{\text{diff}}(\omega)\right], \\ s_{\text{dip}}(\omega) &= s(\omega)\exp\left[i\phi_{\text{dip}}(\omega)\right]. \end{aligned} \tag{18}$$

A synthetic CMP gather was generated employing (15), (16), and (18) together with a Ricker zero-phase wavelet with a center frequency of 20 Hz (cf. Figure 3). The fold was 40 representing a half-offset range from 40 m to 820 m. The data was sampled with 2 ms and white Gaussian noise with a variance of 10% of the maximum trace amplitude was added. The parameter estimation process was benchmarked using the classical semblance analysis of [2].

The output from MUSIC (cf. (13)) is shown in Figure 5 together with the result obtained using semblance. For both cases we used, a window size of 11 samples and in addition for MUSIC we considered two signal subspaces and the rest as noise subspaces. As a result, MUSIC is seen to outperform semblance and resolve the two parameters well. It is well known that the values output from MUSIC are arbitrary. To avoid this phenomenon, we have introduced a *semblance balancing*. This technique is discussed in detail in connection with the real-data example presented below.

To perform a two-parameter test, we have now simulated a zero-offset (ZO) section for the same previous point diffractor and dipping reflector (cf. Figure 4). The corresponding two ZO travel-times for diffraction and reflection are now given by

$$\begin{aligned} \left[\tau_{\text{diff}}(x_m)\right]^2 &= \tau_0^2 + B_{\text{diff}}(x_m - x_0)^2, \\ \left[\tau_{\text{dip}}(x_m)\right]^2 &= \tau_0 + A_{\text{dip}}[(x_m - x_0)]^2, \end{aligned} \tag{19}$$

with $B_{\text{diff}} = C_{\text{diff}}$ and $A_{\text{dip}} = 1.71\times10^{-4}$ (corresponding to a dip of 20^0 and a homogeneous medium with constant velocity 2000 m/s). As seen from the Appendix, the above equations represent the generalized hyperbolic (CRS) travel-time of equation (A.1), in which the conditions

$$B_{\text{diff}} = C_{\text{diff}}, \qquad B_{\text{dip}} = 0, \tag{20}$$

have been implemented. As indicated in the Appendix, the far-left equation above represents the diffraction condition. The far-right equation is due to the fact that in this considered experiment, the N-wave is planar.

Based on (19), using the previous uncorrelated sources (18), synthetic ZO data were computed for midpoints between 40 m and 1040 m. The results from the two-parameter search (A and B) are shown for, respectively, MUSIC (cf. Figure 6) and semblance (cf. Figure 7). MUSIC gives well-resolved results, as opposed to the semblance, where the estimated parameters are more inaccurate.

4.2. Seismic Music. To examine the performance of MUSIC compared to semblance in case of wideband correlated signals, we generated synthetic data based on the travel-time (16) for a CMP gather and (19) for a ZO section. The parameter search was performed within a time window of 25 time samples with the ZO travel-time being the middle sample and following a hyperbolic delay trajectory defined by the travel-times. For the computation of the MUSIC pseudospectrum, the samples within the hyperbolic window were used to form the data covariance matrix and the associated eigendecomposition. In order to reduce the correlated source effect we performed spatial smoothing of the covariance matrix using 31 subarrays each consisting of 10 receivers for the CMP data and 37 subarrays each consisting of 15 receivers for the ZO data.

The results of the parameter search is shown in Figure 8 for the CMP data (i.e., determination of parameter C) and Figures 9 and 10 for the ZO section (i.e., determination of parameters A and B). It is apparent that both semblance and MUSIC can resolve parameters A and B, but MUSIC shows a higher resolution in general. Moreover, for parameter C only MUSIC is able to resolve the two events.

4.3. Real Data Example Using GPR Data. The first step of the CRS analysis determining the C parameter can be regarded as a CMP-based velocity analysis. As indicated by our previous synthetic data example, MUSIC was seen to have a better potential than semblance for resolving interfering events (cf. Figures 5 and 8). We will now investigate whether that feature is confirmed in real data. Prior to our analysis, however, the following normalization issue has to be considered. As opposed to semblance, which produces normalized values between 0 and 1, MUSIC, despite its high-resolution capability, yields arbitrary amplitude values. Such behavior makes the simple replacement of semblance with MUSIC as a coherency measure, for example, in standard velocity analysis, not adequate.

In order to condition MUSIC to be a normalized quantity, we introduce a scaled version of it, denoted by *semblance-balanced* MUSIC or, more simply, SB-MUSIC. In the framework of velocity analysis, SB-MUSIC is defined as follows: for a given CMP location, as well as a selection of N zero-offset time samples, t_i and M trial stacking velocities, V_j, we let m_{ij} and s_{ij} represent the coherency values obtained from MUSIC and semblance, respectively. In other words, (m_{ij}) and (s_{ij}) represent $N \times M$ velocity spectra associated with MUSIC and semblance coherency measures. Denoted by $\hat{m}_{ij}$, SB-MUSIC is given by

$$\hat{m}_{ij} = \frac{A_{s,i}}{A_{m,i}} m_{ij}, \tag{21}$$

where

$$A_{s,i} = \sqrt{\sum_{k=1}^{M} s_{ik}^2}, \qquad A_{m,i} = \sqrt{\sum_{k=1}^{M} m_{ik}^2}. \tag{22}$$

Application of the above conditioning makes sure that those amplitude anomalies inherent to the original MUSIC velocity spectrum are *balanced* according to the energy level of semblance.

A real multioffset GPR data set was used to test out the feasibility of this approach. For an in depth description and discussion of these data, the readers are referred to [11]. Figure 11 shows an example of a typical velocity spectrum obtained from the GPR data using both semblance and SB-MUSIC. In these computations, we used a window size of eleven samples for both semblance and MUSIC. In addition, we performed spatial smoothing of subarray size 15 from a fold of 28 to ensure that MUSIC handles the correlated GPR signals properly. Figure 11 clearly demonstrates that interfering events are much better resolved in the SB-MUSIC spectrum (Figure 11(b)) than in its corresponding semblance spectrum (Figure 11(a)). In particular, as indicated by white arrows, it can be seen how two interfering events are unresolved by semblance (Figure 11(a)) and well resolved by SB-MUSIC (Figure 11(b)). To further validate the previous observation, the hyperbolic moveout curves corresponding to those two events were superimposed to the corresponding CMP-gather (cf. Figure 12(b)). These curves seem to correlate well with two interfering events. As a reference, the result obtained using semblance is also included (cf. Figure 12(a)). It can be regarded as a fit based on a mix between the two interfering events.

5. Conclusions

In this paper, we discussed the CRS travel-time parameters estimation problem in seismic signal processing. The conventional semblance algorithm was found to generate lower-resolution estimates of the parameters. For the purpose of obtaining higher-resolution parameter estimates, we replaced semblance with MUSIC algorithm. Such procedure allowed us to estimate the parameters within a resolution limit that is significantly better. This work can be seen as a followup of previous applications of MUSIC to single-parameter velocity analysis and slant stacks. Now, MUSIC has been extended to Common-Reflection-Surface (CRS) multiparameter estimation. Applications of the technique to first synthetic examples, consisting of dipping planar reflectors and point diffractors, and comparison to semblance, confirm, at least for these initial situations, the expected far better resolution of MUSIC. To further support this analysis, CMP velocity analysis has been applied to a real multioffset GPR data set. In this situation, better results were obtained

upon the introduction of a scaled version of MUSIC, denoted semblance-balanced MUSIC. The new algorithm was seen to outperform semblance in resolving interfering events.

Appendix

General Hyperbolic Moveout

The CRS method uses the so-called generalized hyperbolic (normal) moveout, which is the natural generalization of the NMO, valid for CMP gathers, to CRS supergathers, in which source-receiver pairs are arbitrarily located around the (reference) central point, usually taken as a CMP. In 2D, the generalized hyperbolic moveout depends on three parameters, as opposed to conventional NMO, which depends on a single parameter (NMO velocity).

Mathematically, the generalized hyperbolic moveout, $\tau_{i,w}$, associated with the event, w, measured at receiver i, is specified by the zero-offset (ZO) travel-time, τ_{0_w}, and (reference) trace location, x_{0_w}, and given by (see Figure 13)

$$\left[\tau_{i,w}^{\theta}(x_{m_i},h_i)\right]^2 = \left[\tau_{0_w} + A_w(x_{m_i}-x_{0_w})\right]^2 + B_w(x_{m_i}-x_{0_w})^2 + C_w \mathrm{h}_i^2, \tag{A.1}$$

where x_{m_i} is the midpoint coordinate and h_i is the half-offset coordinate for the ith receiver. Here,

$$\boldsymbol{\theta} = \{\mathrm{A}_w, \mathrm{B}_w, \mathrm{C}_w\} \tag{A.2}$$

is the CRS parameter vector, with three parameters, A_w, B_w and C_w, to be estimated from the data. It is instructive to recall that these parameters are related to the angle and curvature quantities as follows [12]:

$$A_w = \frac{2\sin\beta_{0_w}}{v_{0_w}},$$

$$B_w = \frac{2\tau_{0_w}\cos^2\beta_{0_w}}{v_{0_w}} K_{N_w}, \tag{A.3}$$

$$C_w = \frac{2\tau_{0_w}\cos^2\beta_{0_w}}{v_{0_w}} K_{\mathrm{NIP}_w},$$

where K_{N_w} and K_{NIP_w} are the curvatures of respectively the normal (N) and normal-incident-point (NIP) wavefronts, β_{0_w} is the emergence angle and v_{0_w} is the medium velocity. All these quantities are evaluated at the central point, x_{0_w}. Still considering the CRS parameters, we make the following observations

(a) In the CMP configuration of source-receiver pairs symmetrically located with respect to the central point, namely, $x_{m_i} = x_{0_w}$, we have

$$\left[\tau_{i,w}^{\theta}(h_i)\right]^2 = \tau_{0_w}^2 + C_w h_i^2, \tag{A.4}$$

with the CMP, single parameter vector $\boldsymbol{\theta} = \{C_w\}$. Moreover, we have the relation

$$C_w = \frac{4}{v_{\mathrm{NMO}}^2}, \tag{A.5}$$

with C_w given by the lower-most (A.3).

(b) In case the recorded data stems from a diffraction, the condition $B_w = C_w$ holds. This is because as the reflector shrinks to a point, the N-wave turns out to be identical to the NIP-wave [13]. As a consequence, the hyperbolic moveout of diffraction (or *diffraction travel-time*), reduces to

$$\left[\tau_{i,w}^{\theta}(x_{m_i},h_i)\right]^2 = \left[\tau_{0_w} + A_w(x_{m_i}-x_{0_w})\right]^2 + B_w\left[(x_{m_i}-x_{0_w})^2 + h_i^2\right], \tag{A.6}$$

with the diffraction, two-parameter vector $\boldsymbol{\theta} = \{A_w, B_w\}$.

Acknowledgments

The authors would like to thank Dr. Hervé Perroud for providing the GPR dataset. E. Asgedom has been funded by a PhD grant from the University of Oslo and the Norwegian Science Foundation. This work has been carried out partly while he was visiting State University of Campinas. M. Tygel acknowledges support of the Brazilian Council of Scientific and Technological Development (CNPq) and the sponsors of the Wave Inversion Technology (WIT) Consortium.

References

[1] T. Taner and F. Koehler, "Velocity spectra—digital computer derivation and applications of velocity functions," *Geophysics*, vol. 34, no. 6, pp. 859–881, 1969.

[2] N. Neidell and M. Taner, "Semblance and other coherency measures for multichannel data," *Geophysics*, vol. 36, pp. 482–497, 1971.

[3] B. Gelchinsky, E. Landa, and V. Shtivelman, "Algorithms of phase and group correlation," *Geophysics*, vol. 50, no. 4, pp. 596–608, 1985.

[4] R. L. Kirlin, "The relationship between semblance and eigenstructure velocity estimators," *Geophysics*, vol. 57, no. 8, pp. 1027–1033, 1992.

[5] W. Du and R. L. Kirlin, "Discrimination power enhancement via high resolution velocity estimators," in *Proceedings of the IEEE Acoustics, Speech, and Signal Processing*, vol. 4, pp. 13–16, Minneapolis, Minn, USA, 1993.

[6] K. Larner and V. Celis, "Selective-correlation velocity analysis," *Geophysics*, vol. 72, no. 2, pp. U11–U19, 2007.

[7] S. Luo and D. Hale, "Velocity analysis using weighted semblance," *SEG Expanded Abstracts*, pp. 4093–4097, 2010.

[8] M. Sacchi, "A bootstrap procedure for high-resolution velocity analysis," *Geophysics*, vol. 63, no. 5, pp. 1716–1725, 1998.

[9] R. O. Schmidt, "Multiple emitter location and signal parameter estimation," *IEEE Transactions on Antennas and Propagation*, vol. 34, no. 3, pp. 276–280, 1986.

[10] B. Biondi and C. Kostov, "High-resolution velocity spectra using eigenstructure methods," *Geophysics*, vol. 54, no. 7, pp. 832–842, 1989.

[11] H. Perroud and M. Tygel, "Velocity estimation by the common-reflection-surface (CRS) method: using ground-penetrating radar data," *Geophysics*, vol. 70, no. 6, pp. B43–B52, 2005.

[12] R. Jäger, J. Mann, G. Höcht, and P. Hubral, "Common-reflection-surface stack: image and attributes," *Geophysics*, vol. 66, no. 1, pp. 97–109, 2001.

[13] Y. Zhang, S. Bergler, and P. Hubral, "Common-reflection-surface (CRS) stack for common offset," *Geophysical Prospecting*, vol. 49, no. 6, pp. 709–718, 2001.

Chapter 7

"Time-reversal multiple signal classification in case of noise: A phase-coherent approach," Endrias G. Asgedom, Leiv -J. Gelius, Andreas Austeng, Sverre Holm and Martin Tygel, *J. Acoust. Soc. Am.*, vol. 130, no.4, pp. 2024-2034, 2011.

Time-reversal multiple signal classification in case of noise: A phase-coherent approach

Endrias G. Asgedom[a)]
Centre for Imaging, Department of Informatics, University of Oslo, P.O. Box 1080 Blindern No-0316 Oslo, Norway

Leiv-J. Gelius[b)]
Department of Geosciences, University of Oslo, P.O. Box 1047 Blindern No-0316 Oslo, Norway

Andreas Austeng and Sverre Holm
Centre for Imaging, Department of Informatics, University of Oslo, P.O. Box 1080 Blindern No-0316 Oslo, Norway

Martin Tygel
State University of Campinas, Applied Mathematics Department, Cidade Universitria 13083859, Campinas, Brasil

(Received 7 March 2011; revised 22 July 2011; accepted 23 July 2011)

The problem of locating point-like targets beyond the classical resolution limit is revisited. Although time-reversal MUltiple SIgnal Classification (MUSIC) is known for its super-resolution ability in localization of point scatterers, in the presence of noise this super-resolution property will easily break down. In this paper a phase-coherent version of time-reversal MUSIC is proposed, which can overcome this fundamental limit. The algorithm has been tested employing synthetic multiple scattering data based on the Foldy-Lax model, as well as experimental ultrasound data acquired in a water tank. Using a limited frequency band, it was demonstrated that the phase-coherent MUSIC algorithm has the potential of giving significantly better resolved scatterer locations than standard time-reversal MUSIC. © *2011 Acoustical Society of America.*
[DOI: 10.1121/1.3626526]

PACS number(s): 43.60.Pt, 43.60.Tj [EJS] Pages: 2024–2034

I. INTRODUCTION

Detection and localization of scatterers has been an important research topic within array signal processing for the past three decades.[1] The algorithms developed over these years have progressed from the conventional (or Bartlett) beamformer[1,2] via techniques with a better resolution power (e.g., Capon beamformer, also known as minimum variance distortionless response[1] and the minimum norm technique of Reddi[3]) toward super-resolution techniques like the multiple signal classification (MUSIC) algorithm.[1,4] This latter method has gained considerable attention from the sonar and radar communities for its super-resolution capability of determining the direction of arrivals from multiple signal sources.

Time-reversal MUSIC represents a modification of the classical MUSIC algorithm,[4] which makes it feasible to super-resolve closely separated point scatterers in a possibly non-uniform background medium.[5–7] The basic idea of the technique depends on the ability to decompose the monochromatic response matrix of the experiment into orthogonal signal and noise (nil) subspaces based on singular value decomposition (SVD). Unlike classical MUSIC employed within passive remote sensing type of signal processing,[1,4] there is no inherent assumption made in time-reversal MUSIC about uncorrelated signals. Hence, time-reversal MUSIC can be used to locate point scatterers in the case of correlated sources.[8] The technique has also been tested in the case of multiple scattering data based on the Foldy-Lax approximation,[9,10] showing its capability of resolving targets separated by fractions of a wavelength.[6] However, the underlying theory assumes a relatively high signal-to-noise ratio and most simulations provided in the literature assume a noise-free case.[5,9] In the case of noisy data, time-reversal MUSIC will get easily distorted unless a rather idealized acquisition geometry is applied.[11] An analytical description has been introduced discussing the effect of noise on the singular values of the array-response matrix.[12] The corresponding effect on the pseudo-spectrum of time-reversal MUSIC has also been addressed for smaller amounts of noise.[11]

In this paper the term super-resolution is used to characterize any method with a resolving power beyond the diffraction limit. For a finite aperture, this limit is quantitatively described by the Rayleigh criteria, which for an ideal system approach the classical half wavelength limit. This is different from some literature where super-resolution is associated with the resolution of point-scatterers (features) at subwavelength scale only.

The work presented here introduces a modified version of the time-reversal MUSIC algorithm, which demonstrates phase-coherent properties. The idea is to construct an

a)Author to whom correspondence should be addressed. Also at Department of Geosciences, Univ. of Oslo, P.O. Box 1047 Blindern No-0316 Oslo, Norway. Electronic mail: endriasa@ifi.uio.no
b)Also at Centre for Imaging, Department of Informatics, Univ. of Oslo, P.O. Box 1080 Blindern No-0316 Oslo, Norway.

 0001-4966/2011/130(4)/2024/11/$30.00

alternative pseudo-spectrum operator with an expected value equal to that of the noise-free case for each frequency considered. Moreover, use of mixed-array (i.e., both source and receiver side) projection matrices ensures that phase variations due to noise are preserved. By adding the pseudo-spectra over a given frequency band, random phase variations caused by noise are averaged out.

This paper is organized as follows. First, the fundamental principles behind any subspace type of algorithm are presented. Next, the standard (or incoherent) version of the time-reversal MUSIC algorithm is introduced and the extension to its phase coherent version is accounted for. The validity of the basics behind phase-coherent (PC) MUSIC is verified through Monte Carlo type simulations as well as by the use of multiple-scattering data generated based on the Foldy-Lax model. Finally, PC-MUSIC, time-reversal MUSIC, and Kirchhoff migration are applied to experimental radio-frequency (RF) ultrasound data, demonstrating the superiority of the new technique to give super-resolution images of pointlike scatterers.

II. PROBLEM FORMULATION

This section presents the governing signal model used to define the basic problem of point scattering. The fundamental theoretical concepts behind (incoherent) time-reversal MUSIC are presented followed by an extension to a phase-coherent formulation tailored to handle the noisy case.

A. Data model including noise

Consider separate or coincident source-receiver arrays with N_s and N_r representing respectively the total number of sources and receivers (cf. Figure 1). Each source generates a time-varying wavefield, which propagates through the known background medium with D embedded point scatterers. It is further assumed that a temporal Fourier transform has been applied to the transient data. Let the monochromatic signal vector $\boldsymbol{s}(\omega)$ (dimension $N_s \times 1$) represent the transmitted signal from the source array. Introduce now the complex transfer $N_r \times N_s$ matrix, $\tilde{\boldsymbol{K}}(\omega)$, as follows ($\omega$ representing the angular frequency):

$$\tilde{\boldsymbol{K}}(\omega) = \boldsymbol{K}(\omega) + \boldsymbol{N}(\omega), \tag{1}$$

where $\boldsymbol{K}(\omega)$ is the noise-free response matrix and $\boldsymbol{N}(\omega)$ represents the noise matrix. The monochromatic data associated with this multi-source multi-receiver experiment can now be written formally as

$$\boldsymbol{r}(\omega) = \tilde{\boldsymbol{K}}(\omega)\,\boldsymbol{s}(\omega) \tag{2}$$

where $\boldsymbol{r}(\omega)$ represents the data measured at the receiver array.

The noise-corrupted system matrix, $\tilde{\boldsymbol{K}}(\omega)$, can be further written on its SVD-form as[11,13]

$$\begin{aligned}\tilde{\boldsymbol{K}}(\omega) &= \left[\tilde{\boldsymbol{U}}_{sig}(\omega)\tilde{\boldsymbol{U}}_{\perp}(\omega)\right]\begin{bmatrix}\tilde{\Sigma}_{sig}(\omega) & \mathbf{0}\\ \mathbf{0} & \tilde{\Sigma}_{\perp}(\omega)\end{bmatrix}\begin{bmatrix}\tilde{\boldsymbol{V}}^{H}_{sig}(\omega)\\ \tilde{\boldsymbol{V}}^{\mathrm{H}}_{\perp}(\omega)\end{bmatrix}\\ &= \tilde{\boldsymbol{U}}_{sig}(\omega)\tilde{\Sigma}_{sig}(\omega)\tilde{\boldsymbol{V}}^{H}_{sig}(\omega) + \tilde{\boldsymbol{U}}_{\perp}(\omega)\tilde{\Sigma}_{\perp}(\omega)\tilde{\boldsymbol{V}}^{\mathrm{H}}_{\perp}(\omega),\end{aligned} \tag{3}$$

where the superscript H means complex-conjugated transposed and the subscripts sig and $\perp$ represent the signal and noise subspaces, respectively. In the noise-free case, Eq. (3) simplifies to

$$\begin{aligned}\boldsymbol{K}(\omega) &= \left[\boldsymbol{U}_{sig}(\omega)\boldsymbol{U}_{\perp}(\omega)\right]\begin{bmatrix}\Sigma_{sig}(\omega) & \mathbf{0}\\ \mathbf{0} & \mathbf{0}\end{bmatrix}\begin{bmatrix}\boldsymbol{V}^{H}_{sig}(\omega)\\ \boldsymbol{V}^{\mathrm{H}}_{\perp}(\omega)\end{bmatrix}\\ &= \boldsymbol{U}_{sig}(\omega)\Sigma_{sig}(\omega)\boldsymbol{V}^{H}_{sig}(\omega)\end{aligned} \tag{4}$$

Here, $\Sigma_{sig} = \mathrm{diag}\{\sigma_{sig,1}, \sigma_{sig,2}, .., \sigma_{sig,D}\}$, is a diagonal matrix of D non-zero, real singular values, corresponding to the scatterers. Also, $\boldsymbol{U}_{sig} = [\boldsymbol{u}_{sig,1} \ldots \boldsymbol{u}_{sig,D}]$ and $\boldsymbol{V}_{sig} = [\boldsymbol{v}_{sig,1} \ldots \boldsymbol{v}_{sig,D}]$, where $\boldsymbol{u}_{sig,i}$ and $\boldsymbol{v}_{sig,i}$ are (column) singular vectors of $\boldsymbol{U}_{sig}$ and $\boldsymbol{V}_{sig}$ corresponding to the singular values, $\boldsymbol{\sigma}_{sig,i}$. It is assumed that the rank of the matrix $\boldsymbol{K}$ is $D < \min(N_s, N_r)$, with D representing the total number of scatterers.[7,11] In the same way, the quantities $\boldsymbol{\Sigma}_{\perp}$, $\boldsymbol{U}_{\perp}$, and $\boldsymbol{V}_{\perp}$ represent the counterparts of $\boldsymbol{\Sigma}_{sig}$, $\boldsymbol{U}_{sig}$, and $\boldsymbol{V}_{sig}$, associated to the noise subspace. We finally have the orthonormality properties, namely,

$$\begin{aligned}\boldsymbol{U}^{H}_{sig}(\omega)\boldsymbol{U}_{\perp}(\omega) &= 0,\\ \boldsymbol{V}^{H}_{sig}(\omega)\boldsymbol{V}_{\perp}(\omega) &= 0,\end{aligned} \tag{5}$$

which express the fact that the signal and noise (nil) subspaces are orthogonal. Moreover,

$$\begin{aligned}\boldsymbol{U}^{H}_{sig}(\omega)\boldsymbol{U}_{sig}(\omega) &= \boldsymbol{I},\\ \boldsymbol{V}^{H}_{sig}(\omega)\boldsymbol{V}_{sig}(\omega) &= \boldsymbol{I},\end{aligned} \tag{6}$$

and

$$\begin{aligned}\boldsymbol{U}^{H}_{\perp}(\omega)\boldsymbol{U}_{\perp}(\omega) &= \boldsymbol{I},\\ \boldsymbol{V}^{H}_{\perp}(\omega)\boldsymbol{V}_{\perp}(\omega) &= \boldsymbol{I},\end{aligned} \tag{7}$$

which mean the singular vectors are normalized. Note that we can recast Eq. (4) in the form

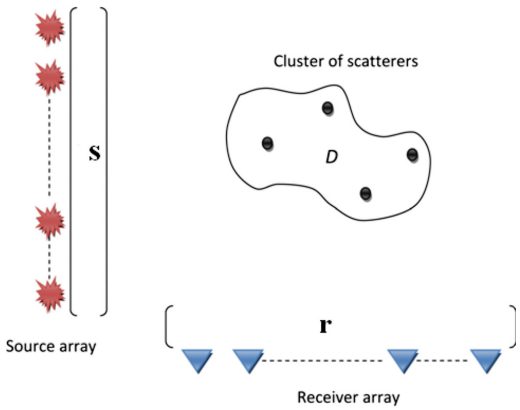

FIG. 1. (Color online) Multi-source multi-receiver experiment involving a cluster of D scatterers.

$$\boldsymbol{K}(\omega) = \sum_{i=1}^{D} \sigma_{sig,i} \boldsymbol{K}_i(\omega), \tag{8}$$

with $\boldsymbol{K}_i = \boldsymbol{u}_{sig,i} \boldsymbol{v}_{sig,i}^H$. A multi-source experiment, where each source is fired at separate times, generates incoherent signals associated with the scatterers. This is due to the fact that each source corresponds to a different location, resulting in varying phases for each of the scattered signals. In addition, the structure of the response-matrix, $\boldsymbol{K}(\omega)$ (or $\tilde{\boldsymbol{K}}(\omega)$) depends on the actual type of acquisition geometry. In the case of moving arrays like in seismic or ground penetrating radar (GPR) this matrix will be partially filled, while for fixed-array ultrasound acquisitions the matrix will be completely filled.

B. Incoherent time-reversal MUSIC algorithm

Assume now a noise-free experiment, which implies that Eq. (4) is a valid representation. Further assume that the scatterers are fully resolved (e.g., ideal array point-spread functions with respect to both source and receiver side), which mathematically can be stated as the conditions[5,11]

$$\boldsymbol{g}_{0r}^H(\boldsymbol{x}_i, \omega) \boldsymbol{g}_{0r}(\boldsymbol{x}, \omega) = \begin{cases} \|\boldsymbol{g}_{0r}(\boldsymbol{x}_i, \omega)\|^2, & \text{if } \boldsymbol{x} = \boldsymbol{x}_i, \\ 0 & \text{if } \boldsymbol{x} \neq \boldsymbol{x}_i, \end{cases} \tag{9a}$$

and

$$\boldsymbol{g}_{0s}^H(\boldsymbol{x}_i, \omega) \boldsymbol{g}_{0s}(\boldsymbol{x}, \omega) = \begin{cases} \|\boldsymbol{g}_{0s}(\boldsymbol{x}_i, \omega)\|^2, & \text{if } \boldsymbol{x} = \boldsymbol{x}_i, \\ 0 & \text{if } \boldsymbol{x} \neq \boldsymbol{x}_i, \end{cases} \tag{9b}$$

where $\boldsymbol{g}_{0s}^H(\boldsymbol{x}_i, \omega)$ and $\boldsymbol{g}_{0r}^H(\boldsymbol{x}_i, \omega)$ represent monochromatic background Green's function (column) vectors with respect to the source and receiver arrays that focus at a point scatterer located at the position $\boldsymbol{x}_i$, and $\boldsymbol{x}$ is the arbitrary test scatterer location. For well-resolved targets satisfying Eqs. (9a) and (9b), an SVD of $\boldsymbol{K}(\omega)$ results in signal subspace singular functions that are normalized versions of the Green's function vectors associated with the scatterers.[5,11] Thus, mathematically the left- and right-singular matrices, $\boldsymbol{U}_{sig}(\omega)$ and $\boldsymbol{V}_{sig}(\omega)$, in Eq. (4) take the forms

$$\begin{aligned} \boldsymbol{U}_{sig}(\omega) &= \left[\frac{\boldsymbol{g}_{0r}(\boldsymbol{x}_1, \omega)}{\|\boldsymbol{g}_{0r}(\boldsymbol{x}_1, \omega)\|} e^{i\theta_1}, \frac{\boldsymbol{g}_{0r}(\boldsymbol{x}_2, \omega)}{\|\boldsymbol{g}_{0r}(\boldsymbol{x}_2, \omega)\|} e^{i\theta_2}, \ldots, \frac{\boldsymbol{g}_{0r}(\boldsymbol{x}_D, \omega)}{\|\boldsymbol{g}_{0r}(\boldsymbol{x}_D, \omega)\|} e^{i\theta_D} \right], \\ \boldsymbol{V}_{sig}(\omega) &= \left[\frac{\boldsymbol{g}_{0s}^*(\boldsymbol{x}_1, \omega)}{\|\boldsymbol{g}_{0s}(\boldsymbol{x}_1, \omega)\|} e^{i\theta_1}, \frac{\boldsymbol{g}_{0s}^*(\boldsymbol{x}_2, \omega)}{\|\boldsymbol{g}_{0s}(\boldsymbol{x}_2, \omega)\|} e^{i\theta_2}, \ldots, \frac{\boldsymbol{g}_{0s}^*(\boldsymbol{x}_D, \omega)}{\|\boldsymbol{g}_{0s}(\boldsymbol{x}_D, \omega)\|} e^{i\theta_D} \right], \end{aligned} \tag{10}$$

where the superscript * denotes a complex conjugate. The singular vectors output from an SVD analysis of a complex-valued matrix system will be non-unique by an arbitrary phase.[11,14] The phase angles in Eqs. (10) represent symbolically this non-uniqueness. Note, however, that the arbitrary phase for the corresponding left- and right-singular vectors are the same.

By using the orthogonality between the signal and noise (nil) subspaces, a signal-subspace based MUSIC pseudo-spectrum operator can be constructed as[6,7,15]

$$P_{MUSIC}(\boldsymbol{x}, \omega) = \frac{1}{1 - A_r(\boldsymbol{x}, \omega)} + \frac{1}{1 - A_s(\boldsymbol{x}, \omega)}, \tag{11}$$

which will peak at the true target locations. In Eq. (11), A_r and A_s represent the receiver and source normalized time-reversal operators

$$\begin{aligned} A_r(\boldsymbol{x}, \omega) &= \frac{\boldsymbol{g}_{0r}^H(\boldsymbol{x}, \omega) \boldsymbol{P}_{sig,r}(\omega) \boldsymbol{g}_{0r}(\boldsymbol{x}, \omega)}{\boldsymbol{g}_{0r}^H(\boldsymbol{x}, \omega) \boldsymbol{g}_{0r}(\boldsymbol{x}, \omega)}, \\ A_s(\boldsymbol{x}, \omega) &= \frac{\boldsymbol{g}_{0s}^T(\boldsymbol{x}, \omega) \boldsymbol{P}_{sig,s}(\omega) \boldsymbol{g}_{0s}^*(\boldsymbol{x}, \omega)}{\boldsymbol{g}_{0s}^T(\boldsymbol{x}, \omega) \boldsymbol{g}_{0s}^*(\boldsymbol{x}, \omega)}, \end{aligned} \tag{12}$$

in which

$$\begin{aligned} \boldsymbol{P}_{sig,r}(\omega) &= \boldsymbol{U}_{sig}(\omega) \boldsymbol{U}_{sig}^H(\omega), \\ \boldsymbol{P}_{sig,s}(\omega) &= \boldsymbol{V}_{sig}(\omega) \boldsymbol{V}_{sig}^H(\omega), \end{aligned} \tag{13}$$

are the signal subspace projection matrices with respect to receiver and source side, respectively. In the literature, the signal-space based MUSIC pseudo-spectrum as given by Eq. (11) is referred to as time-reversal MUSIC.[7] It is to be observed that the same terminology has also been used for a nil-space based MUSIC algorithm.[5] The reason is that the SVD formulation transforms the passive target detection problem into that of an active (secondary) source problem associated with each scatterer.[5,14,16] Time-reversal is an important concept that has been analyzed in detail in the literature (see, e.g., Ref. 7). A short summary of that concept and its main properties is provided in Appendix A.

It is to be noted that the operators $A_r(\boldsymbol{x}, \omega)$ and $A_s(\boldsymbol{x}, \omega)$ give magnitude values only. In a noise-free case both should ideally be one at the location of the scatterer(s). If the data are corrupted with noise the MUSIC pseudo-spectrum in Eq. (11) takes the form

$$\tilde{P}_{MUSIC}(\boldsymbol{x}, \omega) = \frac{1}{1 - \tilde{A}_r(\boldsymbol{x}, \omega)} + \frac{1}{1 - \tilde{A}_s(\boldsymbol{x}, \omega)}, \tag{14}$$

with the operation of time-reversal now being distorted by noise and calculated according to the formulas

$$\begin{aligned} \tilde{A}_r(\boldsymbol{x}, \omega) &= \frac{\boldsymbol{g}_{0r}^H(\boldsymbol{x}, \omega) \tilde{\boldsymbol{P}}_{sig,r}(\omega) \boldsymbol{g}_{0r}(\boldsymbol{x}, \omega)}{\|\boldsymbol{g}_{0r}(\boldsymbol{x}, \omega)\|^2}, \\ \tilde{A}_s(\boldsymbol{x}, \omega) &= \frac{\boldsymbol{g}_{0s}^T(\boldsymbol{x}, \omega) \tilde{\boldsymbol{P}}_{sig,s}(\omega) \boldsymbol{g}_{0s}^*(\boldsymbol{x}, \omega)}{\|\boldsymbol{g}_{0s}(\boldsymbol{x}, \omega)\|^2}, \end{aligned} \tag{15}$$

in which

$$\tilde{\boldsymbol{P}}_{sig,r}(\omega) = \tilde{\boldsymbol{U}}_{sig}(\omega)\tilde{\boldsymbol{U}}^{H}_{sig}(\omega),$$
$$\tilde{\boldsymbol{P}}_{sig,s}(\omega) = \tilde{\boldsymbol{V}}_{sig}(\omega)\tilde{\boldsymbol{V}}^{H}_{sig}(\omega). \tag{16}$$

In the original time-reversal works,[5–7] the issue of noise was not discussed in detail. In the presence of noise, the distinction between the signal and nil subspaces is no longer perfectly defined. Hence, the two subspaces will start to mix and the sharp border defined by the singular values will now be replaced by a smooth transition zone. The effect of noise on nil-subspace based time-reversal MUSIC has been previously analyzed employing a linearized perturbation theory.[11] Applying a similar approach here, gives the following expected values of the time-reversal operations in Eqs. (15) [cf. Eqs. (B11), (B13), and (B14) in Appendix B]

$$E\left[\tilde{A}_r(\boldsymbol{x},\omega)\right] = A_r(\boldsymbol{x},\omega) + \zeta\sigma^2 A_{\perp,r}(\boldsymbol{x},\omega),$$
$$E\left[\tilde{A}_s(\boldsymbol{x},\omega)\right] = A_s(\boldsymbol{x},\omega) + \zeta\sigma^2 A_{\perp,s}(\boldsymbol{x},\omega), \tag{17}$$

where

$$A_{\perp,r}(\boldsymbol{x},\omega) = \frac{\boldsymbol{g}^{H}_{0r}(\boldsymbol{x},\omega)\boldsymbol{P}_{\perp,r}(\omega)\boldsymbol{g}_{0r}(\boldsymbol{x},\omega)}{\|\boldsymbol{g}_{0r}(\boldsymbol{x},\omega)\|^2},$$
$$A_{\perp,s}(\boldsymbol{x},\omega) = \frac{\boldsymbol{g}^{T}_{0s}(\boldsymbol{x},\omega)\boldsymbol{P}_{\perp,s}(\omega)\boldsymbol{g}^{*}_{0s}(\boldsymbol{x},\omega)}{\|\boldsymbol{g}_{0s}(\boldsymbol{x},\omega)\|^2}, \tag{18}$$

in which

$$\boldsymbol{P}_{\perp,r}(\omega) = \boldsymbol{U}_{\perp}(\omega)\boldsymbol{U}^{H}_{\perp}(\omega),$$
$$P_{\perp,s}(\omega) = \boldsymbol{V}_{\perp}(\omega)\boldsymbol{V}^{H}_{\perp}(\omega), \tag{19}$$

are the receiver and source projection matrices of the nil-subspace (noise-free case). Moreover, σ^2 is the variance of the noise (assuming a variance of $\sigma^2/2$ of both real and imaginary parts of the noise matrix $\boldsymbol{N}$) and

$$\zeta = \frac{1}{\sigma^2_{sig,1}} + \frac{1}{\sigma^2_{sig,2}} + \ldots + \frac{1}{\sigma^2_{sig,D}}. \tag{20}$$

It follows directly from Eqs. (17) that, at each scatterer location, the expected values of the time-reversal operations will be the same as for the noise-free case (unit value and no phase). This implies also that the (noise) time-reversal MUSIC operator in Eq. (14) will have the same expectation value as in the noise-free case at each scatterer location (within a linearized noise model). This will apply for every frequency considered.

For a given frequency band, $\Delta\omega$, the multi-frequency equivalent of Eqs. (14) and (17) can be introduced (N_ω representing the number of discrete frequencies available), namely,

$$\tilde{P}_{MUSIC}(\boldsymbol{x},\Delta\omega) = \frac{1}{1-\tilde{A}_r(\boldsymbol{x},\Delta\omega)} + \frac{1}{1-\tilde{A}_s(\boldsymbol{x},\Delta\omega)}, \tag{21}$$

where

$$\tilde{A}_r(\boldsymbol{x},\Delta\omega) = \frac{1}{N_\omega}\sum_{\Delta\omega}\tilde{A}_r(\boldsymbol{x},\omega),$$
$$\tilde{A}_s(\boldsymbol{x},\Delta\omega) = \frac{1}{N_\omega}\sum_{\Delta\omega}\tilde{A}_s(\boldsymbol{x},\omega). \tag{22}$$

However, these quantities contain no phase information. Hence, in the case of noise, they will not coherently add at the scatterer locations. To illustrate the sensitivity of incoherent time-reversal MUSIC to noise, a synthetic data example involving four point scatterers was considered (cf. Figure 2, where dimensions are given in terms of the center wavelength). Non-coincident source and receiver arrays were employed, both of them consisting of 15 elements (half center wavelength sampling). Controlled data were generated employing a zero-phase Ricker wavelet with a center frequency of 20 Hz. The background velocity model was assumed homogenous with a velocity of 2000 m/s. To include possible interactions between the scatterers (especially the two closest ones) a Foldy-Lax type of model was used to generate the scattered data. White noise was added to the data having a variance of 10% of the rms-amplitude of the corresponding signal in time domain. In this analysis a frequency band between 15 and 25 Hz was selected, falling symmetrically around the center frequency. The maximum frequency of 25 Hz was chosen so that the Rayleigh spatial resolution limit, Δl, was violated in the case of the two closest scatterers. This resolution limit was calculated according to the formula

$$\Delta l = \frac{L\lambda}{D}, \tag{23}$$

where λ is the wavelength, D is the aperture or length of the array, and L is the distance to the target object. In the case considered here $L = 2000$ m, $D = 700$ m and $\lambda = 80$ m, which give $\Delta l = 228.6$ m. Correspondingly, the two scatterers were separated by a distance of 200 m. To verify that this set of parameters corresponds to a diffraction limited experiment, the test data was first imaged using a seismic

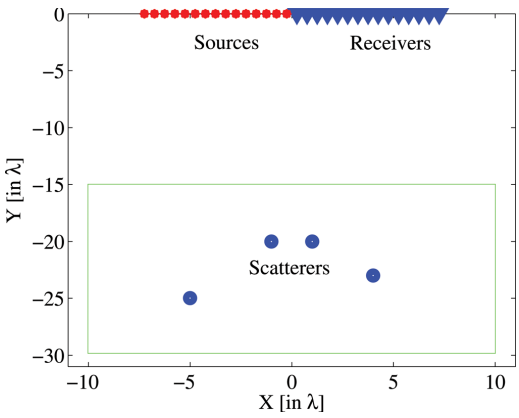

FIG. 2. (Color online) Data acquisition geometry and scattering model. The solid line rectangle defines the image size employed in the data analysis.

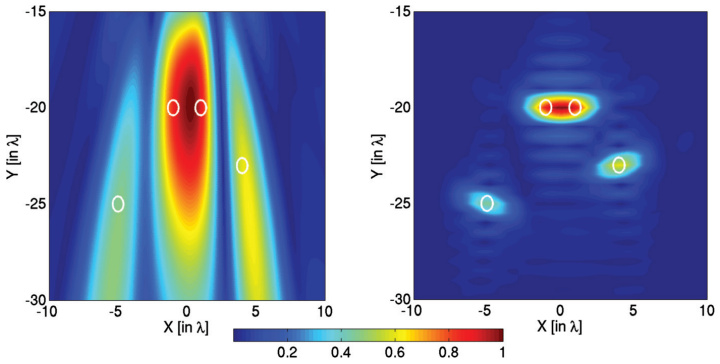

FIG. 3. Kirchhoff migration result at the center frequency of 20 Hz (left) and using a band of frequencies between 15 and 25 Hz (right). The circles show the diffraction limits at the true locations of the scatterers.

migration type of algorithm (e.g., Kirchhoff prestack migration with no weights applied). The final results obtained are shown in Fig. 3 for the center frequency (left) and from using the band between 15 and 25 Hz (right). It can easily be seen that the two nearby scatterers are not resolved as expected. The size of the image in Fig. 3 is defined by the solid line rectangle superimposed in Fig. 2. The same image dimension will be used in the simulations to follow. Around each scatterer location in Fig. 3 a circle representing the classical resolution limit of half a wavelength has been introduced. These circles are used in the subsequent analysis to verify if the spot sizes of the imaged locations are smaller or larger than this classical limit. After this preliminary analysis we are now in a position to test out the time-reversal part of the incoherent MUSIC algorithm. Time-reversal of the singular functions according to Eq. (15) at the center frequency of 20 Hz gave the results shown in Fig. 4 top left and right (source and receiver array side, respectively). Figure 4 bottom left and right show the corresponding results obtained using a band of frequencies between 15 and 25 Hz. As in Fig. 3, circles with radii of half the wavelength (computed for the maximum frequency of 25 Hz) overlay each scatterer location. For a single frequency it can be clearly seen from Fig. 4 that time-reversal resolves the scatterers poorly. Using a band of frequencies (cf. Fig. 4 bottom left and right), due to the lack of phase-coherency, the time-reversal image shows essentially no improvement and the two nearby scatterers are not resolved at all.

Repeated computation of the source and receiver side time-reversal operators over the frequency-band followed by the computation of the MUSIC pseudo-spectrum [cf. Eq. (21)] is denoted incoherent time-reversal MUSIC by analogy with the classical incoherent MUSIC.[17] As in the case of time-reversal, this approach will not satisfy the phase-coherency condition in general needed for a noisy case, because as magnitudes only are involved, the noise-level can be significantly enhanced. Figure 5 top left and right images show the result of employing this procedure with the same noise-corrupted data as in the previous example. After applying a band of frequencies (cf. Fig. 5 top right), the MUSIC pseudo-spectrum is still not able to locate the scatterers well and the noise level has also increased compared to the single

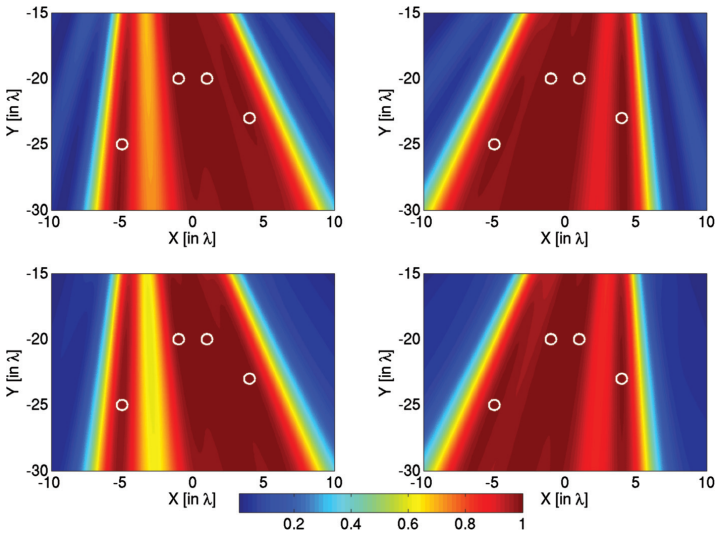

FIG. 4. Source-side time-reversal result of 20 Hz (top left), receiver-side time-reversal result of 20 Hz (top right), bottom left and right results are the same as the top left and right results but now using a band of frequencies between 15 and 25 Hz. The circles show the diffraction limits at the true locations of the scatterers.

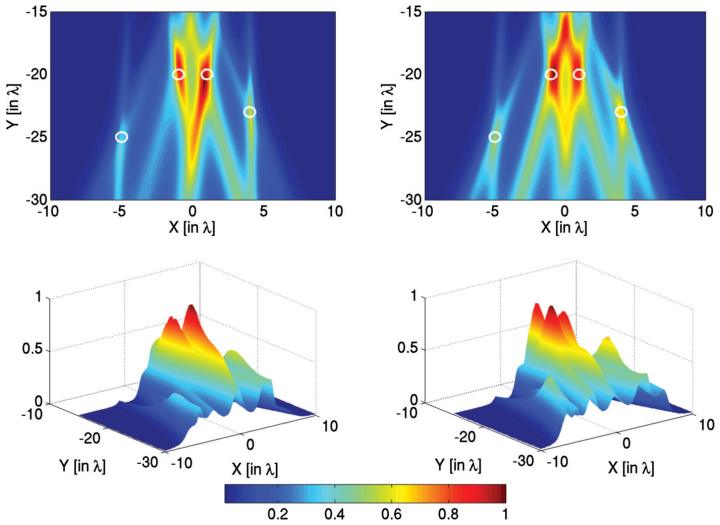

FIG. 5. Incoherent time-reversal MUSIC at the center frequency of 20 Hz (top left) and using a band of frequencies between 15 and 25 Hz (top right). The circles show the diffraction limits at the true locations of the scatterers. The bottom left and right figures represent the 3-D views of top left and top right, respectively.

frequency result (cf. Fig. 5 top left). The above series of observations motivates the development of a phase-coherent (PC) version of time-reversal MUSIC, as described in the next section.

C. Phase-coherent (PC) MUSIC

A mixed-array time-reversal formulation has been introduced earlier in the literature,[14] which preserves the phase and therefore can add coherently over a band of frequencies. We adapt this idea and introduce the normalized mixed-array time-reversal operation, replacing the ones in Eqs. (15) (noise-case):

$$\tilde{A}_{Mix}(\boldsymbol{x},\omega)=\frac{\boldsymbol{g}_{0r}^{H}(\boldsymbol{x},\omega)\tilde{\boldsymbol{P}}_{sig,Mix}(\omega)\boldsymbol{g}_{0s}^{*}(\boldsymbol{x},\omega)}{\|\boldsymbol{g}_{0r}(\boldsymbol{x},\omega)\|\|\boldsymbol{g}_{0s}(\boldsymbol{x},\omega)\|}, \tag{24}$$

where we have denoted

$$\tilde{\boldsymbol{P}}_{sig,Mix}(\omega)=\tilde{U}_{sig}(\omega)\tilde{V}_{sig}^{H}(\omega). \tag{25}$$

As shown in Appendix B [cf. Eqs. (B11) and (B15)], the expected value of the noisy projection matrix is the same as its noise-free counterpart, namely,

$$E\left[\tilde{\boldsymbol{P}}_{sig,Mix}(\omega)\right]=\boldsymbol{P}_{sig,Mix}(\omega). \tag{26}$$

As a consequence,

$$\begin{aligned}E\left[\tilde{A}_{Mix}(\boldsymbol{x},\omega)\right]&=\frac{\boldsymbol{g}_{0r}^{H}(\boldsymbol{x},\omega)E\left[\tilde{\boldsymbol{P}}_{sig,Mix}(\omega)\right]\boldsymbol{g}_{0s}^{*}(\boldsymbol{x},\omega)}{\|\boldsymbol{g}_{0r}(\boldsymbol{x},\omega)\|\|\boldsymbol{g}_{0s}(\boldsymbol{x},\omega)\|},\\&=\frac{\boldsymbol{g}_{0r}^{H}(\boldsymbol{x},\omega)\boldsymbol{P}_{sig,Mix}(\omega)\boldsymbol{g}_{0s}^{*}(\boldsymbol{x},\omega)}{\|\boldsymbol{g}_{0r}(\boldsymbol{x},\omega)\|\|\boldsymbol{g}_{0s}(\boldsymbol{x},\omega)\|}\\&=A_{Mix}(\boldsymbol{x},\omega).\end{aligned} \tag{27}$$

The question is now if an improved resolution can be obtained by using a MUSIC type of approach. By analogy with Eq. (14), we now introduce the PC-MUSIC operator (noise assumed),

$$\tilde{P}_{MIXED}(\boldsymbol{x},\omega)=\frac{1}{1-\tilde{A}_{Mix}(\boldsymbol{x},\omega)}, \tag{28}$$

and for a band of frequencies ($\Delta\omega$) the PC-MUSIC pseudo-spectrum can be generalized as

$$\tilde{P}_{MIXED}(\boldsymbol{x},\Delta\omega)=\frac{1}{1-\tilde{A}_{Mix}(\boldsymbol{x},\Delta\omega)}, \tag{29}$$

where

$$\tilde{A}_{Mix}(\boldsymbol{x},\Delta\omega)=\frac{1}{N_\omega}\sum_{\Delta\omega}\tilde{A}_{Mix}(\boldsymbol{x},\omega). \tag{30}$$

Due to the phase-condition in Eq. (27), it also follows directly that

$$\begin{aligned}E\left[\tilde{A}_{Mix}(\boldsymbol{x},\Delta\omega)\right]&=\frac{1}{N_\omega}\sum_{\Delta\omega}E\left[\tilde{A}_{Mix}(\boldsymbol{x},\omega)\right]\\&=\frac{1}{N_\omega}\sum_{\Delta\omega}A_{Mix}(\boldsymbol{x},\omega)=A_{Mix}(\boldsymbol{x},\Delta\omega).\end{aligned} \tag{31}$$

Hence, the PC-MUSIC pseudo-spectrum will have expected values equal to that of the noise-free case at each scatterer location. More precisely: the expected phase should be zero at the same locations (for a single frequency or a band of frequencies). We carried out a simple test to verify the noise model governed by Eq. (28). Once again the acquisition geometry was according to the one given in Fig. 2. The only difference was that the four original scatterers were replaced by a single scatterer placed at $[0,-20\,\lambda]$. The PC-MUSIC pseudo-spectrum was computed at the center frequency using Eq. (28). The computation was

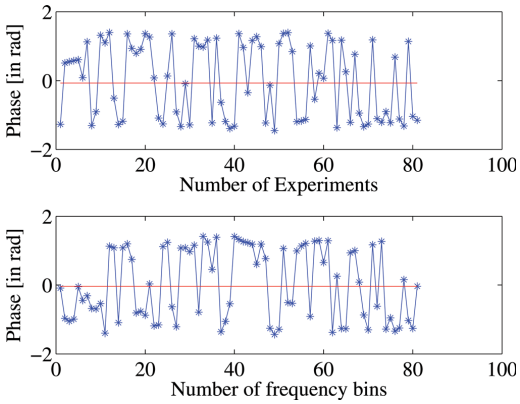

FIG. 6. (Color online) Phase of PC-MUSIC pseudo-spectrum at the scatterer location for noisy data. (Top) 81 repeated experiments and (bottom) 81 different frequency bins. Solid curve represents phase after averaging based on PC-MUSIC pseudo-spectra.

repeated 81 times and each time white noise was added to the signal before SVD (variance of noise about 10% of rms-amplitude of signal in time-domain). For each computation the phase of the pseudo-spectrum at the exact scatterer location was extracted. Figure 6 top shows how this phase varies in a random manner for this ensemble of experiments. In addition, the individual pseudo-spectra were added together and the phase of this PC-MUSIC operator was calculated again at the scatterer point (shown as a solid curve in Fig. 6 top). As expected, the phase of the PC-MUSIC operator is now close to zero at the target location [as predicted from Eqs. (27) and (28)].

The time-reversal part of the PC-MUSIC operator in Eq. (29) has the phase-coherency property sought after.[14] It is therefore likely to expect that PC-MUSIC also shows the same property. More specifically, its pseudo-spectrum should have a phase close to zero at each scatterer location after frequency summation. This is also supported by the results obtained in Fig. 6 top. Because the random phase behavior observed in this figure will occur for every available frequency, the phase variation with frequency will consequently also vary randomly at the location of a scatterer. To verify this assumption we repeated the previous experiment except with one change: Instead of varying the number of experiments for a fixed frequency we varied the frequency by scanning through the defined band (same as before). For each individual frequency the phase of the pseudo-spectrum was computed at the target location. Finally, each pseudo-spectrum was added based on Eq. (29) to demonstrate the inherent phase-coherency characteristic. The results are summarized in Fig. 6 bottom. It can easily be seen that the phase is close to zero (solid curve) after frequency-summation.

After having carefully analyzed the characteristics of the proposed PC-MUSIC operator, it is time to compare its performance with that of incoherent time-reversal MUSIC. Figure 7 represents the equivalence of the previous results given in Fig. 5. It can easily be seen that phase-coherent MUSIC gives a super-resolved image of all scatterers (cf. Figure 7 right). In addition, we can observe that each location spot size is smaller than the classical resolution limit. For completeness the result obtained using a single (center) frequency is shown in Fig. 7 left. As expected, a single frequency is, in general, not sufficient and a coherent summation over a band is needed.

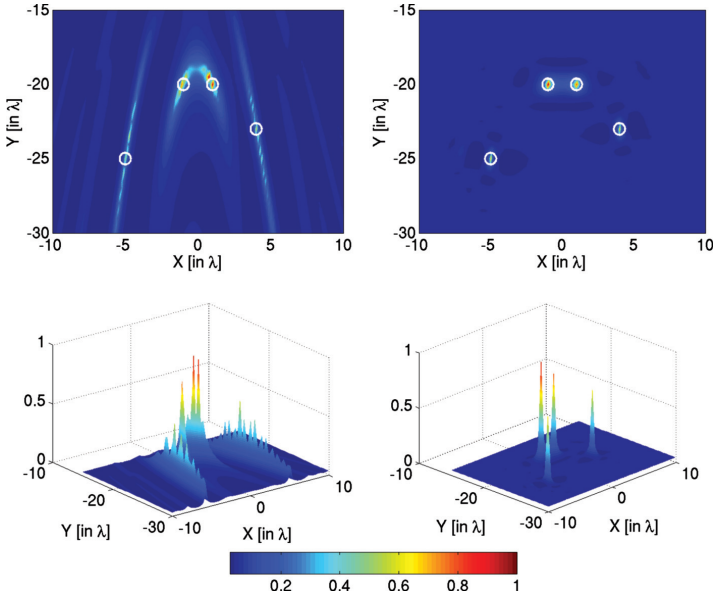

FIG. 7. Phase-coherent MUSIC for a single frequency (top left) and a band (top right). The circles show the diffraction limits at the true locations of the scatterers. The bottom left and right figures represent the 3-D views of top left and top right, respectively.

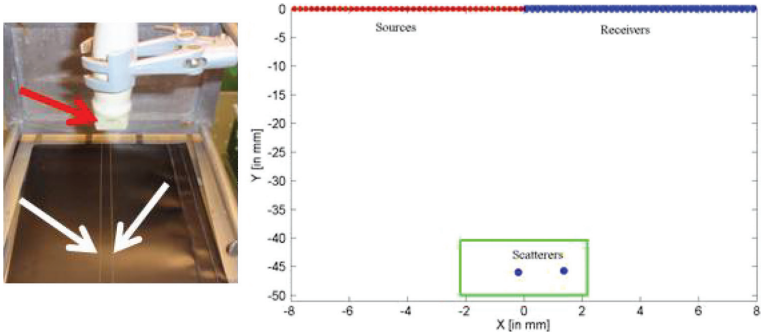

FIG. 8. Measurement setup (left) and simplified view in the plane of insonification (right). The white arrows in the left plot show the target wires and the red arrow shows the transducer. The green rectangle defines the image size employed in the experimental analysis.

III. EXPERIMENTAL ULTRASOUND DATA RESULTS

The performance of the phase-coherent MUSIC algorithm in Eq. (29) was investigated employing water-tank RF data.[18] The experimental setup included an 18.5 mm long linear transceiver array consisting of 96 source-receiver elements and 2 wire targets (cf. Figure 8 left) that can be considered as point-like scatteres in the plane of insonification. The transducers were driven at a frequency of 4 MHz and the received signals were sampled at a frequency of 20 MHz. In order to demonstrate the super-resolution (i.e., beyond the classical diffraction limit) properties of PC-MUSIC, we reduced the number of array elements in use to simulate a subset of separate source and receiver arrays with 41 elements each. (cf. Figure 8 right). The targets were placed approximately 46 mm away from the transducers (with a slight tilt and a shift to the right) and separated by slightly less than 2 mm (cf. Figure 8 right). The Rayleigh spatial resolution limit for a 41 element array with each element separated by half a wavelength of 0.375 mm (computed for a maximum frequency of 4 MHz) is about 2.2 mm. This distance exceeds the actual separation between the two scatterers. Consequently, conventional imaging algorithms like Kirchhoff migration will not be able to resolve the two scatterers given a maximum frequency limit of 4 MHz.

As a result of experimental noise the separation between the signal and noise subspaces is not ideal. However, for the frequency band considered in this experiment (3.7 MHz to 4.0 MHz) two dominating singular values still exist, as shown in Fig. 9. Note that the singular values get smaller with increasing frequency. This is caused by the instrument response having a center frequency of 3.5 MHz, not corrected for here.

In the following, PC-MUSIC was compared with standard (phase-incoherent) time- reversal MUSIC as well as Kirchhoff migration. The results obtained for a single frequency of 4 MHz (corresponding to the center frequency) are shown in Fig. 10. For both types of MUSIC methods the results are not of super-resolution quality and Kirchhoff migration could not resolve the two scatterers.

Next, the idea of adding over the available frequency band between 3.7 and 4.0 MHz is tested out (cf. Figure 11). On comparison with Fig. 10 the following observations can be made: (i) standard time-reversal MUSIC has virtually not improved as expected, (ii) Kirchhoff migration is not able to

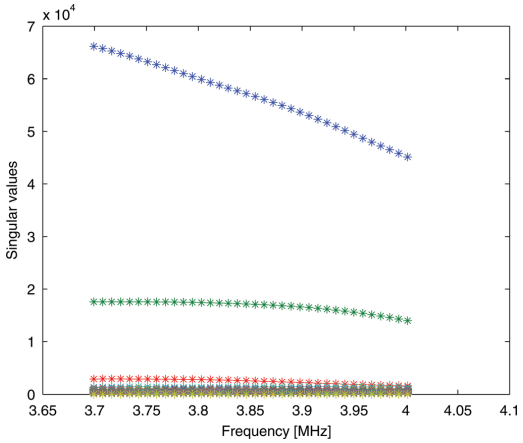

FIG. 9. (Color online) Distribution of singular values over the selected frequency band.

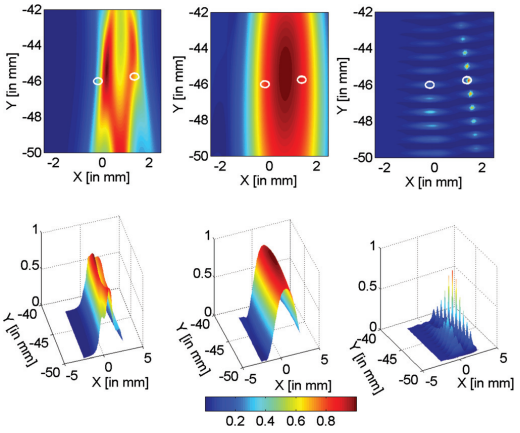

FIG. 10. Standard time-reversal MUSIC (left), Kirchhoff migration (middle), and phase-coherent MUSIC (right). Single frequency of 4 MHz employed (center frequency). The white circles show the classical diffraction limits.

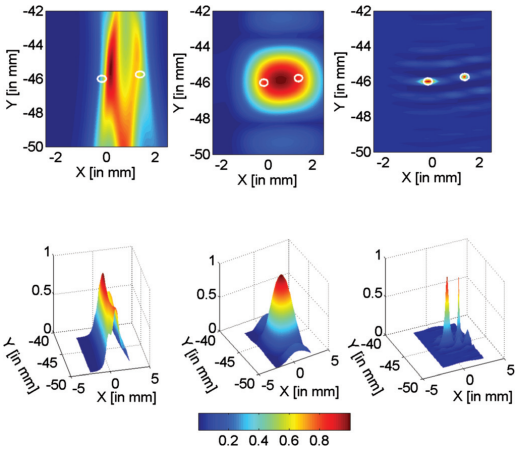

FIG. 11. Standard time-reversal MUSIC (left), Kirchhoff migration (middle), and phase-coherent MUSIC (right). Frequency band 3.7–4.0 MHz. The white circles show the classical diffraction limits.

resolve the two scatterers because they are separated above the Rayleigh spatial resolution limit, and (iii) the best resolution can be observed for phase-coherent MUSIC, which provides a super-resolution result of the two scatterers demonstrating that experimental noise can be handled well by this improved technique.

IV. CONCLUDING REMARKS

A modified MUSIC algorithm has been introduced, which enables a phase-coherency property to be introduced in the standard-type time-reversal MUSIC algorithm. In this way the effect of random noise can be averaged by considering a band of frequencies. The feasibility of such an approach is supported by the fact that the expected value of the MUSIC pseudo-spectrum in the case of random noise is identical to that of the noise-free case (at least within a linearized noise analysis). The validity of this noise model is verified through Monte Carlo simulations.

The phase-coherent MUSIC algorithm proposed in this paper has been tested employing experimental ultrasound data acquired in a water tank. The target consisted of two thin wires, which in the plane of insonification could be regarded as two point scatterers. Using the frequency band of the experimental data it was demonstrated that the new PC-MUSIC algorithm has the potential of giving significantly better resolved scatterers than both standard time-reversal MUSIC and prestack migration (Kirchhoff type). Future work with this algorithm will include investigating its possible extension to the case of non-point like target objects.

ACKNOWLEDGMENTS

E. Asgedom has been funded by a Ph.D. grant from the University of Oslo and the Norwegian Science Foundation. Part of this work was carried out while he was visiting State University of Campinas. The authors are also thankful to two anonymous reviewers for many helpful comments to improve the manuscript.

APPENDIX A: THE TIME-REVERSAL CONCEPT

In this appendix we provide a brief summary of the concept of time-reversal, which plays a crucial role in the work presented in the main text. Without loss of generality, our discussion of the time-reversal process will be focused on the so-called two-transceiver array situation. In that case, the experimental setup is still the one shown in Fig. 1, however both the source and receiver arrays act as transceiver arrays. For simplicity, we also assume a noise-free case. Two different time-reversal experiments can be carried out. In the first, signals are transmitted from array 1 and measured at array 2 (subscripts indicate array number)

$$\boldsymbol{r}_2(\omega) = \boldsymbol{K}(\omega)\boldsymbol{s}_1(\omega). \tag{A1}$$

Time-reversal of measurement, $\boldsymbol{r}_2(\omega)$, and detection at transceiver array 1 satisfies, by definition,

$$\boldsymbol{r}_1(\omega) = K^T(\omega)\boldsymbol{r}_2^*(\omega), \tag{A2}$$

in which the superscript T denotes matrix transpose and the superscript * represents complex conjugation, which corresponds to time-reversal in the frequency domain. Substitution of Eq. (A1) into Eq. (A2) and taking complex conjugates on both sides, yields

$$\boldsymbol{r}_1^*(\omega) = \boldsymbol{K}^H(\omega)\boldsymbol{K}(\omega)\boldsymbol{s}_1(\omega) = \boldsymbol{T}_1(\omega)\boldsymbol{s}_1(\omega). \tag{A3}$$

The matrix $\boldsymbol{T}_1(\omega) = \boldsymbol{K}^H(\omega)\boldsymbol{K}(\omega)$ is now the time-reversal operator [5,16] with respect to transceiver array 1. Correspondingly, by considering the alternative experiment where signals are emitted from array 2, time-reversed, and then measured at receiver array 1 gives the following relationship

$$\boldsymbol{r}_2^*(\omega) = \boldsymbol{K}^*(\omega)\boldsymbol{K}^T(\omega)\boldsymbol{s}_2(\omega) = \boldsymbol{T}_2(\omega)\boldsymbol{s}_2(\omega), \tag{A4}$$

where the matrix $\boldsymbol{T}_2(\omega) = \boldsymbol{K}^*(\omega)\boldsymbol{K}^T(\omega)$ is the time-reversal operator[16] with respect to transceiver array 2. Specializing to the original problem, where transceiver array 1 represents the source array and transceiver array 2 is the receiver array, it is straightforward to show that[16]

$$\boldsymbol{T}_1(\omega)\boldsymbol{P}_{sig,s}(\omega) = \Sigma_{sig}^2(\omega)\boldsymbol{P}_{sig,s}(\omega), \tag{A5}$$

and

$$\boldsymbol{T}_2(\omega)\boldsymbol{P}_{sig,r}(\omega) = \Sigma_{sig}^2(\omega)\boldsymbol{P}_{sig,r}(\omega), \tag{A6}$$

where $\Sigma_{sig}^2 = \Sigma_{sig}\Sigma_{sig}$, in which Σ_{sig} is the signal-subspace eigenvalue matrix defined in Eq. (4). Hence, the source-side projection vectors correspond to the eigenvectors of the time-reversal operator $\boldsymbol{T}_1$. Correspondingly, the receiver-side projection vectors correspond to the eigenvectors of the time-reversal operator $\boldsymbol{T}_2$.

APPENDIX B: LINEARIZED NOISE ANALYSIS OF TIME-REVERSAL AND PHASE-COHERENT MUSIC

Here we make use of a first-order perturbation expansion of an SVD for the purpose of analyzing the effect of noise on the projection matrices required for generating both the time-reversal and phase-coherent MUSIC pseudo-spectra. We are mainly interested to show quantitatively the effect of noise on the expected values of both the time-reversal and phase- coherent MUSIC projection matrices discussed in Sec. II.A and Sec. II.B. More specifically, our aim is to prove Eqs. (17) and (26) given in the main text.

Adapting the second-order perturbation described in Ref. 13, and simplifying it to first-order (see also Ref. 11), we consider the perturbed noise and signal singular vector matrix components in the form

$$\begin{aligned}\tilde{\boldsymbol{U}}_{sig} &= \boldsymbol{U}_{sig} + \boldsymbol{U}_{\perp}R,\\ \tilde{\boldsymbol{U}}_{\perp} &= \boldsymbol{U}_{\perp} + \boldsymbol{U}_{sig}Q,\end{aligned} \tag{B1}$$

for the matrix components of the left-hand side matrix $\tilde{\boldsymbol{U}} = [\tilde{\boldsymbol{U}}_{sig}\tilde{\boldsymbol{U}}_{\perp}]$, and

$$\begin{aligned}\tilde{\boldsymbol{V}}_{sig} &= \boldsymbol{V}_{sig} + \boldsymbol{V}_{\perp}M,\\ \tilde{\boldsymbol{V}}_{\perp} &= \boldsymbol{V}_{\perp} + \boldsymbol{V}_{sig}L,\end{aligned} \tag{B2}$$

for the matrix components of the right-hand side matrix $\tilde{\boldsymbol{V}} = [\tilde{\boldsymbol{V}}_{sig}\tilde{\boldsymbol{V}}_{\perp}]$. Here, $\boldsymbol{Q}$, $\boldsymbol{R}$, $\boldsymbol{L}$, and $\boldsymbol{M}$ represent the perturbation coefficient matrices. The orthogonality between the signal and nil space is expressed as [compare with Eqs. (5)]

$$\begin{aligned}\tilde{\boldsymbol{U}}_{\perp}^{H}\tilde{\boldsymbol{U}}_{sig} &= \boldsymbol{0},\\ \tilde{\boldsymbol{V}}_{\perp}^{H}\tilde{\boldsymbol{V}}_{sig} &= \boldsymbol{0}.\end{aligned} \tag{B3}$$

Substitution of Eqs. (B1) and (B2) into Eq. (B3) gives

$$\begin{aligned}\boldsymbol{R} &= -\boldsymbol{Q}^{H},\\ \boldsymbol{M} &= -\boldsymbol{L}^{H}.\end{aligned} \tag{B4}$$

Explicit expressions for the perturbation matrices $\boldsymbol{R}$ and $\boldsymbol{M}$ can be obtained as[11]

$$\begin{aligned}\boldsymbol{R} &= \boldsymbol{U}_{\perp}^{H}\boldsymbol{N}\boldsymbol{V}_{sig}\Sigma_{sig}^{-1},\\ \boldsymbol{M} &= \boldsymbol{V}_{\perp}^{H}\boldsymbol{N}^{H}\boldsymbol{U}_{sig}\Sigma_{sig}^{-1},\end{aligned} \tag{B5}$$

where signal-subspace, singular-value matrix, Σ_{sig}, and noise matrix, $\boldsymbol{N}$, are given by equations (1), (3), and (4) in the main text. Eqs. (B5) permit derivation of the following important results,

$$\begin{aligned}E[\boldsymbol{R}] &= \boldsymbol{U}_{\perp}^{H}E[\boldsymbol{N}]\boldsymbol{V}_{sig}\Sigma_{sig}^{-1} = 0,\\ E[\boldsymbol{M}] &= \boldsymbol{V}_{\perp}^{H}E\left[\boldsymbol{N}^{H}\right]\boldsymbol{U}_{sig}\Sigma_{sig}^{-1} = 0.\end{aligned} \tag{B6}$$

A. Computation of projected matrices and their expected values

Under the formulations (B1) and (B2), the projected matrices, $\tilde{\boldsymbol{P}}_{sig,r}$, $\tilde{\boldsymbol{P}}_{sig,s}$, and $\tilde{\boldsymbol{P}}_{sig,Mix}$, can be written as

$$\begin{aligned}\tilde{\boldsymbol{P}}_{sig,r} &= \left(\boldsymbol{U}_{sig} + \boldsymbol{U}_{\perp}\boldsymbol{R}\right)\left(\boldsymbol{U}_{sig} + \boldsymbol{U}_{\perp}\boldsymbol{R}\right)^{H},\\ \tilde{\boldsymbol{P}}_{sig,s} &= \left(\boldsymbol{V}_{sig} + \boldsymbol{V}_{\perp}\boldsymbol{M}\right)\left(\boldsymbol{V}_{sig} + \boldsymbol{V}_{\perp}\boldsymbol{M}\right)^{H},\\ \tilde{\boldsymbol{P}}_{sig,Mix} &= \left(\boldsymbol{U}_{sig} + \boldsymbol{U}_{\perp}\boldsymbol{R}\right)\left(\boldsymbol{V}_{sig} + \boldsymbol{V}_{\perp}\boldsymbol{M}\right)^{H}.\end{aligned} \tag{B7}$$

After a little algebra, the above equations can be recast into the alternative form

$$\begin{aligned}\tilde{\boldsymbol{P}}_{sig,r} &= \boldsymbol{U}_{\perp}\boldsymbol{R}\boldsymbol{R}^{H}\boldsymbol{U}_{\perp}^{H} + \boldsymbol{P}_{sig,r} + \tilde{\boldsymbol{X}}_{sig,r},\\ \tilde{\boldsymbol{P}}_{sig,s} &= \boldsymbol{V}_{\perp}\boldsymbol{M}\boldsymbol{M}^{H}\boldsymbol{V}_{\perp}^{H} + \boldsymbol{P}_{sig,s} + \tilde{\boldsymbol{X}}_{sig,s},\\ \tilde{\boldsymbol{P}}_{sig,Mix} &= \boldsymbol{U}_{\perp}\boldsymbol{R}\boldsymbol{M}^{H}\boldsymbol{V}_{\perp}^{H} + \boldsymbol{P}_{sig,Mix} + \tilde{\boldsymbol{X}}_{sig,Mix},\end{aligned} \tag{B8}$$

in which we have denoted

$$\begin{aligned}\tilde{\boldsymbol{X}}_{sig,r} &= \boldsymbol{U}_{sig}\boldsymbol{R}^{H}\boldsymbol{U}_{\perp}^{H} + \boldsymbol{U}_{\perp}\boldsymbol{R}\boldsymbol{U}_{sig}^{H},\\ \tilde{\boldsymbol{X}}_{sig,s} &= \boldsymbol{V}_{sig}\boldsymbol{M}^{H}\boldsymbol{V}_{\perp}^{H} + \boldsymbol{V}_{\perp}\boldsymbol{M}\boldsymbol{V}_{sig}^{H},\\ \tilde{\boldsymbol{X}}_{sig,Mix} &= \boldsymbol{U}_{sig}\boldsymbol{M}^{H}\boldsymbol{V}_{\perp}^{H} + \boldsymbol{U}_{\perp}\boldsymbol{R}\boldsymbol{V}_{sig}^{H}.\end{aligned} \tag{B9}$$

We are now ready to compute the expected values of the projected matrices in Eqs. (B8). In view of Eqs. (B6), we readily observe that

$$\begin{aligned}E\left[\tilde{\boldsymbol{X}}_{sig,r}\right] &= \boldsymbol{U}_{sig}E\left[\boldsymbol{R}^{H}\right]\boldsymbol{U}_{\perp}^{H} + \boldsymbol{U}_{\perp}E[\boldsymbol{R}]\boldsymbol{U}_{sig}^{H} = 0,\\ E\left[\tilde{\boldsymbol{X}}_{sig,s}\right] &= \boldsymbol{V}_{sig}E\left[\boldsymbol{M}^{H}\right]\boldsymbol{V}_{\perp}^{H} + \boldsymbol{V}_{\perp}E[\boldsymbol{M}]\boldsymbol{V}_{sig}^{H} = 0,\\ E\left[\tilde{\boldsymbol{X}}_{sig,Mix}\right] &= \boldsymbol{U}_{sig}E\left[\boldsymbol{M}^{H}\right]\boldsymbol{V}_{\perp}^{H} + \boldsymbol{U}_{\perp}E[\boldsymbol{R}]\boldsymbol{V}_{sig}^{H} = 0.\end{aligned} \tag{B10}$$

As a consequence, we find from Eqs. (B8),

$$\begin{aligned}E\left[\tilde{\boldsymbol{P}}_{sig,r}\right] &= \boldsymbol{U}_{\perp}E\left[\boldsymbol{R}\boldsymbol{R}^{H}\right]\boldsymbol{U}_{\perp}^{H} + \boldsymbol{P}_{sig,r},\\ E\left[\tilde{\boldsymbol{P}}_{sig,s}\right] &= \boldsymbol{V}_{\perp}E\left[\boldsymbol{M}\boldsymbol{M}^{H}\right]\boldsymbol{V}_{\perp}^{H} + \boldsymbol{P}_{sig,s},\\ E\left[\tilde{\boldsymbol{P}}_{sig,Mix}\right] &= \boldsymbol{U}_{\perp}E\left[\boldsymbol{R}\boldsymbol{M}^{H}\right]\boldsymbol{V}_{\perp}^{H} + \boldsymbol{P}_{sig,Mix}.\end{aligned} \tag{B11}$$

Under the use of Eqs. (B4) and (B5), we now observe that

$$\begin{aligned}\boldsymbol{R}\boldsymbol{R}^{H} &= \left[\boldsymbol{U}_{\perp}^{H}\boldsymbol{N}\boldsymbol{V}_{sig}\Sigma_{sig}^{-1}\right]\left[\boldsymbol{U}_{\perp}^{H}\boldsymbol{N}\boldsymbol{V}_{sig}\Sigma_{sig}^{-1}\right]^{H}\\ &= \boldsymbol{U}_{\perp}^{H}\boldsymbol{N}\boldsymbol{V}_{sig}\Sigma_{sig}^{-2}\boldsymbol{V}_{sig}^{H}\boldsymbol{N}^{H}\boldsymbol{U}_{\perp}\\ &= \boldsymbol{U}_{\perp}^{H}N\sum_{i=1}^{D}\frac{1}{\sigma_{sig,i}^{2}}\boldsymbol{\upsilon}_{sig,i}\boldsymbol{\upsilon}_{sig,i}^{H}\boldsymbol{N}^{H}\boldsymbol{U}_{\perp},\end{aligned} \tag{B12}$$

from which

$$\begin{aligned}E\left[\boldsymbol{R}\boldsymbol{R}^{H}\right] &= \boldsymbol{U}_{\perp}^{H}\left(\sum_{i=1}^{D}\frac{1}{\sigma_{sig,i}^{2}}E\left[\boldsymbol{N}\boldsymbol{\upsilon}_{sig,i}\boldsymbol{\upsilon}_{sig,i}^{H}\boldsymbol{N}^{H}\right]\right)\boldsymbol{U}_{\perp}\\ &= \boldsymbol{U}_{\perp}^{H}\left(\sum_{i=1}^{D}\frac{1}{\sigma_{sig,i}^{2}}E\left[\sum_{k=1}^{N_s}\upsilon_{sig,i}(k)\boldsymbol{n}_{k}\sum_{l=1}^{N_s}\upsilon_{sig,i}^{*}(l)\boldsymbol{n}_{l}^{H}\right]\right)\boldsymbol{U}_{\perp}\\ &= \boldsymbol{U}_{\perp}^{H}\left(\sum_{i=1}^{D}\frac{1}{\sigma_{sig,i}^{2}}\sum_{k=1}^{N_s}\sum_{l=1}^{N_s}\left(\upsilon_{sig,i}(k)\upsilon_{sig,i}^{*}(l)\right)E\left[\boldsymbol{n}_{k}\boldsymbol{n}_{l}^{H}\right]\right)\boldsymbol{U}_{\perp}\\ &= \boldsymbol{U}_{\perp}^{H}\left(\sum_{i=1}^{D}\frac{1}{\sigma_{sig,i}^{2}}\sum_{k=1}^{N_s}\sum_{l=1}^{N_s}\left(\upsilon_{sig,i}(k)\upsilon_{sig,i}^{*}(l)\right)\sigma^{2}\boldsymbol{I}\delta_{k,l}\right)\boldsymbol{U}_{\perp}\\ &= \boldsymbol{U}_{\perp}^{H}\left(\sum_{i=1}^{D}\frac{1}{\sigma_{sig,i}^{2}}\left\|\boldsymbol{\upsilon}_{sig,i}\right\|\sigma^{2}\boldsymbol{I}\right)\boldsymbol{U}_{\perp} = \zeta\sigma^{2}\boldsymbol{I},\end{aligned} \tag{B13}$$

where $\upsilon_{sig,i}(k)$ represents the k-th element of the vector $\boldsymbol{\upsilon}_{sig,i}$, $\upsilon^*_{sig,i}(l)$ represents the l-th element of the vector $\boldsymbol{\upsilon}^H_{sig,i}$, $\boldsymbol{n}_k$ is the k-th column vector of $\boldsymbol{N}$, $\boldsymbol{n}_l$ is the l-th row vector of $\boldsymbol{N}^H$, and ζ is given by Eq. (20). In the same way, we have

$$E\left[\boldsymbol{M}\boldsymbol{M}^H\right] = \boldsymbol{V}_\perp^H\left(\sum_{i=1}^{D}\frac{1}{\sigma^2_{sig,i}}E\left[\boldsymbol{N}^H\boldsymbol{u}_{sig,i}\boldsymbol{u}^H_{sig,i}\boldsymbol{N}\right]\right)\boldsymbol{V}_\perp = \zeta\sigma^2\boldsymbol{I}, \tag{B14}$$

and the same approach gives also

$$\begin{aligned} E\left[\boldsymbol{R}\boldsymbol{M}^H\right] &= \boldsymbol{U}_\perp^H\left(\sum_{i=1}^{D}\frac{1}{\sigma^2_{sig,i}}E\left[\boldsymbol{N}\boldsymbol{\upsilon}_{sig,i}\boldsymbol{u}^H_{sig,i}\boldsymbol{N}\right]\right)\boldsymbol{V}_\perp \\ &= \boldsymbol{U}_\perp^H\left(\sum_{i=1}^{D}\frac{1}{\sigma^2_{sig,i}}E\left[\sum_{k=1}^{N_s}\upsilon_{sig,i}(k)\boldsymbol{n}_k\sum_{l=1}^{N_r}u^*_{sig,i}(l)\hat{\boldsymbol{n}}_l\right]\right)\boldsymbol{V}_\perp \\ &= \boldsymbol{U}_\perp^H\left(\sum_{i=1}^{D}\frac{1}{\sigma^2_{sig,i}}\sum_{k=1}^{N_s}\sum_{l=1}^{N_r}\upsilon_{sig,i}(k)u^*_{sig,i}(l)E[\boldsymbol{n}_k\hat{\boldsymbol{n}}_l]\right)\boldsymbol{V}_\perp \\ &= \boldsymbol{0}, \end{aligned} \tag{B15}$$

where $\hat{\boldsymbol{n}}_l$ is the l-th row vector of $\boldsymbol{N}$. Finally, using Eqs. (B11) and (B13)–(B15), we readily recover Eqs. (17) and (26) in the main text.

[1]H. Krim and M. Viberg, "Two decades of array signal processing research," IEEE Signal Process. Mag., **47**, 67–94 (1996).
[2]M. S. Bartlett, "Smoothing periodograms from time series with continuous spectra," Nature **161**, 686–687 (1948).
[3]S. S. Reddi, "Multiple source locationa digital approach," IEEE Trans. Aerosp. Electron. Syst., **15**, 95–105 (1979).
[4]R. O. Schmidt, "Multiple emitter location and signal parameter estimation," IEEE Trans. Antennas Propag. **34**, 276–280 (1986).
[5]S. K. Lehman and A. J. Devaney, "Transmission mode time-reversal super-resolution imaging," J. Acoust. Soc. Am. **113**, 2742–2753 (2003).
[6]C. Prada and J. L. Thomas, "Experimental subwavelength localization of scatterers by decomposition of the time reversal operator interpreted as a covariance matrix," J. Acoust. Soc. Am. **114**, 235–243 (2003).
[7]A. J. Devaney, "Super-resolution processing of multi-static data using time-reversal and MUSIC," Northeastern University Report, available at http://www.ece.neu.edu/faculty/ devaney/ajd/preprints.htm (Last viewed February 10, 2011).
[8]A. J. Devaney, "Time reversal imaging of obscured targets from multi-static data," IEEE Trans Antennas Propag. **53**, 1600–1610 (2005).
[9]F. K. Gruber, E. A. Marengo, and A. J. Devaney, "Time-reversal imaging with multiple signal classification considering multiple scattering between the targets," J. Acoust. Soc. Am. **115**, 3042–3047 (2004).
[10]F. Simonetti, M. Fleming, and E. A. Marengo, "Illustration of the role of multiple scattering in subwavelength imaging from far-field measurements," J. Opt. Soc. Am. **25**, 292–303 (2008).
[11]L.-J. Gelius and E. G. Asgedom, "Diffraction-limited imaging and beyond - the concept of super resolution," Geophys. Prospect. **59**, 400–421 (2010).
[12]M. Davy, J.-G. Minonzio, J. de Rosny, C. Prada, and M. Fink, "Influence of noise on subwavelength imaging of two close scatterers using time reversal method: theory and experiments," Prog. Electromagn. Res. **98**, 333–358 (2009).
[13]R. J. Vaccaro, "A second-order perturbation expansion for the SVD," SIAM J. Matrix Anal. Appl. **15**, 661–671 (1994).
[14]S. Hou, K. Huang, K. Solna, and H. Zhao, "A phase and space coherent direct imaging method," J. Acoust. Soc. Am. **25**, 227–238 (2009).
[15]S. Hou, K. Solna, and H. Zhao, "A direct imaging method using far field data," Inverse Probl. **23**, 1533–1546 (2007).
[16]L.-J. Gelius, "Time-reversal and super-resolution in case of two transceiver arrays: Generalized DORT," in *Proceedings of the CPS/SEG Beijing International Conference and Exposition*, April 24–27, Beijing, China (2009).
[17]H. Wang and M. Kaveh, "Coherent signal-subspace processing for the detection and estimation of angles of arrival of multiple wide-band sources," IEEE Trans. Acoust., Speech, Signal Process. **33**, 823–831 (1985).
[18]J.-F. Synnevåg, A. Austeng, and S. Holm, "Adaptive beamforming applied to medical ultrasound imaging," IEEE Trans. Ultrason. Ferroelectr. Freq. Control, **54**, 1606–1613 (2007).

Chapter 8

"Seismic Coherency Measures in Case of Interfering Events: A Focus on the Most Promising Candidates of Higher-Resolution Algorithms,"
Endrias G. Asgedom, Leiv -J. Gelius and Martin Tygel,
IEEE Signal Processing Magazine, vol. 29, no. 3, pp. 47-56, 2012.

Chapter 9

"2D Common-Offset Traveltime Based Diffraction Enhancement and Imaging," Endrias G. Asgedom, Leiv -J. Gelius, and Martin Tygel, *Geophysical Prospecting*, Submitted for publication, Oct. 2012.